2009

Scanning probe microscopy investigations of (1) arrays of cysteine-coated CdS nanoparticles and (2) structures formed during the early stages of the corrosion of copper surfaces

Brian Robert Lewandowski
Louisiana State University and Agricultural and Mechanical College

SCANNING PROBE MICROSCOPY INVESTIGATIONS OF (1) ARRAYS OF CYSTEINE-COATED CdS NANOPARTICLES AND (2) STRUCTURES FORMED DURING THE EARLY STAGES OF THE CORROSION OF COPPER SURFACES

A Dissertation

Submitted to the Graduate Faculty of the
Louisiana State University and
Agricultural and Mechanical College
in partial fulfillment of the
requirements for the degree of
Doctor of Philosophy

in

The Department of Chemistry

by
Brian R. Lewandowski
B.S., Loyola University New Orleans, 2004

May 2009

ACKNOWLEDGMENTS

First of all I would like to thank my advisor, Dr. Jayne Garno, for the guidance she has provided throughout my time at LSU. I would also like to thank her for the great opportunities she has given to me while a student in her research group. She has motivated my interests in the fields of surface science and scanning probe microscopy.

I also would like to thank Dr. Darren Lytle who was my advisor during my stay with the Environmental Protection Agency in Cincinnati, OH. I am grateful for his guidance and direction that he gave me for my research conducted there. I also thank Christy Muhlen, Chris Parrett, and Christina Bennett-Stamper for making my time in Cinninnati enjoyable. For our collaborators, I thank Robert Singleton, Mark Lowry, and Dr. Isiah Warner for the supply of the quantum dots used in my research.

I would also like to thank all of the members of the Garno research group, past and present, for their helpful discussion during my time at LSU. I especially thank Jie-Ren Li, Zorabel LeJeune, and Kathie Lusker for their friendship and fun times I have had as a graduate student.

TABLE OF CONTENTS

LIST OF TABLES

LIST OF FIGURES

ABSTRACT

Scanning probe microscopy (SPM) characterizations are becoming more prevalent for surface investigations due to their capabilities for obtaining structural information and physical measurements. New capabilities of SPM for studying and controlling nanoscale processes are emerging as valuable assets in research. A fundamental understanding of the interactions of surface reactions provides essential information for developing workable applications for nanotechnology. Two applications of SPM are discussed in this dissertation.

The first investigation uses atomic force microscopy (AFM) for the characterization of nanostructures produced with a newly developed lithographic technique called "two-particle" lithography. This new technique is based on particle lithography for the patterning of nanoparticles. Structural templates of either latex or silica guide the deposition of nanoparticles to generate 2D arrays of nanopatterns. The surface coverage, size and periodicity of the nanoparticle structures can be controlled by changing the particle size of the templating sphere. Particle lithography provides test platforms to enable multiple reproducible SPM measurements for nanostructures which have well-defined geometries and surface arrangements.

The second part of the dissertation discusses the results from using AFM to study the earliest stages of the onset of water corrosion of copper surfaces with nanoscale resolution. Within a few hours of exposure to water of varying chemistries, dramatic differences in the morphology of copper surfaces were observed by ex situ AFM topography imaging. Surface characterizations of the treated copper samples were used systematically evaluate changes for copper surfaces with various chemical treatments and to investigate mechanisms of passivation and corrosion.

CHAPTER 1. INTRODUCTION

The focus of this dissertation was to apply an interdisciplinary approach using scanning probe methods in combination with fundamental investigations using analytical chemistry, surface science, environmental and materials chemistry. Because of the dual capabilities for obtaining physical measurements and structural information with unprecedented sensitivity, scanning probe characterizations are becoming prevalent for surface investigations. The new capabilities of scanning probe microscopy (SPM) for studying and controlling processes at the nanoscale are emerging as valuable assets in both fundamental and applied research. Imaging modes of SPM have been used for studies of chemical and biochemical reactions and for investigations of tip-surface interactions,[1, 2] chemical structures,[3-6] and material properties[7, 8] at the molecular level. Scanning probe methods not only provide a means for characterizing samples with unprecedented spatial resolution, but also can be applied for nanoscale measurements of surface properties and as a tool for constructing designed surface arrangements of molecules.[9-11] Scientific developments using SPM are providing a foundation for new technologies in areas such as molecular electronics,[12-14] materials engineering,[15, 16] medical diagnostics,[17, 18] and drug discovery.[19] Fundamental understanding of the interactions of surface reactions provides essential information for developing workable applications for nanotechnology.

Two applications of SPM are advanced in this dissertation. The first investigation applies atomic force microscopy (AFM) for characterizing nanostructures produced with a newly developed procedure for nanolithography described as "two-particle" lithography.[20] Protocols were developed to prepare surface structures of cysteine-coated CdS quantum dots with nanoscale control of the placement and surface coverage of nanoparticles. Particle lithography provided test platforms to enable multiple reproducible SPM measurements for nanostructures

having well-defined geometries and surface arrangements. In the second part of the dissertation, the earliest stages of the onset of water corrosion of copper surfaces was investigated with nanoscale resolution using AFM imaging.[21, 22] Within a few hours of exposure to water of varying chemistries, dramatic differences in the morphology of copper surfaces were observed at the nanoscale with ex situ AFM topography images. These experiments were conducted at the National Risk Management Research Laboratory within the Water Supply and Water Resources Division of the United States Environmental Protection Agency (USEPA) in Cincinnati, Ohio, in collaborative research with Dr. Darren Lytle. New ex situ protocols were developed for treating copper surfaces and information was obtained by viewing changes in surface morphology at the earliest stages of corrosion. Nanoscale AFM characterizations were used to investigate mechanisms of surface passivation and corrosion, and to systematically evaluate changes for copper surfaces with various chemical treatments.

1.1 Experimental Approach: Operating Principles of AFM Imaging Modes

The second chapter of the dissertation provides details of the experimental approaches for SPM imaging modes used for these studies. The imaging principle, hardware and instrument operation for contact mode and tapping mode AFM will be described, as well as the corresponding simultaneously acquired channels of frictional force and phase imaging modes, respectively. The imaging principle for a newly developed magnetic imaging mode using magnetic sample modulation (MSM) will be explained.[23, 24] Force modulation AFM, magnetic AC or MAC mode AFM, and magnetic force microscopy (MFM) will also be described to provide perspective and background information for understanding the investigations presented in this dissertation.

1.2 Nanostructures of Cysteine-Coated CdS Nanoparticles Produced with "Two-Particle" Lithography

Particle or nanosphere lithography is an approach for nanopatterning which uses physical adsorption of materials to surfaces. Monodisperse latex particles self-assemble into periodic structures on flat surfaces, which can then be used as structural templates or photomasks to direct the deposition of materials.[25-27] The latex particles are removed by various approaches, such as calcination,[28-30] solvent dissolution,[31-33] adhesive tape,[34] or simple rinsing with water.[35-37] Particle lithography has been successfully applied for patterning metals, sols, polymers, and inorganic materials.[26, 38-41] Researchers have also applied particle lithography with latex beads as photomasks, to construct functional surfaces for selective protein adsorption on lithographically defined regions.[41, 42] Particle lithography can be applied for controlling the organization of proteins on surfaces through physical adsorption.[35] This approach is a highly reproducible and robust method for patterning nanomaterials, and serves as an excellent starting point for continuing to develop more complex protocols with different surfaces and nanomaterials. Particle lithography is a practical technology which is amenable to further steps of chemical reactions, or for developing well-defined test structures for fundamental surface measurements. The methods of particle lithography offer advantages of nanometer precision and high throughput, since a small milliliter vial of solution can produce hundreds of replicate samples.

There is an emerging need for efficient methods that can produce organized arrays of nanomaterials with high throughput. Particle lithography provides such an approach for rapidly preparing millions of exquisitely uniform nanometer-sized structures on flat surfaces, using basic steps of bench chemistry (e.g., centrifugation, drying, evaporation, rinsing). A new lithography procedure was developed based on particle lithography for the patterning of nanoparticles into ordered arrays of nanostructures. The new procedure, called "two-particle" lithography is

described in Chapter 3, demonstrating AFM images of nanostructures produced with cysteine-coated CdS quantum dots. The cysteine-coated CdS quantum dots were synthesized by students in collaborative research with Professor Isiah Warner's research group. Using two-particle lithography, we have developed a method to control the surface coverage and arrangement of quantum dots such as cysteine-coated CdS nanoparticles.[20] Chapter 3 describes the new approach for patterning cysteine-coated nanoparticles to generate surface arrangements of ring structures, in which the diameter and spacing depend on the diameter and monodispersity of the particle used for the structural template, either polystyrene latex or silica mesoparticles. Atomic force microscopy is used to visualize the nanostructures produced and to measure the height, diameter, and surface coverage of nanopatterned surfaces.

The mechanism for controlling the arrangement of nanoparticles is based on natural self-assembly of colloidal mesospheres into close-packed arrangements on flat surfaces. The organized arrays of nanoparticles are ideal test platforms for surface measurements and provide a tool for fundamental studies of material properties. For example, designed arrays of deposited metal nanoparticles can be applied for fundamental studies of magnetic, structural and electronic properties with various AFM imaging modes. Results with cysteine-capped CdS quantum dots reveal well-organized periodic ring-shaped patterns, which cover micron-sized areas of flat surfaces such as mica(0001). Well-defined arrays of nanostructures furnish precise reproducible dimensions for multiple successive AFM measurements. The nanoparticle templates used for test platforms can be scaled to very small dimensions, to enable studies of size-dependent properties at tens of nanometers. In comparison to conventional methods for creating nanostructures which use costly lasers, electron/ion beams or clean rooms, particle lithography is inexpensive and accessible to researchers with conventional bench equipment. The two-particle

lithography procedure uses the simple steps of centrifuging, drying and rinsing. Particle lithography can be applied to organize a range of nanomaterials such as proteins,[35, 36] nanoparticles[34, 43, 44] and organic molecules[45-47] on surfaces with exquisite control of surface arrangements and chemistry. Size scalable test platforms facilitate successive reproducible SPM measurements. In addition, the nanopatterning approach described in Chapter 3 provides new insight for interesting self-assembly phenomena, which can be applied to assemble nanoparticles at ultrasmall size scales. The rationale for choosing CdS nanoparticles as model systems, the strategy for preparing well-defined nanostructures of nanoparticles and the plans for further SPM measurements will be detailed in Chapter 3.

1.3 Surface Changes of Copper during the Initial Stages of Water Corrosion Investigated by AFM: Role of pH, Phosphates, and Dissolved Inorganic Carbon

In Chapters 4 and 5, AFM was applied to investigate the role of different water chemistries on the initial stages of the corrosion of copper surfaces. The source of lead and copper contaminants for drinking water is primarily from leaching of metal plumbing. The surface features of Cu_2O which initially form on a corroding copper surface upon exposure to drinking water directly impact the type and extent of corrosion and copper levels for consumer tap water samples. Therefore studies of the influence of water chemistry for the resulting generation of copper corrosion by-products that form at the early stages of corrosion are important for improving the quality of drinking water. The degradation of metal pipelines in water distribution systems caused by corrosion is an important research focus for the Water Supply and Water Resources Division of the USEPA. In water distribution pipelines, valves, and fixtures, corrosion can be detrimental to the quality of public drinking water. One area of research within the USEPA aims to control corrosion and reduce the release of metals into drinking water.

Copper occurs naturally in rock, soil, water, sediment, and air, and is often used for water pipes in household plumbing. Though a small amount of copper is required by the human body as an essential nutrient, long-term exposure to elevated levels of copper in drinking water may cause serious health problems.[48] Short periods of exposure to high levels of copper have been shown to cause gastrointestinal disturbance, such as nausea and vomiting. Using water with elevated levels of copper over many years may cause damage to the liver or kidneys. The primary sources of copper in drinking water are corroding pipes and brass components of household plumbing systems. Signs that drinking water may have elevated levels of copper include a metallic taste or blue to blue-green stains around sinks and plumbing fixtures. Corrosion leads to the release of copper ions into water samples and forms deposits of corrosion by-products on the interior walls of metal pipes. In 1991, the USEPA published the Lead and Copper Rule in the National Primary Drinking Water Regulations (also referred to as the LCR or 1991 Rule). The Lead and Copper Rule requires that lead and copper levels in drinking water be minimized and public water utilities are enforced by these standards. An action level of 0.015 milligrams per liter (mg/L) was established for lead and 1.3 mg/L for copper for water samples standing for more than six hours.

The effects of pH and phosphate (ortho- and poly-) levels, as well as high levels of dissolved inorganic carbon, on the corrosion of copper surfaces were examined using AFM, secondary ion mass spectrometry (SIMS) and x-ray diffraction (XRD) analyses. High resolution AFM clearly reveals differences in the structure and morphology for by-products formed on copper surfaces after only 6 to 24 hours of exposure to water samples. For example, orthophosphate was found to substantially reduce the size and distribution of crystalline features that formed on copper surfaces. Substantial differences in surface morphology at different pH

levels were also investigated within the normal pH range of tap water samples. The details of experimental protocols that were developed in collaborative efforts with the USEPA laboratory, as well as the results and conclusions of these investigations are given in Chapters 4 and 5.

1.4 Synopsis and Future Prospectus

A considerable challenge is posed for making reproducible measurements in nanosized systems, for scaling and manufacturing devices at nanometer length scales, and for systematically evaluating the effects of molecular structure for material properties. One of the major problems with surface studies is the lack of reproducibility and accuracy for measurement technologies. For example, measuring electrical conductance with reliability has proven to be technically difficult for molecularly thin films due to problems with generating consistent test platforms of molecules and nanomaterials. Another challenge is to develop methods for reproducibly depositing nanoparticles on surfaces with desired arrangements and coverage. To address these challenges, a new approach for particle lithography was developed to generate designed planar arrays of regular nanostructures of quantum dots, to serve as a measurement platform for SPM measurements of nanomaterials properties.

The approach for producing regular arrangements of nanoparticles with high throughput as SPM test platforms has further been applied to pattern other systems of nanoparticles for other research projects in the Garno research group. A brief overview of the new directions and applications of particle lithography is provided in Chapter 6. Two-particle lithography has been successfully applied to systems of coated nanoparticles such as plasmid DNA-encapsulated metal nanoparticles,[43] coated cobalt nanoparticles[44] and CdSe quantum dots.[34] A key advantage of two-particle lithography is that expensive instrumentation is not required for generating well-defined nanostructures of designed dimension and periodicity. The resulting arrangements of magnetic nanoparticles, for example, are important for commercial applications such as

ultrasmall transistors, catalysts, magnetic devices, immunoassay labeling, and medical imaging. In addition, collaborative work with surface characterizations of copper surfaces is being continued by Ms. Stephanie Daniels this year. She has begun to develop in situ protocols for visualizing even earlier stages of copper corrosion, and will investigate the influence of other ions that are naturally present in water for surface corrosion.

At present, scanning probe microscopes and nanoscale lithographies are primarily used as research tools in laboratories rather than as tools for manufacturing. However in the future, nanoscale technology in manufacturing is predicted to bring an even greater impact and benefit to society than present-day microfabrication technologies. Potential applications include the development of a new generation of chemical and biosensors, biochips, drug delivery mechanisms, analysis platforms and molecular electronic devices. We anticipate that nanoscale research will define new directions in areas such as materials chemistry, biosensing, biomimetic surfaces and molecule-based electronics. Work at the nanoscale interface is a promising multidisciplinary research frontier, offering a wealth of opportunities for new investigations of chemical reactions on surfaces. Studies of the fundamental reactions of surface-bound molecules, including mechanisms, kinetics, chemical modification and surface properties are valuable areas for academic research.

CHAPTER 2. IMAGING MODES OF ATOMIC FORCE MICROSCOPY

1.1 Overview of Scanning Probe Microscopy

Scanning probe microscopy (SPM) provides a new class of imaging techniques which offer a means to view surfaces in greater detail than previously possible. Scanning tunneling microscopy (STM) was invented by Binnig and Rohrer in 1982[49] and for this development they were awarded the Nobel Prize in Physics in 1986. Shortly afterwards, the atomic force microscope (AFM) was invented by Binnig, Quate, and Gerber in 1986.[50] The invention of these new approaches for surface microscopy has captured a new view of surfaces and provides rich information for scientific research. Unlike traditional optical microscopes, SPM techniques use a sharp probe affixed to a cantilever to "feel" the surface rather than using lenses to "see" a specimen. Therefore the resolution is not limited by the wavelength of light. The interactions between the tip and the sample are recorded and processed to form an image. The surface structure of materials can be observed in real time on a scale from microns down to nanometers. The lattice arrangement of atoms can be visualized, and STM provides views of molecular and atomic vacancies and adatoms.

There are several advantages to using AFM compared to other microscopy techniques. Images generated by AFM are true three-dimensional surface profiles. Samples do not require special treatments or coatings which alter their composition. Both conducting and insulating materials may be imaged. A vacuum environment is not required for AFM imaging, and samples can be imaged in air or in liquid media.

Since the invention of AFM, a range of different imaging modes have been developed to characterize the physical properties of surfaces, thin films, and nanomaterials.[51] In normal contact mode, a sharp tip is scanned across a sample and the laser deflection is monitored to provide surface topography information.[50, 52, 53] One drawback of contact mode is that drag

forces develop between loosely bound samples and the scanning probe, which can alter or damage the surface. To overcome this limitation, tapping mode was developed.[54-56] Tapping mode is a type of intermittent contact mode in which the cantilever is oscillated at a certain frequency and scanned over a sample. This greatly reduces the dragging forces[57] and makes it an excellent mode for imaging biological materials.[58-61] Conducting-probe AFM (CP-AFM) is an imaging mode which measures the current-voltage relationship of materials.[62, 63] This particular mode has been used to measure the electronic transport properties of single molecules[64, 65] and self-assembled monolayers.[66-68] Force modulation is a mode which measures the relative stiffness of a sample.[69, 70] The Young's modulus of organic thins films of varying sizes has been studied using force modulation.[71, 72] For the imaging of magnetic domains, magnetic force microscopy was developed.[73, 74] This mode is widely used in characterizing magnetic recording media.[75, 76]

The various imaging modes require specific changes to the configuration of the instrument, such as oscillating the AFM probe or changing the positional feedback loop. Rich structural and mechanical information about samples can be obtained for the different imaging modes, such as characterizations of elasticity, adhesion, conductivity, electronic properties and magnetic forces.

This chapter presents the operating principles for several AFM imaging modes used for the research investigations described. Instrument operation for contact mode, force modulation, tapping mode, magnetic AC (MAC) mode and magnetic force microscopy (MFM) are explained. The differences in operation for these imaging modes will provide a clearer understanding of the newly developed magnetic sample modulation (MSM) imaging mode, which is also presented. This new MSM imaging mode is essentially a hybrid technique which uses the feedback loop of

conventional contact mode AFM, the MAC mode solenoid to drive sample oscillation, and the phase and amplitude channels for data acquisition to characterize the selective modulation of magnetic domains.

2.2 Contact Mode and Frictional Force Imaging

Contact mode AFM is a high resolution imaging technique capable of resolving features as small as an atomic lattice. In the most basic configuration, a sharp tip affixed to a cantilever is scanned across a surface. The tip is rastered in continuous contact across a surface using a piezoelectric tube scanner. A diode laser is focused onto the backside of the cantilever and reflected onto a quadrant photodetector as illustrated in Figure 2.1. As the tip is scanned across

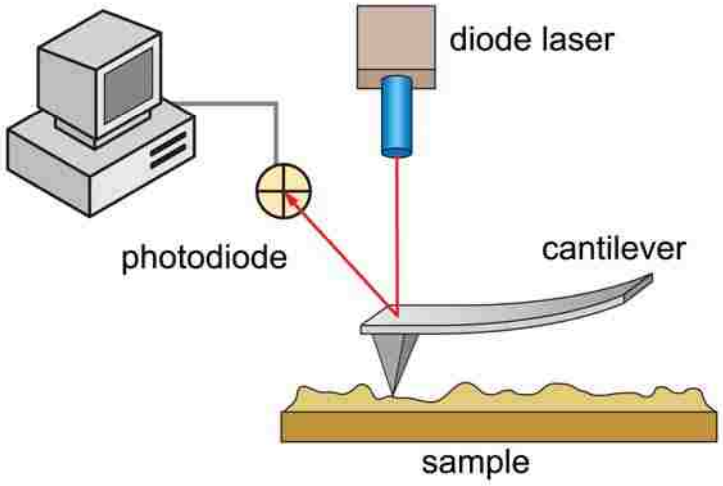

Figure 2.1. Setup for contact mode and lateral force AFM imaging.

the surface in an X-Y raster pattern, attractive and repulsive forces between the tip and the sample cause the cantilever to bend as it profiles the surface features. The tip deflection changes the position of the reflected laser on the quadrant photodiode detector. The feedback loop adjusts the voltages of the piezoscanner to maintain a constant deflection or pressure on the sample surface. A computer records the motion of the tip and a 3-D image is generated of the

surface topography of the sample by mapping the changes in voltage applied through the feedback loop with the X-Y position of the tip.[50, 77-81]

As the tip is scanned across the sample in contact mode AFM, in addition to the vertical attractive and repulsive forces of the surface, it also experiences a torsional twisting. The twisting of the cantilever is caused by friction between the tip and sample caused by nanoscale changes in surface chemistry. Lateral force or frictional force microscopy, which are acquired simultaneously alongside surface topography, display contrast due to friction. Frictional force imaging is useful when studying the inhomogeneity of sample surfaces, and provides a sensitive map of chemical differences for discriminating changes in surface chemistry and adhesion.

An example of contact mode imaging is shown in Figure 2.2 displaying gold nanoparticles which were dropcast on a glass surface. The topography frame is shown on the left in Figure 2.2A, the dark areas represent shallow areas and the bright colors correspond to

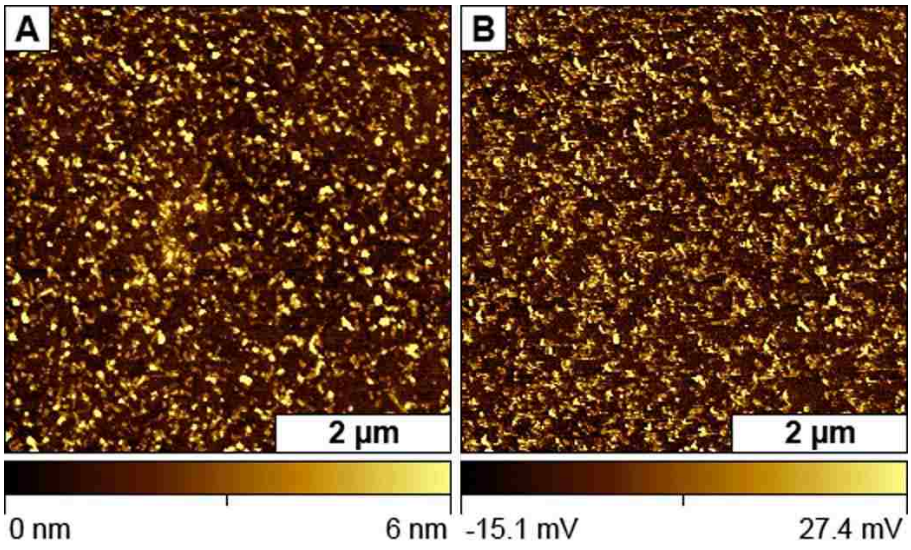

Figure 2.2. Contact mode AFM images of gold nanoparticles deposited on glass. (A) Topography and (B) friction images acquired in an ambient environment.

taller features. The image on the right (Figure 2.2B) shows the simultaneously acquired friction or lateral force image. Areas of higher or lower friction can be arbitrarily scaled with different

colors. Assigning regions of higher or lower friction requires prior knowledge of the nature of the sample. In the absence of hysteresis, trace and retrace friction images can be digitally subtracted to reveal differences in surface friction, for well-aligned scanners.

2.3 Force Modulation AFM

Force modulation AFM is a continuous contact imaging mode used to map differences in the elasticity of a sample. For force modulation AFM, the entire sample is induced to vibrate while the tip is scanned in continuous contact with the sample surface (Figure 2.3). The sample

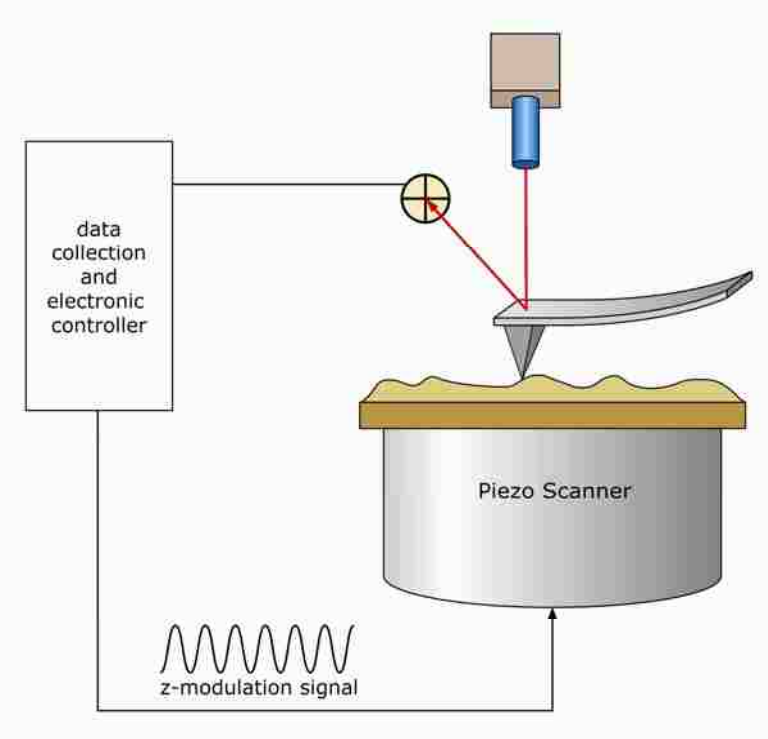

Figure 2.3. Instrument set-up for force modulation AFM.

is driven to oscillate at a selected frequency and amplitude while using the force-deflection feedback loop typical of contact mode AFM. When the modulated surface is interrogated by the AFM tip, energy transfer causes the cantilever to vibrate. Amplitude and phase signals are generated simultaneously with acquisition of topographic information. The dampening or

enhancement of the amplitude and phase components of the cantilever vibration depends sensitively on the softness and viscoelastic properties of the sample.[52, 82-84] Force modulation experiments have investigated the Young's modulus of nanostructures composed of self-assembled monolayers.[71]

2.4 Tapping Mode and Phase Imaging

Tapping mode is an intermittent imaging mode of AFM, which uses an oscillating cantilever to minimize stick-slip adhesion during contact between the tip and the sample. Tapping mode offers advantages for imaging samples that are loosely bound to the surface or for samples that are sticky or fragile. The tip is driven to oscillate at its resonant frequency and is brought close to the sample surface to intermittently "tap" the surface at the chosen frequency and desired amplitude. For ambient imaging in air, the typical resonant frequency of tapping mode tips ranges from 160 to 300 kHz, whereas softer tips with resonances below 100 kHz can be used for tapping mode imaging in liquid media. Typically, the tip is affixed to a small piezoceramic chip to drive the mechanical actuation for tip vibration (Figure 2.4). As the tip is

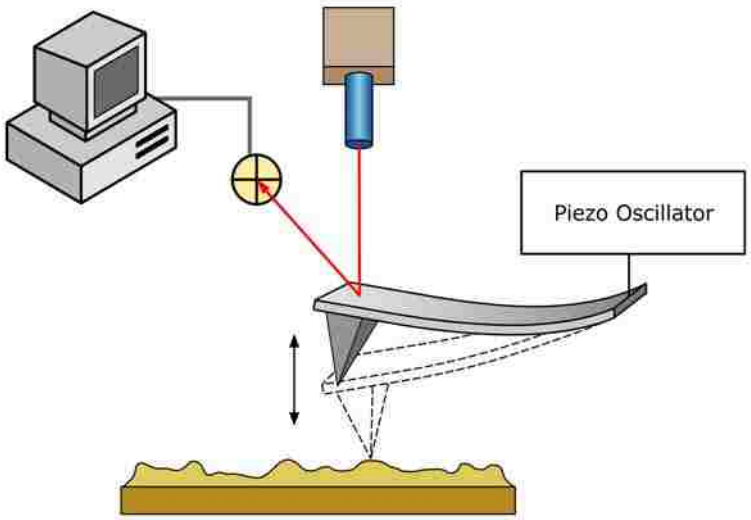

Figure 2.4. Instrument configuration for tapping mode.

scanned in intermittent contact with the surface, the feedback loop maintains a constant amplitude of tip oscillation. The voltage changes applied to maintain the amplitude are reconstructed to form an amplitude image. Phase data is obtained from the phase lag between the AC input which drives the oscillation and the cantilever oscillation output. Phase images can be used to view differences in material properties due to differences in surface chemistry. Topography, amplitude, and phase data are obtained simultaneously. [54, 55, 85-87]

An example tapping mode image is shown in Figure 2.5. Frames of the topography and phase channels for an 8×8 μm^2 scan area of the surface of 300 nm polystyrene latex is displayed, revealing the hexagonal packing arrangement of monodisperse spheres. Figure 2.5A displays a topography image acquired in ambient air, with a z-scale of 130 nm and Figure 2.5B shows the simultaneously acquired phase image.

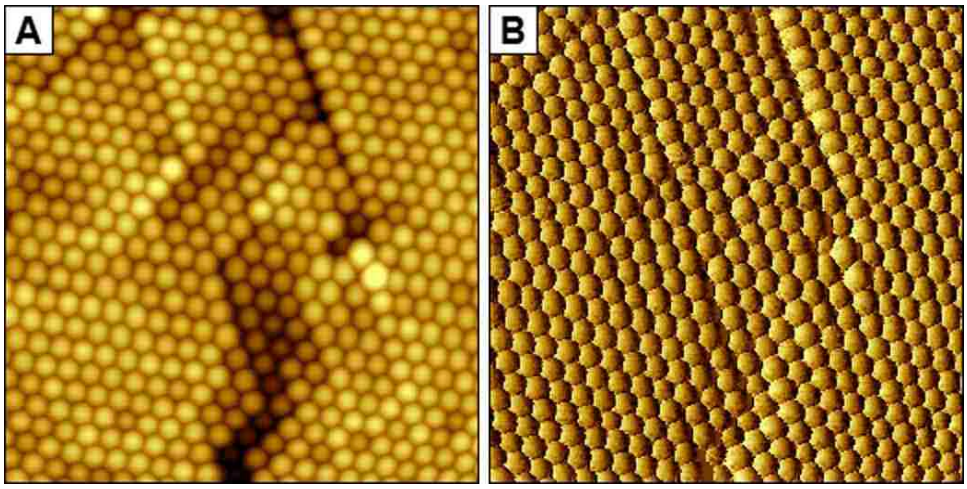

Figure 2.5. Tapping mode images of 300 nm polystyrene latex film. (A) Topography and (B) phase image.

2.5 Magnetic AC Mode AFM

Magnetic AC (MAC) mode is used to accomplish tapping mode AFM with an alternating electromagnetic field to drive the oscillation of a magnetically coated probe.[88-92] For MAC

mode, an AC current is applied to a solenoid located beneath the sample stage to generate an electromagnetic field which alternates in polarity, frequency and strength (Figure 2.6). The alternating electromagnetic field precisely drives the actuation of a cantilever which has a

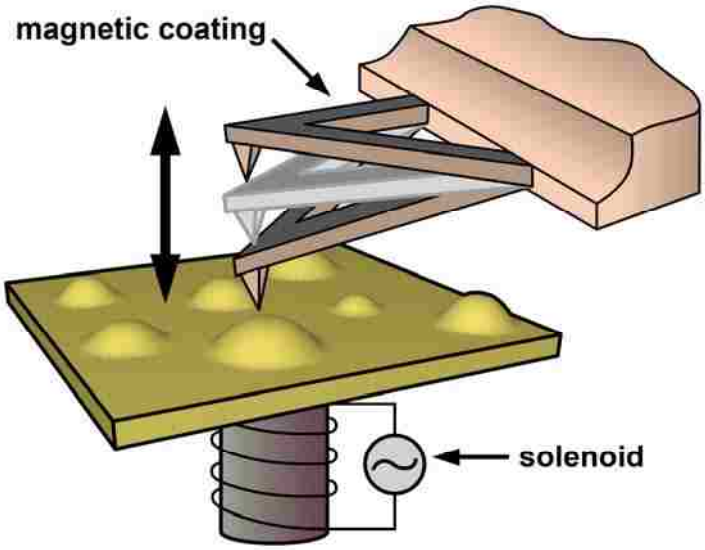

Figure 2.6. Setup for MAC mode.

magnetic coating on the top side of the probe. Better resolution can be often be achieved with MAC-mode because only the cantilever is being modulated as opposed to the entire cantilever holder attached to the piezoelectric actuator. Essentially, MAC mode uses the same amplitude-based feedback loop as for tapping mode. The key difference between MAC-mode and conventional acoustic tapping mode is that a magnetic coating is required for MAC mode imaging, and tip actuation is driven directly by an electromagnetic field.

2.6 Magnetic Force Microscopy

The conventional imaging mode used for the detection of magnetic forces is known as magnetic force microscopy (MFM).[73, 93-97] For MFM, the bottom side of an AFM probe is coated with a magnetic metal film (Figure 2.7). The tip is first scanned in contact mode and the

topographic line trace is memorized. The tip is then withdrawn from the surface at a selected height and is operated in non-contact mode while following the memorized topographic trace. The tip is rastered at a fixed distance from the sample and used as a magnetic force sensor to detect the relatively weak long range magnetic forces of areas of surfaces. The attraction and

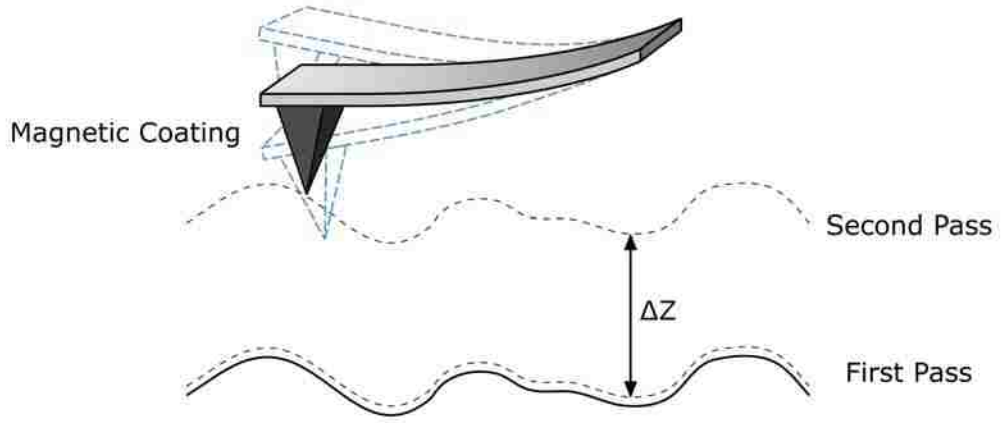

Figure 2.7. Operating principle for magnetic force microscopy.

repulsion of the tip by magnetic domains of a sample cause the cantilever to bend. This approach provides a means to map the strength of the magnetic field at various distances (e.g. 50, 100, 150 nm) from the surface. Weaker magnetic forces do not influence the tip over great distances. This limits the resolution of MFM to magnetic domains of 200-500 nm.

A practical example of MFM is shown in Figure 2.8 for a sample of magnetic film from a zip data diskette. From the topography image, little can be determined about the chemical or magnetic structure of the surface. However, in the MSM channel of Figure 2.8B the magnetic domains of the memory device are visible as light and dark bands. The bright bands indicate that the magnetized tip is repelled by the magnetic field of the surface, whereas the dark bands display attractive forces for the magnetic probe.

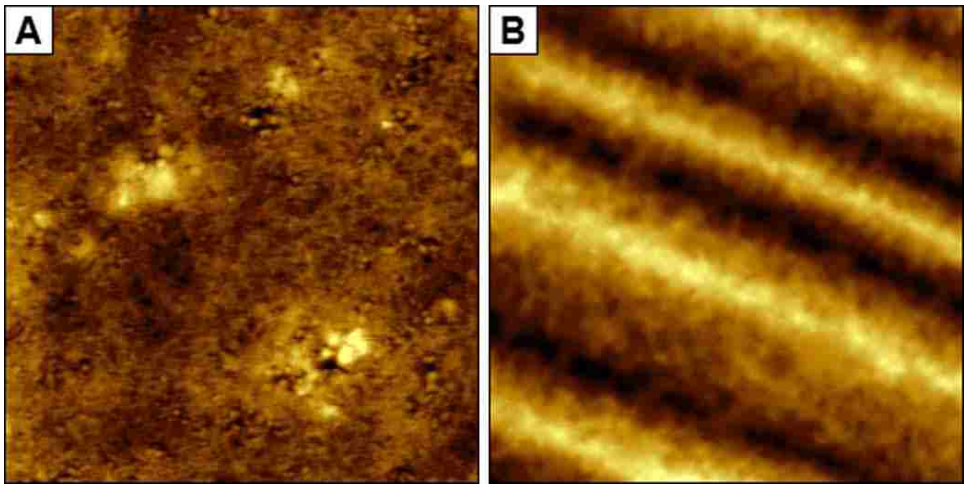

Figure 2.8. Magnetic force microscopy (MFM) images of the surface of the polymer film taken from a zip disk, scan size is 8×8 μm^2, the topography z-scale is 60 nm. (A) Topography image; (B) magnetic image.

2.7 Magnetic Sample Modulation

Several measurement modes with SPM provide surface characterizations for evaluating magnetic properties of surfaces. Imaging modes such as magnetic resonance force microscopy (MRFM)[98-101] and magnetic force modulation[102-105] require the use of tips with a magnetic coating. Magnetic probes can be problematic, since the magnetic properties of the thin metal films which coat the underside of the probes diminish over time, requiring remagnetization. Also, after continuous contact mode scanning, the thin metal films can be worn away. The thickness of the magnetic coatings is on the order of tens of nanometers, which greatly decreases the resolution for imaging small surface features. Intrinsically, the resolution of SPM methods depends on the geometry of the coated probe; and metal coatings produce relatively large, blunt tips.

This section presents a new approach for mapping the magnetic response of nanomaterials by combining magnetic sample modulation with contact mode AFM. In contrast to magnetic force microscopy, magnetic sample modulation imaging requires nonmagnetic

probes and the mechanical response of materials to an external magnetic field is used to map the magnetic domains. This new imaging mode has the potential to advance the resolution of magnetic imaging beyond that which is currently possible with MFM.

This new imaging mode employs a standard, soft, nonmagnetic AFM cantilever operated in contact mode for detecting the physical motion of nanoparticles which are driven to vibrate by an AC electromagnetic field. As shown in Figure 2.9, a solenoid is located underneath the sample, to which an AC voltage is applied, producing an alternating magnetic field. The flux of the alternating magnetic field causes the magnetic materials on the surface to vibrate. The periodic motion of the sample vibration can be tracked by changes in the deflection of the tip. As the tip is rastered across the surface in contact mode, the movement of the magnetic materials causes the tip to vibrate when it touches the vibrating domains. The mechanical motion of the magnetic material is sensitively detected by a scanning AFM tip. Only the magnetic materials vibrate when the alternating magnetic field is applied, providing selective contrast.

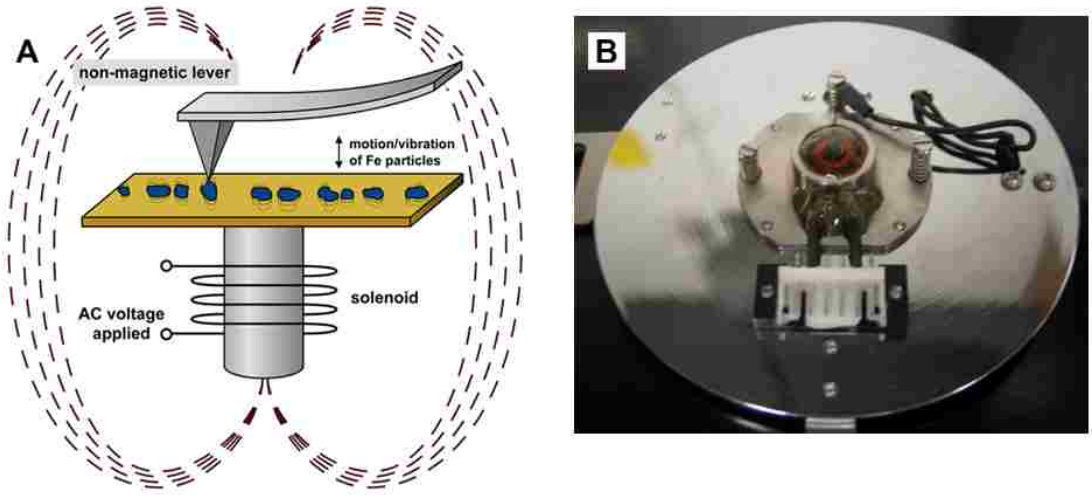

Figure 2.9. Imaging concept for magnetic sample modulation. (A) Instrument setup, (B) photograph of solenoid located beneath the sample plate.

The instrument setup for MSM is a hybrid of three imaging modes, in which the tip is operated in contact mode using a MAC mode sample plate to apply an alternating magnetic field for selective modulation of magnetic domains. Essentially, MSM is a variant of force modulation AFM with selectivity for actuating and characterizing magnetic nanomaterials. To visualize the magnetic domains of a sample, conventional contact mode images are first acquired without applying a magnetic field. Next, the same area of the surface is scanned again with an alternating electromagnetic field applied. The polarity, oscillation and flux of the magnetic field are generated and controlled by selection of parameters for the AC current applied to the wire coil solenoid, which is located underneath the sample plate embedded within an epoxy resin shown in Figure 2.9 B. When an electromagnetic field is applied to samples, only the magnetic domains are driven to vibrate, providing selective contrast for areas that are in motion. A lock-in amplifier is used to acquire the amplitude and phase components of the deflection signals, which furnishes exquisite sensitivity for slight changes in tip movement. The changes in phase and amplitude as the tip interacts with the vibrating sample are plotted as a function of tip position to create MSM phase and amplitude images. The differences displayed for images with and without an applied magnetic field are used to map areas of magnetic nanomaterials.

Magnetic sample modulation was applied to characterize micropatterned stripes of iron oxide nanoparticles. Figure 2.10 showcases an experiment providing proof-of-concept images of MSM applied for microstripes of iron nanoparticles. A topography image of the stripes of nanoparticles is shown in Figure 2.10A and Figure 2.10B is the simultaneously acquired phase image. In the top images, no magnetic field was applied. The bottom row of images was taken when the alternating magnetic field was activated. In the presence of a magnetic flux, the

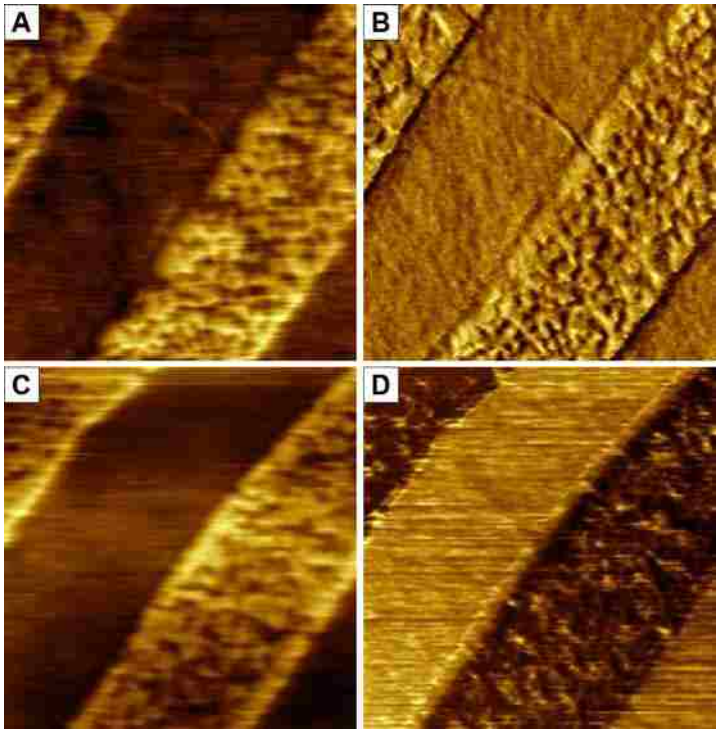

Figure 2.10. Contact mode images of micropatterned stripes of iron nanoparticles acquired with magnetic sample modulation (MSM). (A) Topography and (B) phase image without an applied AC electromagnetic field. Views of (C) topography and (D) phase channels with the AC electromagnetic field turned on.

topography view of Figure 2.10C is indistinguishable from that of Figure 2.10A. However, the magnitude and contrast of the MSM phase image has become more apparent in Figure 2.10D.

CHAPTER 3. NANOSTRUCTURES OF CYSTEINE-COATED CdS NANOPARTICLES PRODUCED WITH "TWO-PARTICLE" LITHOGRAPHY

3.1 Introduction

Organizing and arranging materials on surfaces with nanometer-level spatial control has proven to be a considerable challenge in nanotechnology. There are few tools for writing or inscribing structures at the nanoscale, and most lithography techniques for producing ultrasmall dimensions are expensive, difficult to accomplish and rely on stepwise serial processes of writing or inscribing patterns. With particle lithography, conventional bench chemistry methods of mixing, centrifuging, evaporation and rinsing can produce high density arrays of nanostructures. The patterning mechanism for particle lithography is based on spontaneous processes of solution self-assembly of monodisperse colloidal mesoparticles on flat surfaces. Using particle lithography, we have developed a new approach to control the surface coverage and arrangement of quantum dots such as cysteine-coated CdS nanoparticles.

The optical properties of semiconductor and metal nanocrystals not only depend on the size of the nanoparticles, but are also influenced by the arrangement and spacing on surfaces. Both long and short-range ordering in thin films greatly affect the overall light scattering, absorption, and luminescence. Methods have been developed to produce regular superstructures of metal, semiconductor and magnetic nanoparticles.[106-110] The spacing between adjacent nanoparticles has been found to affect plasmon resonance properties for distances below 200 nm.[111-117] Ensembles of organized metal and semiconductor nanocrystals can be applied for measurements of physical properties as well as for tuning optical and electronic properties for device applications.[118] The self-organization of nanoparticles into superlattices requires size distributions that are highly monodisperse to generate long-range order without defects.

*Reproduced with permission from the American Chemical Society.

Particle lithography, which has also been referred to as nanosphere lithography, uses submicron-sized spherical particles as either a mask or template to produce nanostructures on surfaces. Particle lithography has been applied to generate arrays of nanostructures of polymers,[119-122] proteins,[35, 36, 123, 124] metals,[25, 125-136] and self-assembled monolayers.[47, 137-139] Particle lithography has not previously been applied to directly pattern nanoparticles, such as quantum dots. The variety of nanostructures that can be generated using particle lithography include vertical rods/pillars,[140, 141] 2D and 3D arrays of nanoparticles,[142-145] metal oxides,[146, 147] and silica;[148] porous membranes of polyurethane;[149] and 3D opal or reversed opal photonic band gap materials of silicon or titanium dioxide.[150] There is a practical problem when using colloidal masks for patterning materials through sequential immersion steps, such as for preparing organic thin films by solution self-assembly. Because of the buoyancy of the mesoparticles in various liquids, silica and latex spheres rapidly detach from surfaces when immersed in solutions of water or solvents. Therefore, strategies need to be devised for particle lithography without direct immersion of mesosphere templates to form patterns. To overcome this problem, liquid transfer from an inked PDMS stamp[138, 139] or vapor deposition[47] has been applied to pattern organic monolayers with mesoparticle masks.

For optically active nanostructures, the diameters of templating mesospheres can be used to tailor the plasmonic properties of surfaces with periodic arrangements of nanoparticles.[151] Arrays of nanoparticles may provide useful structures for applications based on localized surface plasmon resonance (LSPR)[26, 152, 153] and surface-enhanced Raman scattering (SERS).[154-158] For applications in the field of photonic band gap materials, it is particularly important to develop methods of producing colloidal crystals with few defects for millimeter size scales. Researchers have developed approaches to minimize the density of defects for particle lithography by use of

fabrication steps such as using convective assembly,[159] sonication,[160] spin-coating,[161] shear force alignment,[162] Peltier cooling,[130] Langmuir-Blodgett troughs[163] or directing the sample orientation under gravitational forces.[164]

Nanoparticles such as semiconductor quantum dots exhibit stable fluorescence and are promising alternatives to organic dyes for investigations which require biological labeling.[165-167] However, concerns have been raised about the potential cytotoxicity of nanoparticles because of the toxic elements of the core materials (e.g., cadmium, selenium). In certain cases, quantum dots can be rendered nontoxic with biocompatible coatings.[168, 169] For example, nanoparticles of CdS have been passivated using organic ligands,[170-175] peptides,[176, 177] DNA,[178, 179] proteins[180] and cysteine.[181, 182]

We have developed a new approach of "two-particle" lithography by mixing latex or silica mesospheres with nanoparticles in aqueous solution. Monodisperse mesoparticles self-assemble into close-packed crystalline arrays on surfaces such as mica(0001) providing a structural template to direct the adsorption and placement of nanoparticles. As solutions dry, nanoparticles surround the templates, filling in the interstitial void spaces of the surface between spheres. Mesospheres can be efficiently removed by a simple rinsing step to disclose periodic arrays of nanoparticles. The CdS nanoparticles for these investigations were capped with cysteine and were relatively polydisperse. Depending on the concentration and ratios of smaller particles, the patterns generated on surfaces are either pores within a film of nanoparticles, or arrays of ring structures. The arrays exhibit uniform geometries and periodicity, spanning micron-sized areas. The density and periodicity of the arrays can be controlled by choosing the diameters of the mesospheres and ratios of nanoparticles.

3.2 Experimental Section

3.2.1 Materials and Reagents

Tris buffer (tris(hydroxymethyl)aminomethane), hydrochloric acid, L-cysteine, cadmium sulfate, sodium sulfide nonahydrate, and other routine chemicals were purchased from Sigma-Aldrich (St. Louis, MO) as ACS reagent grade or higher. Ultrapure 18.2 MΩ·cm distilled deionized water was used in all experiments. Monodisperse latex and silica spheres were acquired from Duke Scientific (Palo Alto, CA).

3.2.2 Synthesis of Cysteine-Coated CdS Nanoparticles

The colloidal aqueous synthesis of cysteine-capped CdS nanoparticles was adapted from a procedure reported by Mehra and coworkers in which they reported formation of particles ranging in size from 2 nm to 4 nm.[183] Briefly, 0.25 M solution of L-cysteine was prepared in nitrogen-saturated Tris buffer (1 M). A solution with a final cysteine to cadmium ratio of 2:1 was prepared by adding 20 mL $CdSO_4$ (~0.03 M in 0.01 N HCl) to 5 mL of cysteine solution while vortexing. Sodium sulfide (0.5 M in water) was then titrated into the solutions while vortexing to obtain S:Cd molar ratios of 0.25, 0.50, 0.75, 1.00, 1.50, and 2.00. The samples were sealed and incubated for 60 min at 45ºC, followed by 10 min of N_2 flushing to remove most of the unreacted sulfide. Ethanol precipitations and centrifugations were used to remove free cysteine. Cold ethanol was added drop-wise with continuous mixing until precipitation was formed. The precipitates were recovered by centrifugation and the supernatant removed. The precipitates were redissolved in 1 M Tris buffer and the ethanol precipitation repeated four times. The recovered solids from the final step were dissolved in water for spectroscopic characterization. The approximate sizes of the particles were estimated based upon the size dependence of the lowest excited state of the semiconductor particles[184, 185] and through empirically derived sizing curves that relate spectral properties to physical measurements.[186]

The synthesis procedure typically resulted in particles with diameters estimated to be in the range of ca. 1 to 4 nm, increasing as the S:Cd molar ratio was increased. The expected size dependent luminescence was also observed upon illumination with a black light. A lyophilizer used to remove water yielding a stable re-dispersible product. Powders from the lowest ratio preparation, the preparation resulting in the smallest particles, were redispersed in water for AFM characterization and patterning.

3.2.3 Preparation of Substrates

Ruby muscovite mica (S&J Trading Co., NY) was used for atomic force microscopy (AFM) investigations. Pieces of mica (1×1 cm^2) were cut and cleaved immediately before depositing sample solutions.

3.2.4 Atomic Force Microscopy

Images were acquired using an Agilent 5500 scanning probe microscope (SPM) equipped with Picoscan v5.3.3 software. Digital images were processed using Gwyddion (version 2.9) open source software, which is freely available on the Internet.[187] An ambient environment was used for either contact mode (Figures 2, 4, and 6) or intermittent contact imaging with acoustic AC (AAC) mode (Figures 3 and 5). Rectangular silicon nitride cantilevers (MSCT-AUHW, resonance frequency 85-155 kHz, spring constant 0.50 N/m) from Veeco Probes (Camarillo, CA) and silicon AFM probes (PPP-NCL, resonance frequency 155 kHz) with an aluminum reflex coating from Nanosensors (Neuchatel, Switzerland) were used for imaging.

3.2.5 Procedure for "Two-Particle" Lithography

A solution of monodisperse mesospheres (200-800 nm) is mixed with smaller nanoparticles (diameter < 50 nm) at a given ratio, for two-particle lithography. The basic chemistry steps are outlined in Figure 3.1. First, an aqueous solution of monodisperse latex or

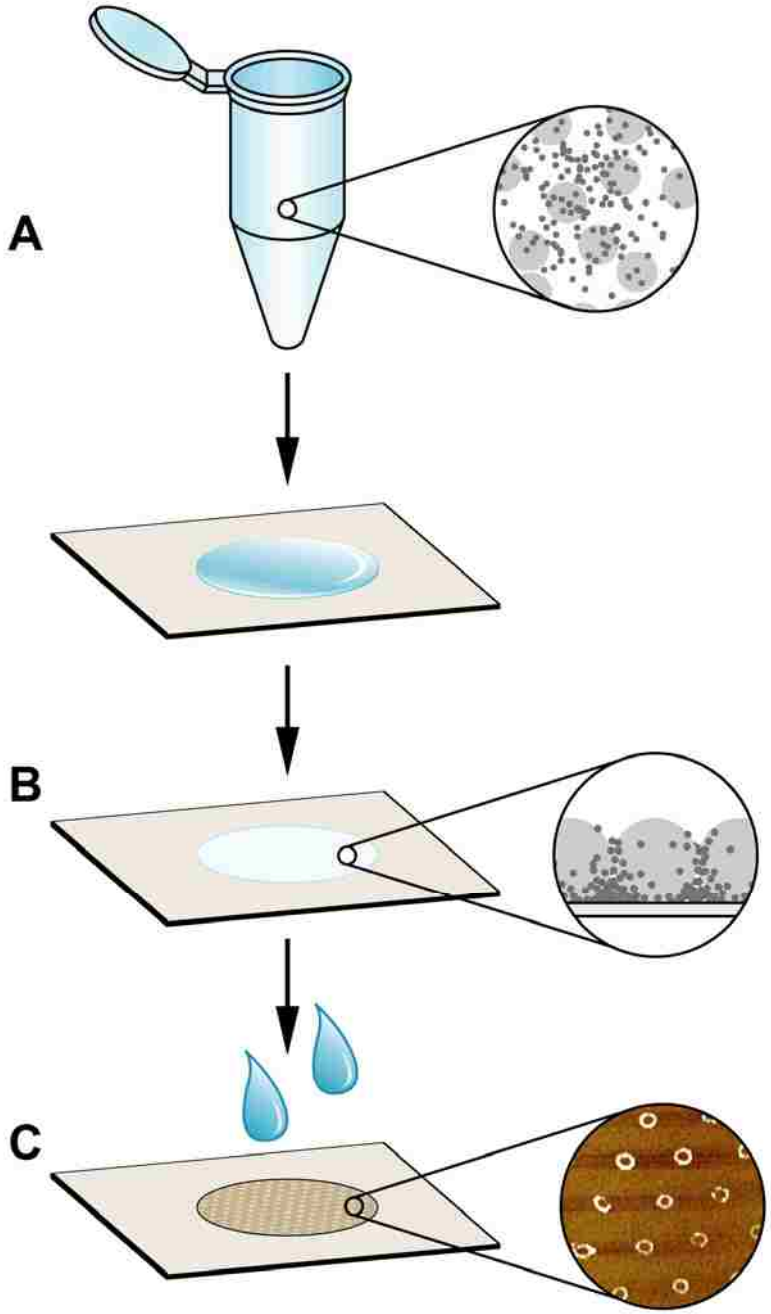

Figure 3.1. Procedure for "two-particle" lithography. (A) Mesospheres and nanoparticles are mixed; (B) a drop of sample is dried; (C) mesospheres are rinsed away.

silica mesoparticles is centrifuged and rinsed to remove surfactants or other contaminants. The centrifuge speed and duration are chosen to produce a clear supernatant, in the range of 10-20

min at 14,000 rpm. The pellet is then resuspended in deionized water for one rinsing cycle by centrifugation. In the next step, the rinsed pellet of mesospheres is resuspended in the desired volume of an aqueous solution containing nanoparticles. A small volume (10 μL) of the mixture of nanoparticles and mesospheres is deposited onto the substrate, e.g. pieces of freshly cleaved mica (1×1 cm^2). The droplet of sample is then dried in air at room temperature, with relative humidity ranging from 40-70%. This method is commonly used for preparation of samples for SPM referred to as "dropcasting" or drop deposition. After drying, the larger mesospheres can be efficiently and completely rinsed away using ethanol or water, to leave the nanoparticles adsorbed to the surface in patterned arrangements which conform to the periodicity of the structural template of mesospheres.

3.3 SPM Characterization and Size Analysis of Nanoparticles

For these investigations, CdS nanoparticles were functionalized with cysteine as a capping agent. Samples were analyzed using contact-mode AFM (Figure 3.2) to obtain information about the size and dispersity of the nanoparticles. The topography and frictional force images were acquired simultaneously and provide maps of the morphology and surface chemistry, respectively. The cysteine-coated nanoparticles were diluted in water and deposited on mica substrates to dry. The hydrophilic nature of mica provides a means to disperse nanoparticles across the surface and to minimize self-aggregation. Two different size ranges are apparent in the AFM images; the smaller adsorbates (less than 0.5 nm) correspond to residues of excess cysteine which are present in the parent sample. Evidence for the differences in surface composition of the two materials is provided in the frictional force image of Figure 2B, which displays markedly distinct colors for the different materials. Friction images map changes in surface chemistry which result from differences in tip-surface adhesion as the sample is scanned by the AFM probe. For example, the atomically smooth and flat areas of mica reflect a different

color contrast than the adhesive areas of cysteine or nanoparticles. To determine which adsorbates are cysteine and which are CdS nanoparticles the topography and frictional force images can be compared side-by-side. Cysteine has approximate dimensions of 0.8 nm, which matches well with the thickness of the smaller adsorbates.[188] The smaller adsorbate particles with a dark color correspond to cysteine residues, whereas the larger particles with a bright color are CdS nanoparticles.

The diameters of the cysteine-coated nanoparticles were measured by acquiring cursor measurements of the heights of individual nanoparticles. In AFM topography images the lateral dimensions of nanoparticles are distorted by the geometry of the probes. However, measurements in the z-direction correlate accurately with the nanoparticle diameters. For the sample presented in Figure 3.2A, the average size of the nanoparticles is 1.7 ± 0.7 nm, ranging from 0.9 to 3.5 nm in diameter (n = 44).

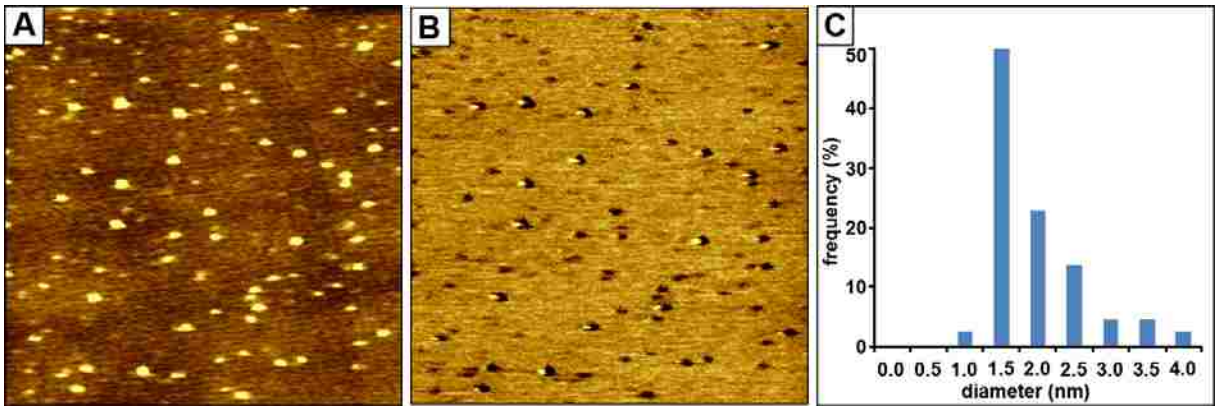

Figure 3.2. Cysteine-coated CdS nanoparticles dried on mica(0001). (A) Contact mode topography image (7 × 7 μm^2); (B) corresponding frictional force image; (C) size distribution from multiple cursor height measurements.

3.4 Structural Templates of Latex

The ex situ steps of patterning with mesospheres and nanoparticles can be characterized using AFM throughout the fabrication process. The top surface of latex mesospheres used as a

structural template in two-particle lithography is viewed in Figure 3.3, before the rinsing step. Basically the larger spheres provide a rigid structure to direct the arrangement of nanoparticles during drying. As water evaporates from the mixture of two particles (mesospheres and nanoparticles) convective forces drive the larger latex or silica spheres to assemble into a close-packed hexagonal array (Figure 3.3A).[143] The periodicity and arrangement of the structural templates dictates the surface organization of the nanoparticles (Figure 3.3B). The nanoparticles are pulled towards the surface and surround the larger mesospheres during the drying step. The smaller nanoparticles, which are not visible during this step, migrate to the bottom areas surrounding the template spheres. For monodisperse samples of latex or silica mesospheres, a close-packed arrangement is produced spontaneously when solutions are dried on atomically flat surfaces.

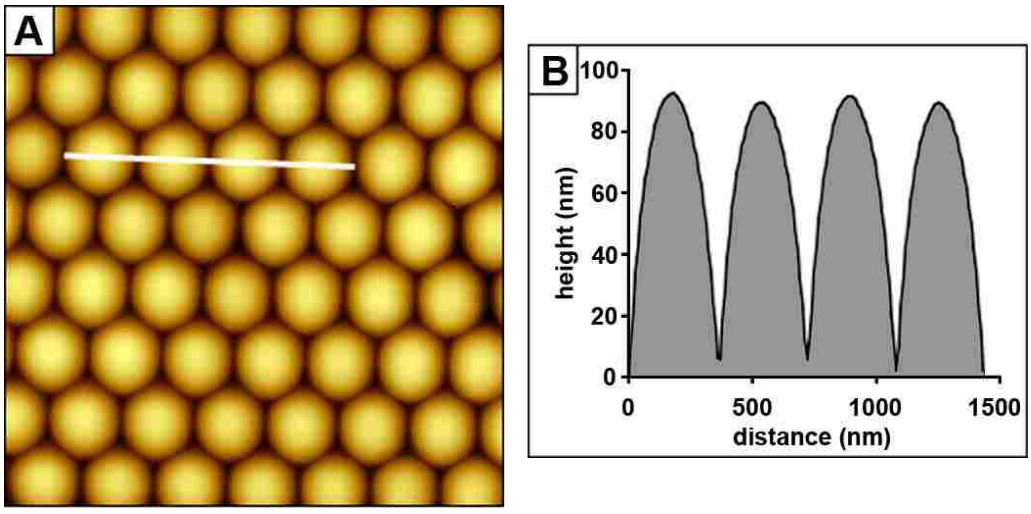

Figure 3.3. The natural self-assembly of monodisperse latex mesospheres furnish a structural template for two-particle lithography, to guide the adsorption of nanoparticles on surfaces. (A) AAC mode topograph of 300 nm latex (2.5 × 2.5 μm2); (B) cursor line profile for A.

The mesospheres mask circular areas of the surface to form a crystalline, close-packed structure. The tightly packed spheres do not fully cover all areas of the surface; small exposed

areas in between spheres provide a network of narrow capillary channels for solutions to migrate to the surface. The nanoparticles are carried with the liquid meniscus during the drying step to form regular, evenly distributed arrangements of nanoparticles deposited near the base of the template mesospheres. After the surface is rinsed, the mesospheres are completely displaced, whereas the nanoparticles persist and are not removed from the surface. Several factors contribute to the facile removal of mesospheres by simple rinsing. There is relatively weak adhesion between the mesospheres and the mica substrate. The buoyant properties of the spheres provide a mechanism for flotation, and the particles swell and expand when water is introduced. However, the cysteine-coated nanoparticles remain securely attached to the surface despite rinsing, to form a 2D array of circular nanopatterns organized with a periodicity corresponding to the diameters of the template mesospheres.

After rinsing away the latex structural template for the sample of Figure 3.3, cysteine-coated nanoparticles remain attached to the surface to form well-defined circular patterns. The geometries and arrangement of the rings are viewed with contact mode topography images in Figure 3.4. The nanopatterns are highly symmetric, with uniform geometries and periodicity matching the organization and diameters of the structural templates. A view of 105 ring structures is provided within the $3.3 \times 3.3\ \mu m^2$ frame of Figure 3.4A. Scaling up to macroscopic dimensions, this would extrapolate to 900 million nanostuctures for a $1 \times 1\ cm^2$ area. Approximately 21% of the surface is covered by rings of nanoparticles, estimated using digital image analysis.[189] The corresponding frictional force image (Figure 3.4B) displays differences in surface composition between the rings of nanoparticles and other areas of the surface. In this example, the bright areas have higher friction, resulting from stronger adhesive interactions between the tip and rings of cysteine-coated CdS nanoparticles. Notice that the frictional

contrast of the areas between the rings of nanoparticles is different than the dark areas inside the circle. The interstitial areas between the rings of nanoparticles are an intermediate color, and correspond to residues of cysteine.

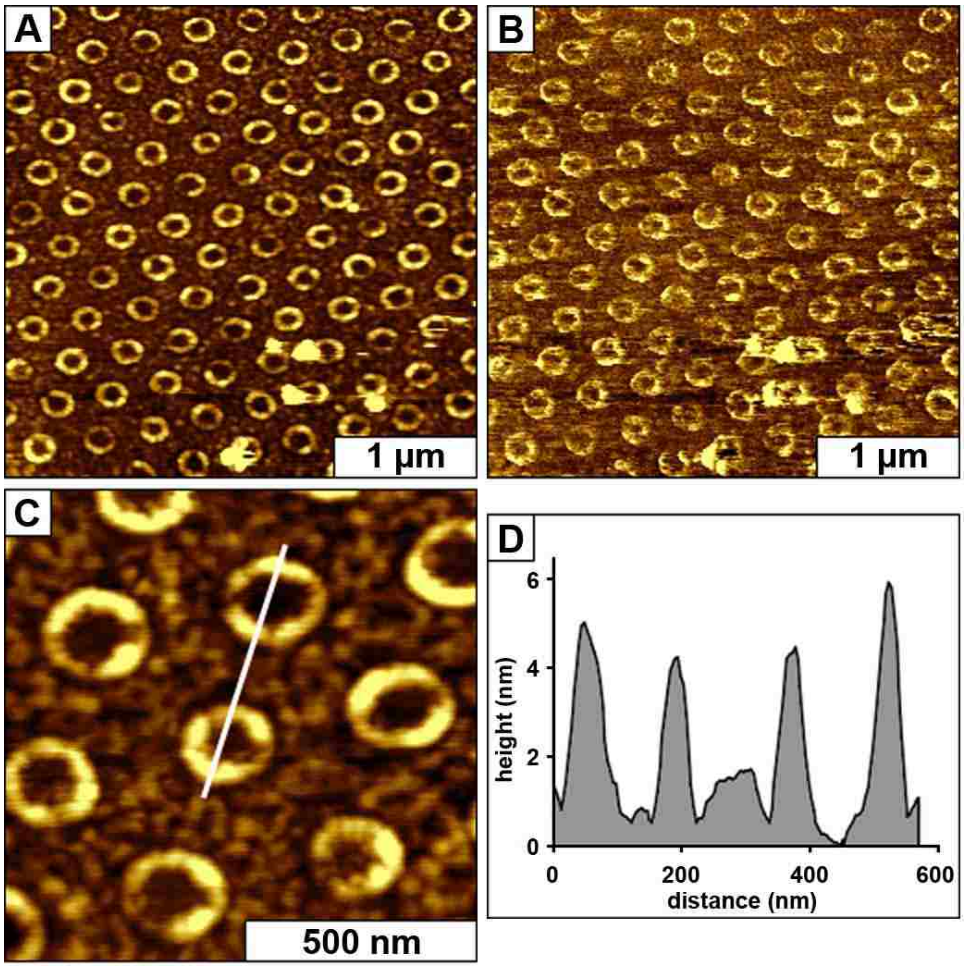

Figure 3.4. Rings of cysteine-coated CdS nanoparticles formed using a structural template of 300 nm latex mesospheres. (A) Contact mode topography image; (B) corresponding frictional force image; (C) zoom-in view of A; (D) line profile for C.

A zoom view of the hexagonal arrangement of seven nanostructures (1×1 µm^2) is presented in Figure 3.4C. The diameter of the rings measures approximately 180 nm across, and there are 9-14 nanoparticles forming each ring. The average periodicity measures 320 ± 12 nm, which closely matches the expected diameter (300 ± 6 nm) of the latex template. The center-to-

center spacing between adjacent rings corresponds to the periodicity of the latex; however the size of the rings is somewhat smaller. The diameter of the rings is established by the area of contact between the mesosphere and surface. The uncovered areas of the substrate inside the rings of nanoparticles provide a baseline for height measurements. A representative line profile across two ring structures is shown in Figure 3.4D. The height of the rings measures 5.6 ± 0.9 nm. An intermediate height is observed between the rings of nanoparticles, which is attributed to clusters of adsorbates of unreacted cysteine. The ring structures of nanoparticles are uniformly distributed throughout areas of the surface, according to the regular periodic arrangement of the 300 nm latex templates. The AFM images are representative views of the morphologies observed for multiple areas of the surface.

3.5 Structural Templates of Colloidal Silica

Mesospheres of colloidal silica can also be used as structural templates for two-particle lithography. Nanopatterns of cysteine-coated CdS nanoparticles were formed using 500 nm silica spheres as a template (Figure 3.5). The diameters of the mesospheres can conveniently be

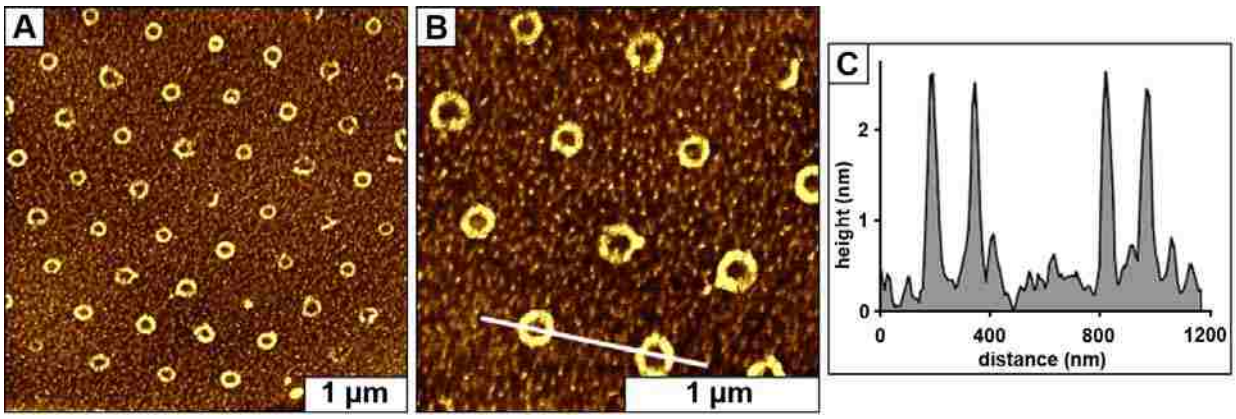

Figure 3.5. Ring structures of cysteine-coated CdS nanoparticles produced using 500 nm silica spheres as a template. (A) Topography image acquired using AAC mode; (B) zoom in view of A; (C) line profile for B.

used to tailor the periodicity of the arrays of ring structures. A topographic view is displayed for a 4×4 μm^2 area of the ring structures of cysteine-coated CdS nanoparticles (Figure 3.5A). The rings have a diameter of 140 ± 12 nm. The diameters for rings formed with colloidal silica as the templating particle are smaller than when polystyrene latex was used. Colloidal silica spheres are more mechanically robust than latex beads. Polysytrene latex deforms upon drying, which increases the contact area between the mesoparticle and the surface, thereby increasing the diameter of the ring patterns.[138, 190, 191] Approximately 10% of the surface is covered by nanostructures. Twelve rings of nanoparticles are visible within the 2×2 μm^2 frame of Figure 3.5B. This scales to 300 million nanostructures for a 1×1 cm^2 area. A cross section across two ring structures (Figure 3.5C) indicates that the rings measure 1.9 ± 0.6 nm in height, which matches the thickness of a single layer of nanoparticles. Areas between the rings contain adsorbates of unbound cysteine. There are also bright spots interspersed throughout the regions between the ring patterns, which are cysteine-coated CdS nanoparticles. The cross section (Figure 3.5C) displays a bumpy baseline, where nanoparticles have filled in the areas of the surface between the rings.

3.6 Changes in Surface Coverage with Different Ratios of Particles

Structures of continuous films with uncovered regular pores can be produced using higher concentrations of nanoparticles. An example of pore morphologies produced within a 2.5×2.5 μm^2 area using 300 nm latex spheres as the templating mesospheres is shown in Figure 3.6A. Forty-seven pores are visible within this image, with an average diameter measuring 210 ± 16 nm. A height profile of four pore areas is presented in Figure 3.6B. The edges of the pores have a height of 8.5 ± 1.8 nm, which suggests that a multilayer of nanoparticles has formed at the edges of the pores. The areas between the pore structures have heights of several nanometers. This thickness corresponds to a layer of cysteine-coated CdS nanoparticles which have filled the

interstitial regions of the surface between the ring structures. The pattern is discontinuous, revealing areas of uncovered mica substrate. As the latex film is dried, the defects of the templating film produce imperfections. Depending on the drying conditions, the shrinkage and deformability of latex spheres can produce cracks and shifts in the registry of the patterns.

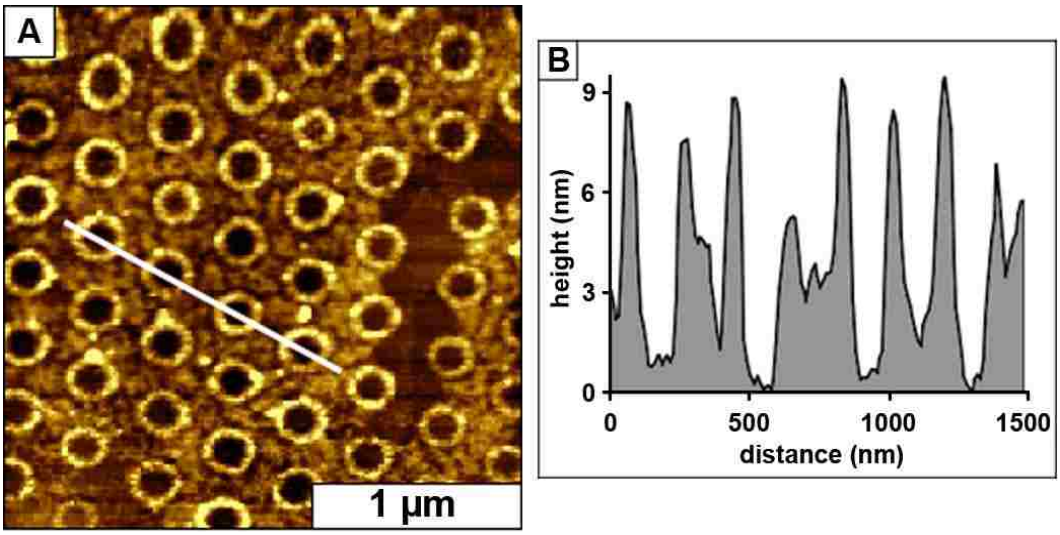

Figure 3.6. Pore nanostructures within a film of cysteine-coated CdS nanoparticles produced using 300 nm latex particles as the template. (A) Topography image acquired with contact mode AFM; (B) line profile for A.

3.7 Discussion

For two-particle lithography, the natural self-assembly of monodisperse mesospheres furnishes a structural template to direct the placement of nanoparticles on surfaces. Since the mesospheres of latex or silica are uniform in size, a close-packed hexagonal arrangement is produced spontaneously when aqueous solutions are dried on flat surfaces (Figure 3.3). The tightly packed mesospheres do not fully cover the surface; areas between spheres provide channels for aqueous solutions of the cysteine-coated CdS nanoparticles to flow to the surface. The cysteine-coated CdS nanoparticles are soluble in water and are carried with the liquid meniscus during the drying step, to form rings around the base of the template spheres. The

areas where the mesospheres are in direct contact with the surface are effectively masked. After the template spheres are rinsed away, the structures of cysteine-coated CdS nanoparticles can be applied for further surface characterizations or assays.

A number of complex interactions are involved in the process of generating nanostructures with two-particle lithography. For the protocol to succeed, the nanoparticles should exhibit strong adhesion to the surface, whereas the structural templates of mesospheres need to adhere weakly. Two-particle lithography has worked successfully with other systems of nanoparticles such as cobalt nanoparticles with an oleic acid and trioctylphosphine oxide[192] and metal nanoparticles encapsulated with plasmid DNA.[43] The adhesion between bare gold nanoparticles and the substrate was not sufficiently strong for the nanostructures to remain attached to the surface during the rinsing step. There should be weak or no adhesion between the nanoparticles and mesospheres, so that only the template spheres are displaced during the rinsing step. Polystyrene latex spheres and colloidal silica have worked successfully as templates, due to their relatively weak adhesion to hydrophilic mica. Another requirement for two-particle lithography is for the substrate to be atomically flat, to minimize defects during the assembly of mesospheres. Thus far, two-particle lithography has been successful with aqueous solutions. When organic solvents were tested for two-particle lithography, the samples dried rapidly and did not generate ordered arrangements of ring patterns. Further investigations are in progress to evaluate cooled conditions during the drying step, to try different solvents and to test the suitability of other substrate materials.

Unlike methods of particle lithography with metal evaporation in vacuum, which generate periodic arrays of triangular structures, solution-based particle lithography produces circular geometries. The examples presented for two-particle lithography display circular or

ring-shaped morphologies when using solution-based approaches for patterning. These nanostructures are quite different from those of previous reports using methods of metal evaporation, which disclose triangular or pyramid nanostructures.[26] Since solution-based particle lithography does not require heated evaporation of metals through a latex mask, the dynamics and mechanisms of patterning are dissimilar. For two-particle lithography, the mesospheres serve as a solid structural template during conditions of ambient drying. As the liquid dries, nanoparticles assemble surrounding the base of latex or silica spheres to generate patterns that conform to the solid shape of the mesosphere templates. The resulting nanostructures of two-particle lithography exhibit circular ring or pore morphologies according to the spherical shape of the mesosphere templates. In contrast, with deposition of heated metal vapors in vacuum, the interstitial void areas produce nanostructures with a triangular or pyramidal shape. For evaporative masks of close-packed mesospheres, line of sight deposition such as metal evaporation will not be able to deposit materials in the areas masked by spheres, thus triangular structures or incomplete rings are generated.

Two-particle lithography provides a convenient and facile means for controlling the surface coverage and density of nanoparticles on surfaces. Once the solution conditions are optimized, replicate samples prepared using a given ratio and particle diameter exhibit reproducible morphologies and periodicity. Surface self-assembly is emerging as an indispensable approach for organizing materials at the molecular scale for practical reasons, such as low cost, applicability to a wide range of nanomaterials and capabilities for high-throughput manufacture of regularly shaped structures. Two-particle lithography provides a viable approach for generating arrays of patterns of nanoparticles using simple steps of bench chemistry (e.g. centrifugation, drying, evaporation, rinsing). Well-defined nanostructures provide precise

reproducible dimensions for investigations of surface properties and furnish test platforms that are suitable for successive characterizations with SPM.

CHAPTER 4. SURFACE CHANGES DURING THE INITIAL STAGES OF WATER CORROSION OF COPPER INVESTIGATED BY ATOMIC FORCE MICROSCOPY: ROLE OF pH AND PHOSPHATES

4.1 Introduction

The primary source of copper in drinking water is from corroding copper pipes in household plumbing. The solubility of corrosion products which have formed on the interior walls of copper pipes determines the level of copper at the consumer's tap. In 1991, the Environmental Protection Agency issued the Lead and Copper Rule which specifies an Action Limit of 1.3 mg/L for copper.[48] If the concentration of copper in more than 10% of customer taps is above this level, then action must be taken to reduce the concentration of copper. This can be accomplished by adjusting either the pH, alkalinity or by addition of corrosion inhibitors. Phosphorous compounds are commonly used as corrosion inhibitors for the protection of metal materials.[193-197] Orthophosphate and hexametaphosphate have been shown to reduce the soluble copper release from corrosion products.[198]

Atomic force microscopy (AFM) is a high resolution imaging technique which furnishes topographic information about surface changes due to corrosion down to the nanoscale. Samples imaged by AFM can be acquired in ambient, liquid, or UHV environments. Unlike macroscopic corrosion studies which take weeks to months for visible changes to occur, corrosion studies using AFM are able to visualize the changes a surface undergoes at the early onset of corrosion. High resolution AFM furnishes an experimental approach to directly view the initial events and formation of corrosion deposits on a surface. Previously, AFM has been applied for studies of the corrosion of materials such as iron,[199] steel,[200-202] silver,[203] glass[204] and copper.[205-208] The effectiveness of corrosion inhibitors has also been evaluated using AFM investigations.[209-211]

The aim of this report was to investigate the early stages of the water corrosion (< 24 h) occurring for a copper surface using high resolution AFM. The evolution of surface changes

over time was studied by using ex situ high resolution AFM, time-of-flight secondary ion mass spectrometry (ToF-SIMS) and x-ray diffractometry (XRD) as specifically influenced by changing pH and orthophosphate levels.

4.2 Experimental Section

4.2.1 Copper Sample Preparation

Pure copper samples (99.9%) were used for the experiments. The copper surfaces were not polished or etched, to simulate the natural conditions of copper plumbing. Samples of copper coupons were cut into 1×1 in^2 squares, and cleaned by sonicating for 5 min in 0.5% Triton X-100® (Curtis Matheson Scientific, Inc., Houston, TX) followed by ultrasonic cleaning in Milli-Q water for 5 minutes. The copper substrates were then rinsed in acetone and dried in air.

4.2.2 Water Sample Preparation

Water samples (1 L) of varied conditions were prepared as detailed in Table 1. The pH of the solutions was adjusted with hydrochloric acid and sodium hydroxide using an automated titrator system (Fisher Scientific). Reagents added to the water solutions were prepared from ACS reagent grade sodium bicarbonate, sodium sulfate, sodium chloride, sodium hypochlorite, and sodium phosphate tribasic (Fisher Scientific). The initial concentrations of chloride, sulfate, phosphate, and other metals were measured with an inductively coupled plasma atomic emission spectrophotometer (ICP-AES).

Table 4.1. Water conditions for immersion of copper samples.

Sample	pH	DIC (mg/L)	Sulfate (mg/L)	Chloride (mg/L)	Chlorine (mg/L)	Orthophosphate (mg/L)
1	9	10	120	60	3	0
2	9	10	120	60	3	6
3	6.5	10	120	60	3	0
4	6.5	10	120	60	3	6

4.2.3 Experimental Setup

Copper samples were suspended by a nylon string in a 1 L glass beaker of water sample with selected chemistry. The beaker was covered with parafilm and the water was stirred at a slow rate. After a certain time interval (4 h or 24 h), the copper samples were removed from the water and dried in air. After drying, the samples were analyzed by AFM.

4.2.4 Surface Analysis

An Agilent 5500 scanning probe instrument equipped with PicoScan version 5.4 software was operated in acoustic AC (AAC) mode and used to aquire AFM images. Tapping mode tips were obtained from Nanosensors (Neuchatel, Switzerland), and had average resonance frequencies ranging from 155 – 170 kHz.

A Scintag (Santa Clara, CA) XDS-2000 diffractometer with a copper x-ray tube was used to acquire x-ray patterns. The tube was operated at 35 or 40 kV and 40 mA. Scans were performed over a 2-theta range between 5 to 90º with a step of 0.02º and a 2 second hold time. Pattern analysis was performed using the MDI Jade XRD pattern processing computer software in conjunction with the ICDD PDF-2 2002 database.

A CAMECA (Gennevilliers, France) ION-TOF model IV instrument equipped with a 25 keV liquid metal (^{69}Ga) ion gun was used for ToF-SIMS analysis. A flood gun was used for charge neutralization. A 100 × 100 μm^2 area of the corroded copper samples was analyzed for the chemical composition on the surface and depth profiling from the top down. The mass spectra generated are used to determine the composition of sample surface constituents.

4.2.5 Data Analysis

Calculation of the RMS roughness (R_{rms}) were accomplished using Gwyddion (version 2.10) open source software supported by the Czech Metrology Institute, which is freely available

on the internet.[212] The RMS roughness is calculated using the following equation:

$$R_{rms} = \sqrt{\frac{\sum_{i=1}^{n}(Z_i - \bar{Z})^2}{n}}$$

Where Z_i is the height of each data point, Z bar is the average of all height values in the image, and *n* is the number of data points within the image. Estimates of surface coverage were obtained with UTHSCA Image Tool for Windows version 3.00.[213] The percentage of colored pixels was determined subjectively to provide estimates of surface coverage. The topography images were converted to grayscale bitmaps and a threshold value was selected visually for conversion to black and white pixels.

4.3 Results and Discussion

4.3.1 Images of the Cleaned Copper Surface before Water Immersion

As a frame of reference, AFM topography views the surface of a freshly cleaned copper substrate are presented in Figure 4.1, providing a baseline for comparison to treated surfaces. Surface changes that occur at both the micro- and nanoscale can be characterized with AFM. Figure 1 exhibits successive zoom-in views ranging from 30 μm to 850 nm for scan sizes. Tall features are displayed as bright areas and shallower features are shown with dark colors. Several dark grooves or scratches which result from the manufacturing process are apparent in the AFM images, which are oriented in the vertical direction. The depth of the grooves ranged from 20 to 190 nm for the copper control surface viewed in Figure 4.1. For convenient comparison of various surface treatments, the AFM scan direction was consistently chosen to align the grooves vertically. Multiple areas of the samples were characterized, and the images presented display representative morphologies of the entire sample. A high resolution view (0.85×0.85 μm^2) of the

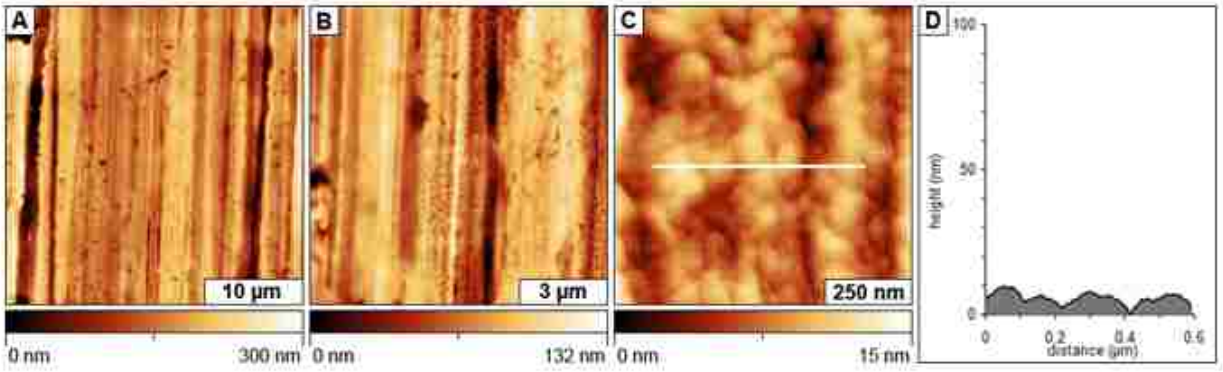

Figure 4.1. A clean copper surface viewed with contact mode AFM. Successively acquired images at different magnifications (A) 30×30 μm^2; (B) 10×10 μm^2; (C) 0.85×0.85 μm^2; (D) cursor profile for the line in C.

copper surface is presented in Figure 4.1C, for a relatively flat area of the sample with few scratches. The roughness for this selected area measured 2.4 nm, which is relatively smooth. A cursor line across the image (Figure 4.1D) displays a representative height profile in the range of 10-15 nanometers.

4.3.2 Surface Changes Observed at pH 9, Without or With Orthophosphate

The effects of corrosion for a copper substrate that was immersed in the conditions of sample 1 (pH 9) after 6 h or 24 h are viewed in Figure 4.2. Changes that have taken place after 6 h are shown in the top row of images (Figures 4.2A-2C); the bottom panels were acquired after 24 h immersion (Figures 4.2E-2G). Small clusters of adsorbates are observed, scattered throughout areas of the surface that were not evident for the control sample of Figure 4.1. The heights of the clusters range from 37 to 92 nm, and cover roughly 3% of the copper surface; lateral dimensions range from 160 to 460 nm. A cursor line profile (Figure 4.2D) indicates the height of the clusters in Figure 2C measures from 62 to 85 nm. The adsorbates result in an increase in overall surface roughness compared to the control sample. The roughness (R_{rms}) measures 28 nm for the area presented in Figure 4.2C.

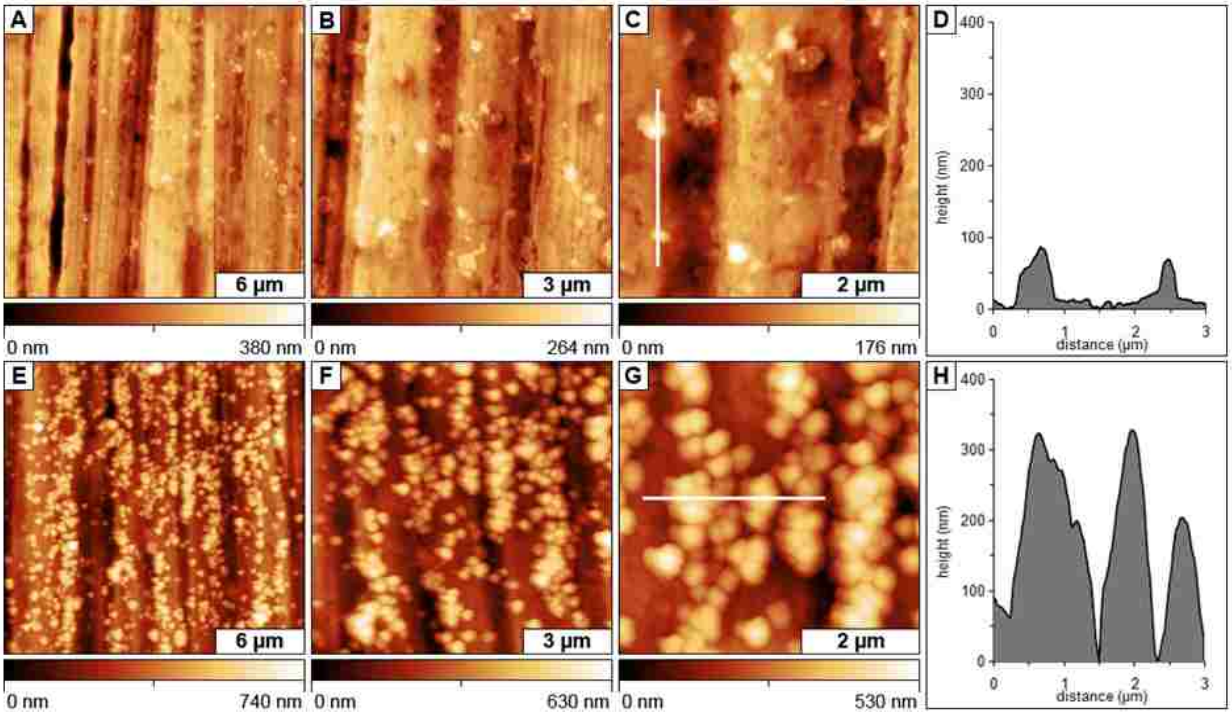

Figure 4.2. Copper surface after immersion in water sample 1 at pH 9. Zoom-in AFM views after 6 h for (A) 20×20 μm^2; (B) 10×10 μm^2; (C) 5×5 μm^2; (D) line profile for C. Changes after 24 h immersion for areas of (E) 20×20 μm^2; (F) 10×10 μm^2; (G) 5×5 μm^2; (H) line profile for G.

The surface changes became more prominent after 24 h of immersion in water sample 1. Larger clusters with greater surface coverage are visible in Figures 4.2E-2G. The adsorbates range in height from 170 to 390 nm, and cover 42% of the surface. A cursor line across several of the clusters show heights of 200-350 nm (Figure 4.2H) leading to an increase in RMS roughness of 95 nm.

The water conditions for Figure 4.3 are nearly the same as in Figure 4.2, except for adding orthophosphate. With addition of 6 mg/L orthophosphate at pH 9, distinct differences in surface morphology are produced as shown in Figure 4.3. After 6 h, the sample exhibits small adsorbed clusters that are randomly distributed across areas of the surface (Figures 4.3A-3C). The clusters range in height from 40 to 74 nm, and cover approximately 6% of the surface. The

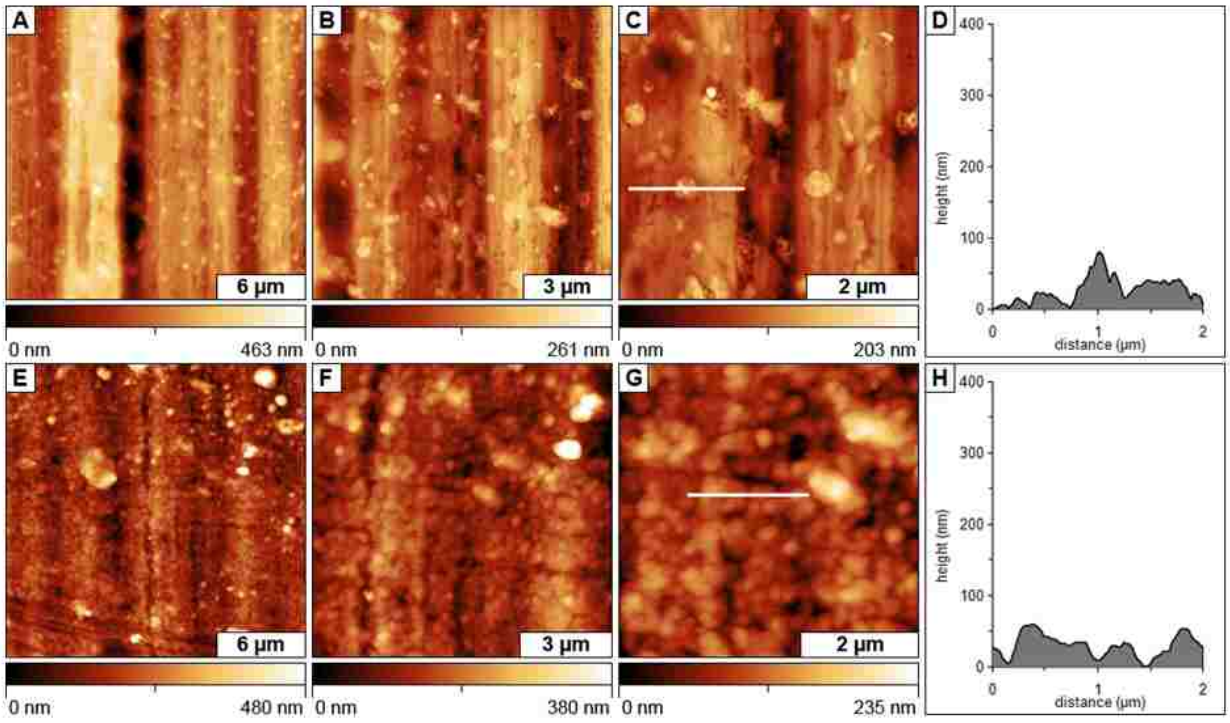

Figure 4.3. Copper surface after treatment with water sample 2 at pH 9 containing 6 mg/L orthophosphate. Contact-mode AFM topographs after 6 h of immersion: (A) 20×20 μm^2; (B) 10×10 μm^2; (C) 5.3×5.3 μm^2; (D) cursor profile for the line in C. Successive zoom views after 24 h of immersion: (E) 20×20 μm^2; (F) 9.7×9.7 μm^2; (G) 5×5 μm^2; (H) line profile for G.

RMS roughness measures 19 nm for the area of Figure 4.3C, which is comparable to the roughness of Figure 4.2C. The cross section in Figure 4.3D indicates that the adsorbates are shorter than those of Figure 4.2, measuring less than 100 nm in height.

After 24 h of immersion under conditions of pH 9 with 6 mg/L orthophosphate, the surface has been substantially changed. The entire surface of the copper substrate is covered by small adsorbates. The heights of the clusters measure approximately 50 nm or larger, however there are no uncovered areas of the substrate to reference as a baseline for cursor profiles. The surface roughness of Figure 4.3G measured 30 nm, however this value does not reflect changes relative to the bare copper. As compared to the surfaces of Figure 4.2 after 24 h, the deposits for

Figures 4.3E-H are smaller but are adsorbed throughout the surface to fully maximize the surface coverage.

4.3.3 Changes for Copper Surfaces Immersed in Water at pH 6.5

Copper surfaces were similarly immersed in water at pH 6.5 with different levels of orthophosphate for 6 and 24 h. The surface changes are presented in Figures 4.4A-C after 6 h of immersion in water sample 3 without addition of orthophosphate, and Figures 4.4E-G display the changes after 24 h. Angular crystalline adsorbates are distributed throughout areas of the surface after 6 h (Figures 4.4A-C). These crystals nearly cover the entire surface (80%) and measure 290 to 410 nm in height. With a close-up view in Figure 4.4C, the crystals are shown to have a

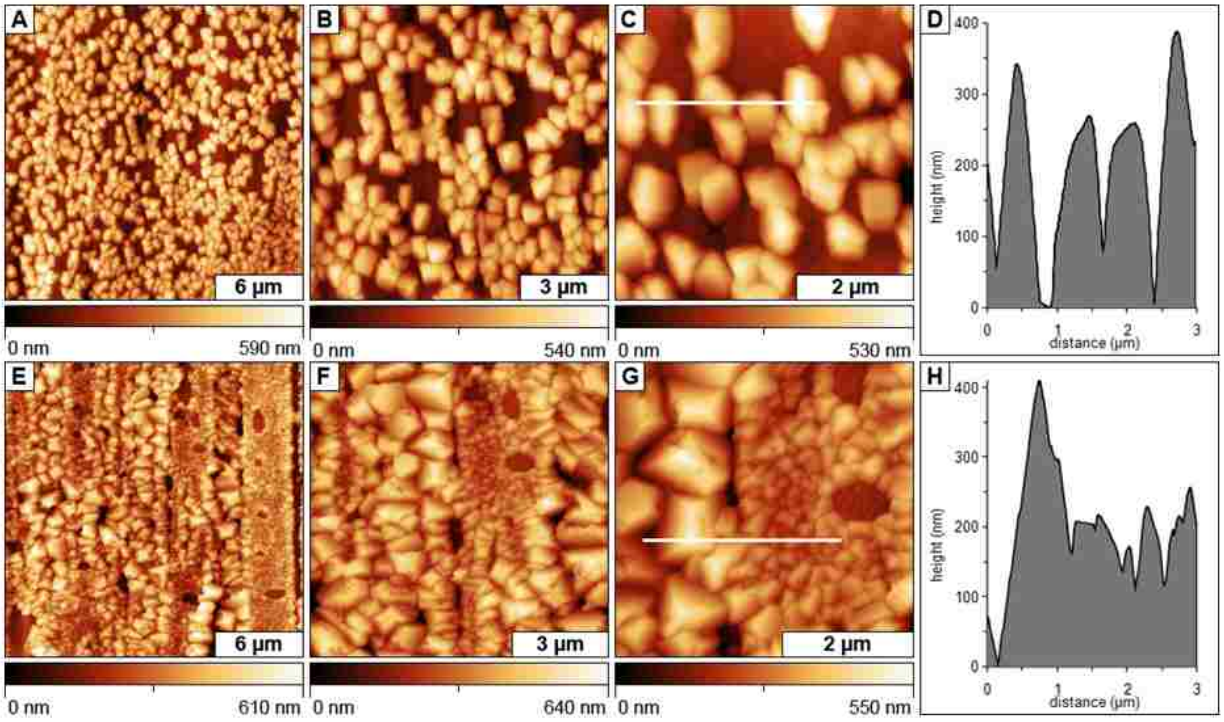

Figure 4.4. Surface changes after immersion in water sample 3 at pH 6.5. After 6 h: (A) 20×20 μm^2; (B) 10×10 μm^2; (C) 5×5 μm^2; (D) line profile for C. After 24 h of water exposure: (E) 20×20 μm^2; (F) 9.1×9.1 μm^2; (G) 4.5×4.5 μm^2; (H) line profile for G.

highly regular geometry with little variability in size at the nanoscale. There are approximately 33 crystals within the 5×5 μm^2 area of Figure 4.4C, and the RMS roughness measures 108 nm. The heights of the crystals range from 250 to 400 nm along the representative line profile of Figure 4.4D.

The copper surface exhibits near saturation coverage of a crystalline film after 24 h of immersion in water sample 3 (Figure 4.4E-G). Larger crystals have formed and there is a greater polydispersity for the crystal sizes. The surface density of adsorbates has increased; there are no longer gaps in between the angular particles. A few small holes are present within the layer of crystals, providing a baseline for measuring changes in the height of the crystalline layer. There are two oval shaped areas of bare copper in the upper right quadrant of Figure 4.4E which provide an in situ landmark for the zoom views of Figures 4.4F and 4.4G. Comparing the topography frames, the shape of the grooves of the underlying copper surface (oriented in the vertical direction) can be distinguished. Larger crystals appear to have formed within the grooves than on the flatter surface areas, likely attributable to confinement within narrow channels. The RMS roughness for the area defined in Figure 4.4G measures 74 nm.

To determine the composition of the crystalline features on the surface observed in Figure 4.4, x-ray diffraction (XRD) was performed on the copper substrates. The XRD spectrum obtained for the sample immersed for 6 h in water sample 3 is presented in Figure 4.5. Several large peaks which predominate the XRD spectrum result from the bulk composition of the Cu substrate. The smaller peaks observed for the spectrum arise from a minor surface contribution of Cu_2O, cuprite, to the overall diffraction pattern.

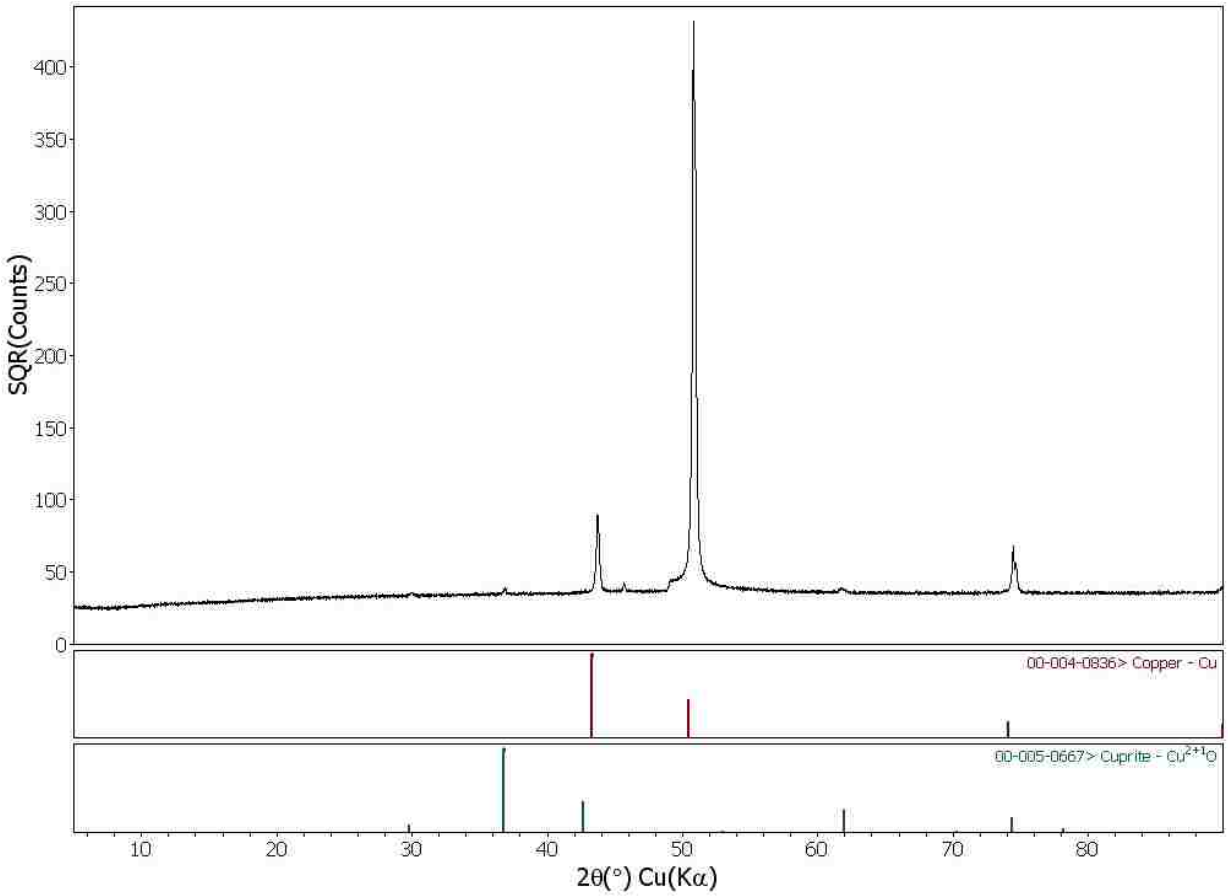

Figure 4.5. XRD spectrum of a copper surface after immersion in water sample 3 for 6 h.

The XRD spectrum obtained for the sample immersed in water sample 3 for 24 hours is shown in Figure 4.6. This spectrum is similar to the spectrum seen in Figure 4.5, however the peaks resulting from the presence of Cu_2O are greater in magnitude. This correlates well with the AFM results presented in Figure 4.4 which show that the surface was almost fully saturated with crystalline features after immersion in water sample 3 for 24 h. The density, coverage and thickness of the surface structures increased after longer immersion. This data indicates that crystals of cuprite have grown on the copper surface when immersed in water sample 3.

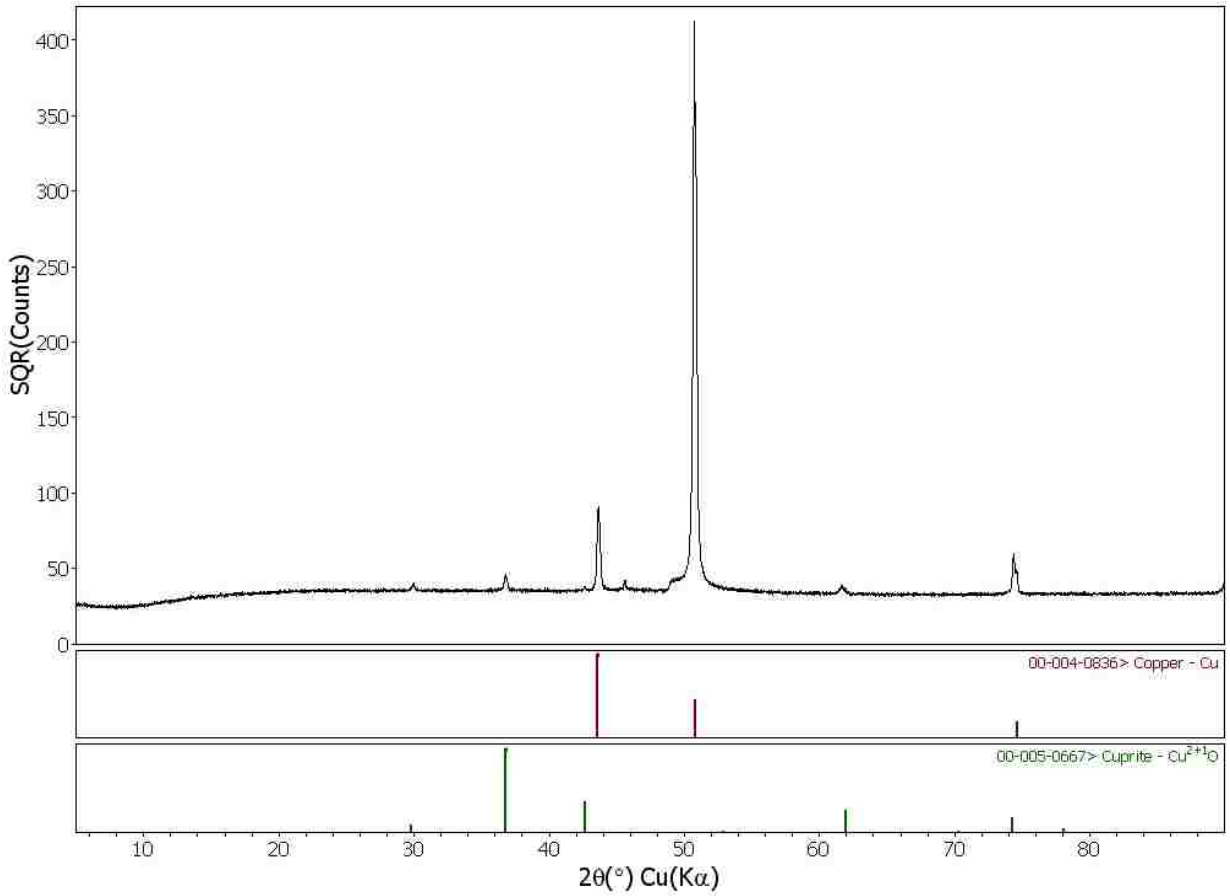

Figure 4.6. Diffraction spectrum of a copper surface immersed for 24 h in water sample 3.

The changes for a copper surface after immersion in water sample 4 at pH 6.5 containing 6 mg/L orthophosphate are shown in Figure 4.7. Comparing the AFM topographs of Figure 4.7 with the control sample of Figure 4.1, significant changes are evident throughout all areas of the surface. The morphology has changed from mixed domains of relatively smooth flat areas to exhibit a granular coating of small spherical structures. As the scan area is magnified in Figures 4.7B and 4.7C, the surface is covered with a dense network of chains of round clusters. The nanostructures measure from 35 to 62 nm in height and lateral dimension. The roughness measurement of Figure 4.7C indicates a relatively smooth surface, R_{rms} = 24 nm because the very

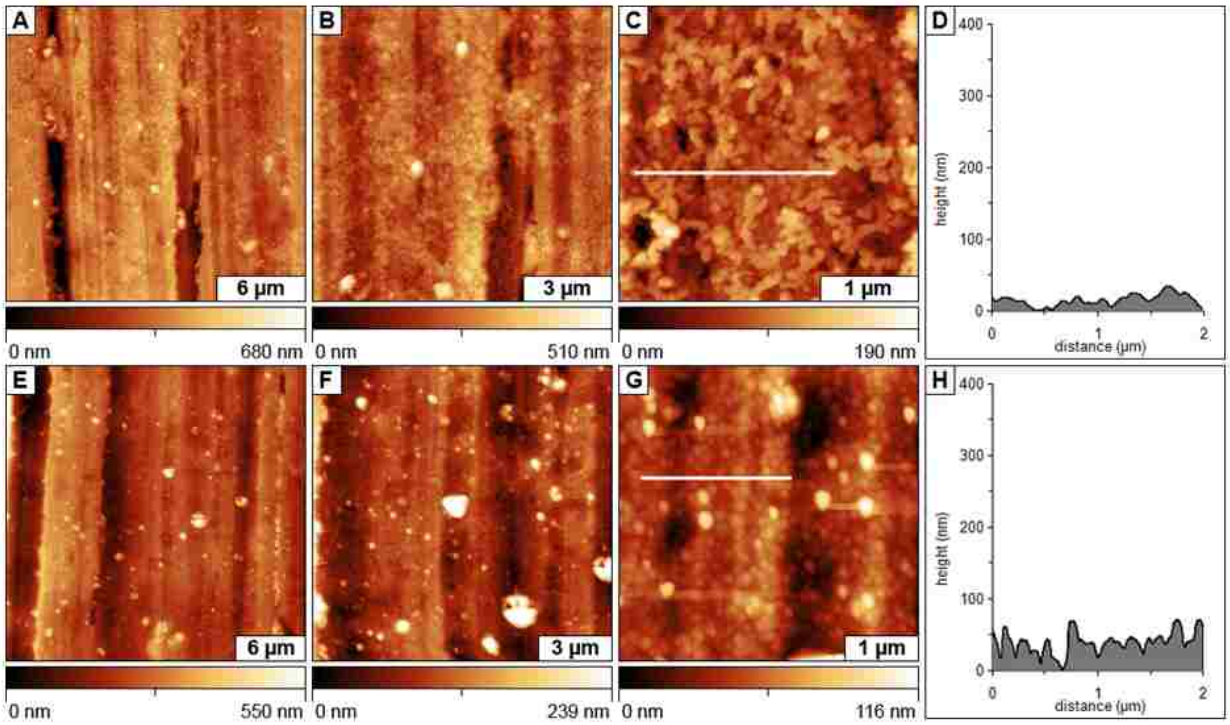

Figure 4.7. Copper surface after immersion in water sample 4 at pH 6.5 containing 6 mg/L orthophosphate. After 6 h of treatment: (A) 20×20 μm^2; (B) 10×10 μm^2; (C) 3×3 μm^2; (D) line profile for C. Topography images after 24 h of immersion: (E) 25×25 μm^2; (F) 12×12 μm^2; (G) 4×4 μm^2; (H) line profile for G.

small clusters are densely packed and expose few gaps or valleys. The cursor profile of Figure 4.7D correspondingly exhibits little surface corrugation.

Further surface changes become apparent after 24 h of immersion in water sample 4 (pH 6.5, 5 mg/L orthophosphate) as shown in Figures 4.7E-G. The smaller grooves and scratches have begun to fill in, and a few larger adsorbates are scattered across the surface. The size of the larger clusters ranges from 78 to 230 nm. The larger features maintain a round geometry, and higher magnification views of Figures 4.7F and 4.7G show that the larger structures are actually aggregates of several smaller clusters. The RMS roughness measures 16 nm for the area framed in Figure 4.7G, which is slightly smaller than that for Figure 4.7C. Differences in the roughness of the underlying substrate are quite variable at the nanoscale. When the changes in roughness

are quite small, the RMS parameter is not the best indicator for comparison. A representative line profile across Figure 4.7H demonstrates an increase for the heights of the surface structures, reaching 75 nm in dimension.

To evaluate the effects of the addition of the corrosion inhibitor orthophosphate, XRD was performed on the copper surfaces presented in Figure 4.7. The XRD spectrum of the sample immersed for 6 hours in water sample 4 is displayed in Figure 4.8. Unlike the diffraction pattern presented in Figure 4.5, there are no peaks apparent which correspond to the pattern for Cu_2O.

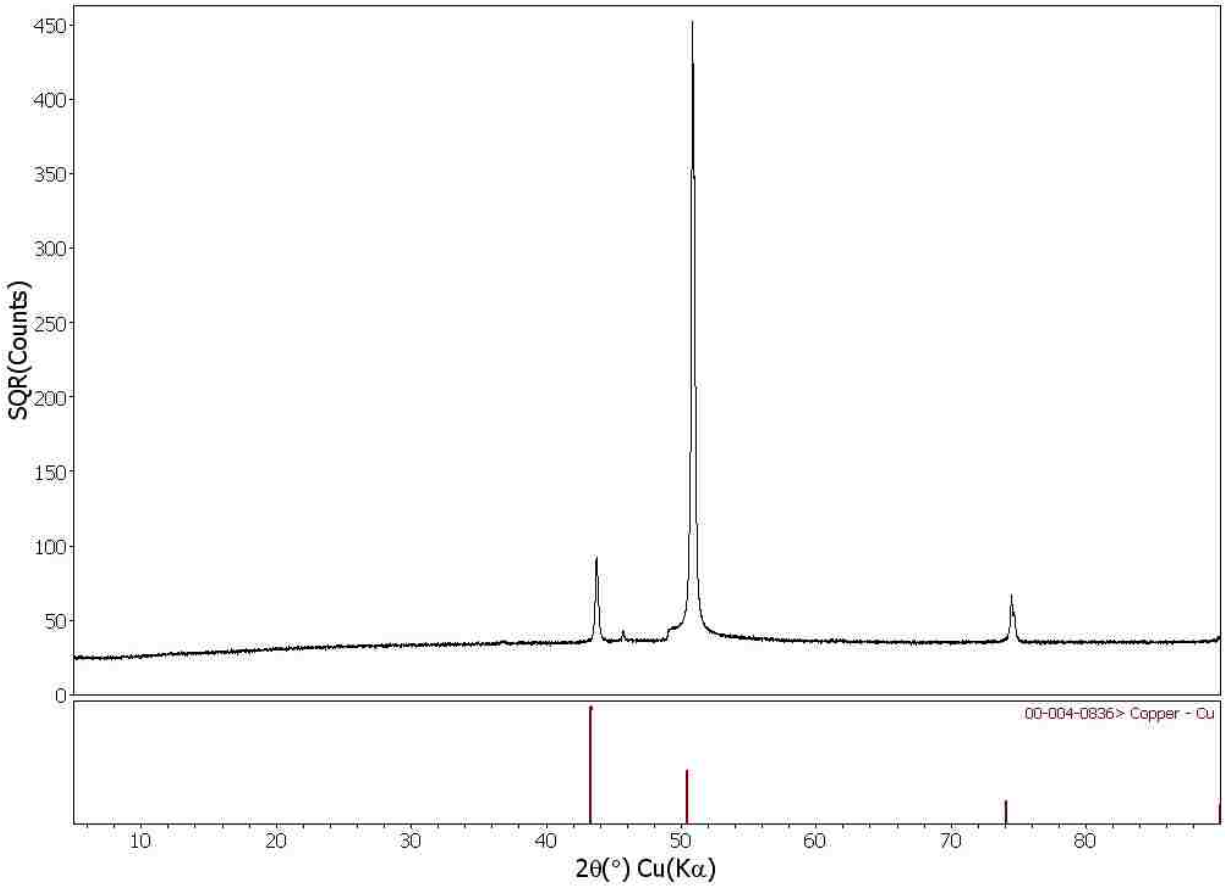

Figure 4.8. XRD spectrum for a copper sample immersed in water sample 4 for 6 h.

After 24 h of immersion in water sample 4, the XRD spectrum for the copper surface does not evidence further changes, as shown in Figure 4.9. Similar to the sample immersed for 6

h, there are no peaks in this spectrum which correspond to the diffraction pattern of Cu_2O. This shows that the addition of orthophosphate to a water having pH 6.5 inhibits the formation of cuprite on the surface of copper.

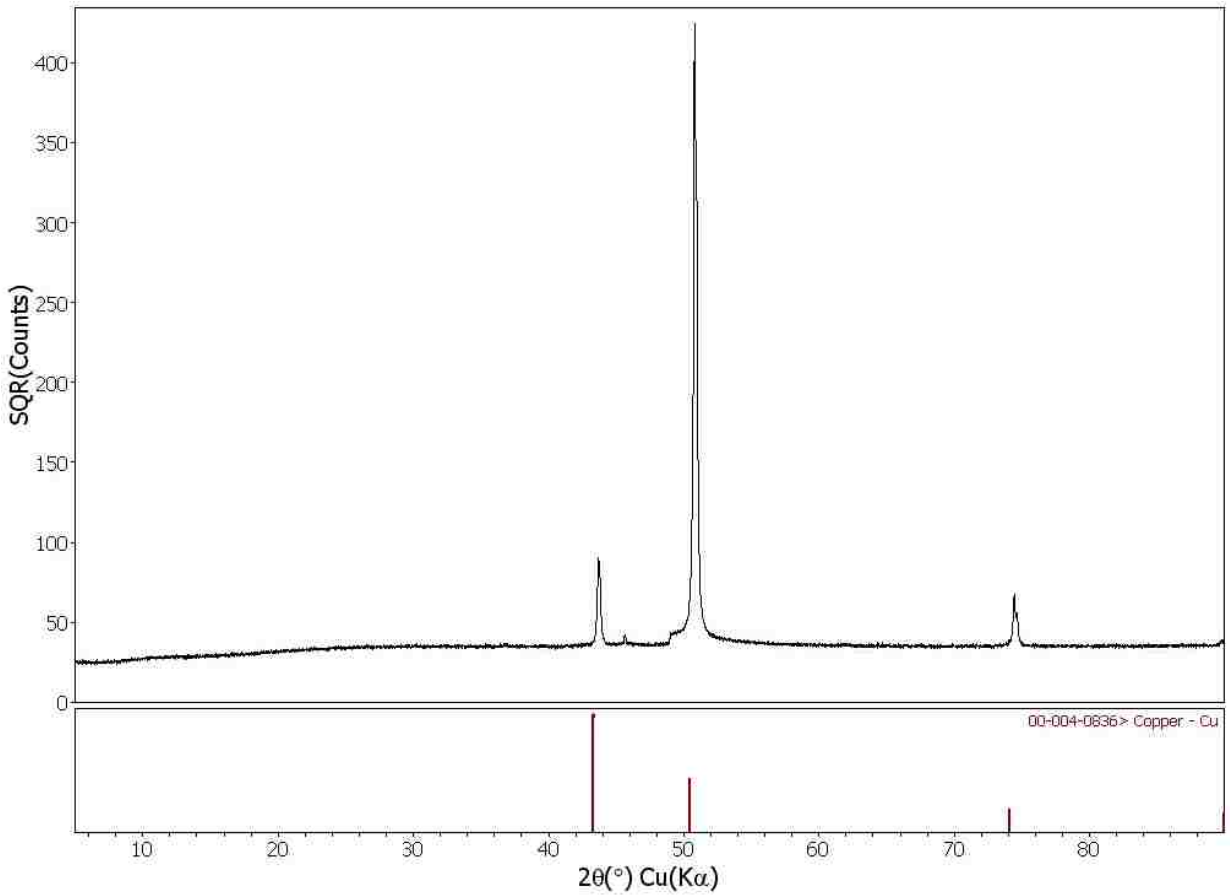

Figure 4.9. XRD spectrum of a copper surface immersed in water sample 4 for 24 h.

Changes in the morphology of copper surfaces caused by water corrosion can be readily observed using AFM, within a few hours of exposure to the water solutions. For the four water samples tested, morphology differences are readily apparent at the nanoscale. The shapes, sizes and distribution of adsorbates across the surface are influenced by the parameters of pH and orthophosphate concentration. Even small changes in pH substantially affect the resulting surface morphology. For example, crystalline surface structures were detected in the absence of

orthophosphates at pH 6.5, whereas at alkaline pH 9 the shape of the clusters was more spherical and smaller in dimension.

Comparing the samples of water containing orthophosphate, (water samples 2 and 4) the sizes of the clusters formed throughout areas of the surface were smaller and more homogeneous, as revealed in the topographs of Figures 4.3 and 4.7. Differences could be detected within the first 6 h of water immersion for Figure 4.3A-C versus Figures 4.7A-C, there was considerably less surface coverage of round clusters at pH 9. However, after 24 h of water treatment with orthophosphate, at either pH 6.5 or 9 the surfaces are strikingly similar with saturation coverage of adsorbates of uniform dimension.

Through XRD analysis, the chemical composition of the crystalline features formed on the copper surface immersed in water sample 3, water with pH of 6.5 and containing no orthophosphate, was determined to be Cu_2O. The formation of Cu_2O was inhibited by the addition of orthophosphate as indicated by the XRD spectra for a copper surface immersed in water sample 4, water with pH 6.5 containing 6 mg/L orthophosphate, displayed in Figures 4.8 and 4.9.

Further analysis of the chemical composition of the corrosion by-products that formed on the surface of the copper samples was accomplished using time-of-flight secondary ion mass spectrometry (ToF-SIMS). This supplemental data is reported in Appendix C.

CHAPTER 5. IMPACT OF pH, DISSOLVED INORGANIC CARBON, AND POLYPHOSPHATE FOR THE INTIAL STAGES OF WATER CORROSION OF COPPER SURFACES INVESTIGATED BY AFM

5.1 Introduction

The degradation of metal pipelines in water distribution systems caused by corrosion is an important research focus towards controlling corrosion and for reducing the release of deleterious metals into drinking water. The mechanisms of aqueous copper corrosion as influenced by various combinations of anions such as chloride, sulfate, bicarbonate, silicate, phosphate and calcium have not been thoroughly investigated at the nanometer scale. Studies of the early stages of water corrosion (< 24 h) occurring for a copper surface, as specifically influenced by changing pH, ions and orthophosphate levels will provide insight towards developing water treatment chemistries which minimize the corrosive effects of water on metal distribution systems.

Copper originates naturally in rock, soil, water, sediment, and air, and is often used for water pipes in household plumbing. Corrosion of metal plumbing in water distribution pipelines, valves, and fixtures leads to the release of copper ions into water samples and produces deposits of corrosion by-products on the interior walls of metal pipes. Corrosion can be detrimental to the quality of public drinking water, by releasing metals such as copper into water.[48] Though a small amount of copper is required by the human body as an essential nutrient, long-term exposure to elevated levels of copper in drinking water may cause serious health problems. Acute ingestion of high levels of copper have been shown to cause gastrointestinal disturbance, such as nausea and vomiting. Using water with elevated levels of copper over many years may cause damage to the liver or kidneys. In 1991, the USEPA published the Lead and Copper Rule in the National Primary Drinking Water Regulations (also referred to as the LCR or 1991 Rule). The Lead and Copper Rule requires that lead and copper levels in drinking water be minimized

in public water utilities. An action level of 1.3 mg/L was established for copper for water samples standing for more than six hours.

Phosphorous compounds often are used to inhibit corrosion and to protect metal surfaces.[193-197] Orthophosphate and hexametaphosphate have been shown to reduce the soluble copper release from corrosion products.[198] Aminophosphonic acid has been shown to inhibit corrosion of iron surfaces.[214]

Atomic force microscopy (AFM) provides 3D topographic information for a wide range of surface materials with micron to nanometer resolution. Increasingly, AFM is being applied for corrosion studies to gain insight on local changes of metal surfaces. High resolution AFM provides highly sensitive measurements for systematically investigating changes, enabling one to control a wide range of experimental parameters for surface treatments. For example, for *in situ* studies of corrosion inhibitors were investigated for different media using AFM.[202, 215-218] Surface studies with AFM have been used to investigate corrosion of materials such as copper[205-208, 219] steel,[200, 201] iron[199, 220] and silver.[203]

In this report, the effects of pH and polyphosphate levels combined with high levels of dissolved inorganic carbon were examined using AFM, secondary ion mass spectrometry (SIMS) and X-ray diffraction (XRD) analyses to gain insight on mechanisms of corrosion for copper surfaces. Differences in the structure and morphology were readily observed within 6 to 24 hours of exposure to various water samples, forming by-products and mineral deposits on copper surfaces. Substantial differences in surface morphology at different pH levels were also observed at the nanoscale, for water samples within the normal pH range of tap water samples.

5.2 Materials and Methods

5.2.1 Surface Preparation

Scanning probe studies require surfaces which are clean and relatively smooth for viewing small changes. The samples used in these experiments were pure copper (99.9%) cut into 1×1 in^2 squares. To remove possible impurities or surface contaminants, copper samples were cleaned by sonication for 5 minutes in 0.5% Triton X-100® in water (Curtis Matheson Scientific, Inc., Houston, TX). This was followed by ultrasonic cleaning in deionized water (Milli-Q, 18 megaohm) for 5 minutes. After sonication, the copper surfaces were rinsed in acetone and dried in air.

5.2.2 Water Sample Preparation

The water conditions for these experiments are summarized in Table 5.1. The pH of the solutions was controlled with an automated titrator system using hydrochloric acid and sodium hydroxide (Fisher Scientific). Reagents added to the solutions were sodium bicarbonate, sodium sulfate, sodium chloride, sodium hypochlorite (Fisher Scientific), and sodium hexametaphosphate (Mallinckrodt Chemicals). Initial concentrations were measured using inductively coupled plasma atomic emission spectrophotometry.

Table 5.1. Water conditions for copper sample immersion.

Sample	pH	DIC (mg/L)	Sulfate (mg/L)	Chloride (mg/L)	Chlorine (mg/L)	Hexametaphosphate (mg/L)
1	9	100	120	60	3	0
2	6.5	100	120	60	3	0
3	9	10	120	60	3	6
4	6.5	10	120	60	3	6

5.2.3 Experimental Setup

Copper samples were immersed in 1 L of water sample by suspension with a nylon string. The solutions were stirred at a slow rate with a magnetic stir bar and covered with parafilm.

After either 6 or 24 h of immersion, the samples were removed and dried in air for analysis using AFM.

5.2.4 Atomic Force Microscopy

An Agilent 5500 scanning probe microscope equipped with Picoscan v5.4 software (Agilent Technologies, Tempe, AZ) was used to aquire images in Figures 5.3 and 5.4. A Veeco Bioscope system (Veeco Instruments Inc., Plainview, NY) was used to aquire the images presented in Figures 5.1 and 5.2. Digital images were processed using Gwyddion (version 2.13) open source software, which is freely available on the Internet and supported by the Czech Metrology Institute.[187] Images were acquired in ambient conditions using acoustic AC (tapping) mode. Tapping mode tips were obtained from Nanosensors (Neuchatel, Switzerland), and had average resonance frequencies ranging from 155 – 170 kHz.

5.3 Results

Studies of the early stages of water corrosion, as specifically influenced by selected parameters of pH, alkalinity, anions and orthophosphate levels were accomplished by immersing cleaned pieces of copper in various water samples for either 6 or 24 h. After samples were removed and dried, AFM images were used to directly visualize the nucleation and growth of metal deposits, corrosion by-products or the formation of pits. Topographic views of samples that were prepared under controlled aqueous conditions provide insight for the role of pH and water parameters for the passivation or corrosion events which take place at the onset of copper corrosion.

5.3.1 Cleaned Copper Sample before Immersion in Water

To provide a control sample as a frame of reference for surface changes, AFM images were acquired for a cleaned copper sample before water immersion. Figure 5.1 displays the surface of a copper sample after it was cleaned. Vertical grooves or scratches aligned in a

vertical direction are shown in the successive zoom-in views of Figures 5.1A to 5.1C, which measure different depths ranging from 52 to 256 nm. The grooves are spaced at variable intervals, spanning distances from 1 to several microns. There are also small pits and scars scattered randomly throughout the sample surface, which contribute to a moderately rough surface. All of the AFM images acquired for subsequent samples in this report were oriented to view a similar vertical direction, to enable convenient comparison. Multiple areas of the samples were analyzed, and the views shown in Figure 5.1 are representative of the morphology for areas throughout the entire copper surface. The RMS roughness for a relatively smooth region of Figure 5.1C measures 2.4 nm. This value is comparable to previous reports of surface roughness for copper surfaces.[209]

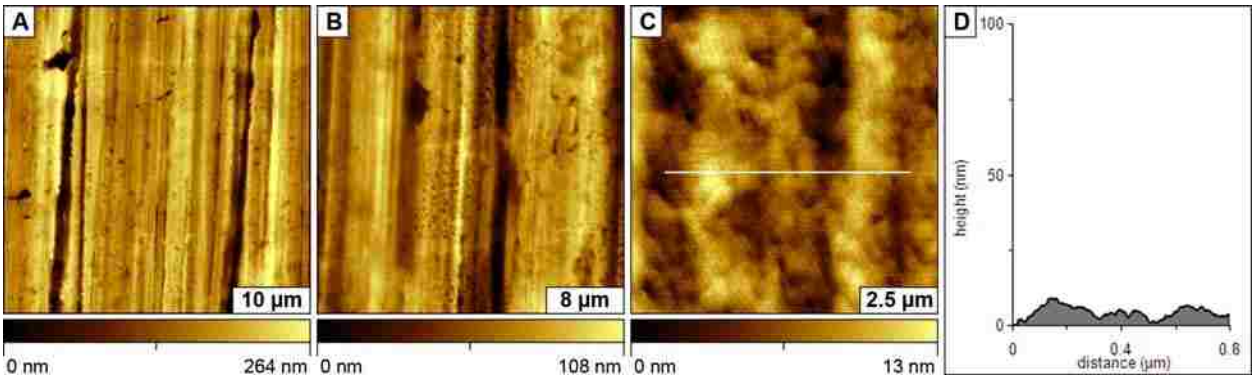

Figure 5.1. Surface views of a clean copper sample displaying different magnifications. Tapping mode topographs for areas of (A) 40×40 µm^2; (B) 8×8 µm^2; (C) 1×1 µm^2; (D) cursor profile for the line in C.

5.3.2 Effects of High Carbonate Alkalinity at pH 6.5 versus 9

Dissolved inorganic carbon (DIC) is the sum of inorganic carbon species and includes contributions of carbon dioxide, carbonic acid, bicarbonate and carbonate anions. Most of the total alkalinity of natural waters results from the carbonate alkalinity of DIC. In previous reports, alkalinity has been shown to mitigate the corrosive effects of water and protect copper

surfaces.(Lytle et al.) For a direct assessment of the effects of high alkalinity on copper surfaces, water sample 1 was prepared at pH 9 with a relatively high DIC level of 100 mg/L. Successive zoom-in views of the copper surface after 6 and 24 h at high alkalinity are presented in Figure 5.2, in which the DIC originated from dissolved sodium bicarbonate. The top row (Figures 5.2A-C) shows the surface changes after immersion for 6 h, and the bottom row (Figures 5.2D-F) shows the topography after 24 h. The images disclose scattered arrangements of round protrusions or clusters of carbonate by-products, formed at the surface-liquid interface. There was no evidence of pits or holes being formed within this time frame, and successive magnified views of Figures 5.2B and 5.2C reveal that the entire surface is covered with regular sized

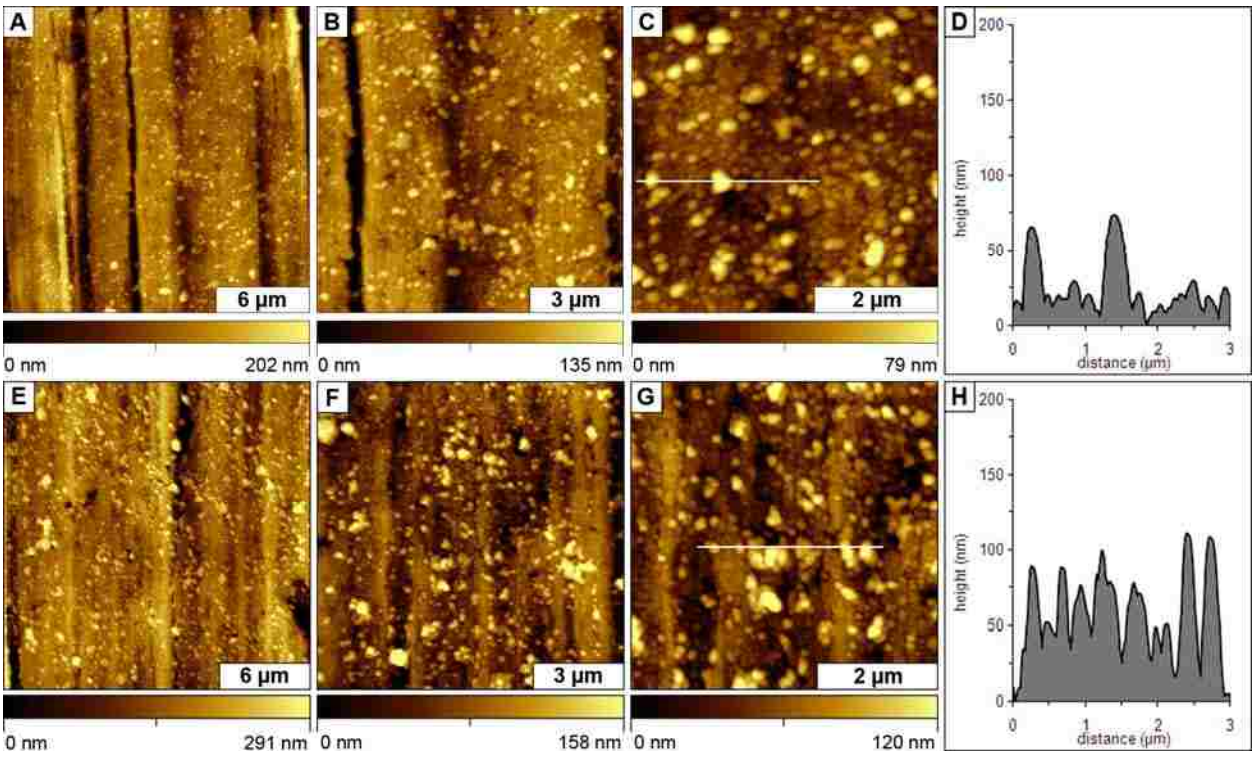

Figure 5.2. Copper surface after immersion in water sample 1 at pH 9 with 100 mg/L DIC. Zoom in magnified views after 6 h for (A) 20×20 µm^2; (B) 10×10 µm^2; (C) 5×5 µm^2; (D) line profile for C. Changes after 24 h for areas of (E) 20×20 µm^2; (F) 10×10 µm^2; (G) 5×5 µm^2; (H) line profile for G.

clusters ranging from 25 to 63 nm. A representative line profile in Figure 5.2D indicates the heights for two large adsorbates measure 48 and 55 nm. The overall roughness of the sample has increased; the area in Figure 5.2C evidenced an RMS roughness measuring 13 nm.

After 24 h of immersion in water sample 1, the surfaces display similar morphologies for carbonate clusters, however at higher density. A few larger clusters have attached to the surface, exhibiting heights ranging from 48 to 135 nm. The taller adsorbates are actually aggregates of smaller clusters, as revealed in the zoom-in AFM views of Figures 5.2F and 5.2G. A representative cursor profile across Figure 5.2G shows that the heights of the surface protrusions have increased in size, in comparison to Figure 5.2C.

Water sample 2 was prepared at pH 6.5 to match the composition of sample 1, for a direct comparison of pH effects for copper surfaces exposed to high DIC levels. There are considerable differences in surface morphology after immersion in water sample 2, as shown in the AFM topographs of Figure 5.3. The upper row (Figures 5.3A-C) displays images for a sample that was immersed in water sample 2 for 6 h, and the second row (Figures 5.3E-G) shows the changes after 24 h immersion. Large, angular crystalline nanostructures are evident for the sample prepared at pH 6.5. The large crystals shown in the upper row of images have heights ranging from 432 to 723 nm, and cover approximately 20% of the surface. The RMS roughness has increased to 164 nm. The facets and angular morphology of the crystals can be readily recognized as salt crystals resulting from the precipitation of sodium salts at lower pH.

After 24 h immersion in water sample 2, the surface coverage and density of crystals has increased in comparison to the 6 h sample. The heights of the structures range from 210 to 580 nm and the surface coverage has increased to approximately 56% of the total area. The RMS roughness of the 24 h sample measured 166 nm.

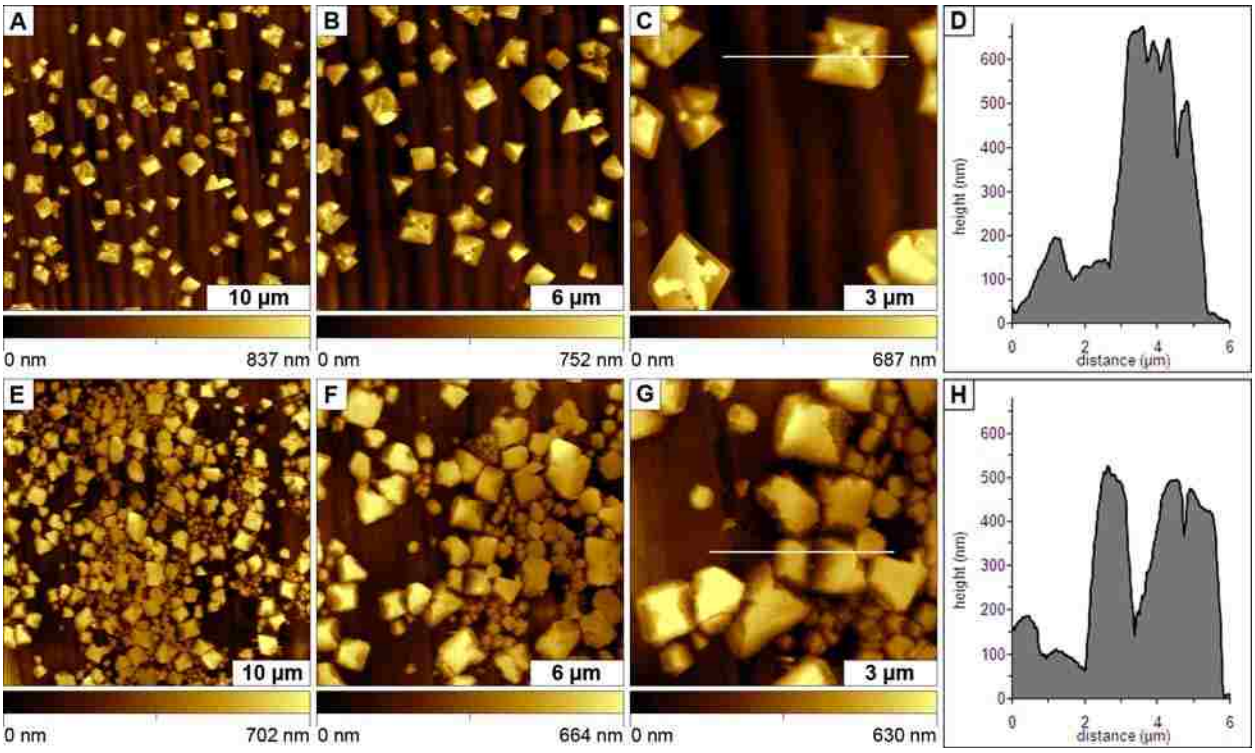

Figure 5.3. Surface changes of copper substrate after immersion in water sample 2 with pH 6.5 and 100 mg/L DIC. AFM topographs after immersion for 6 h for areas of (A) 30×30 μm^2; (B) 20×20 μm^2; (C) 10×10 μm^2; (D) line profile for C. After 24 h for areas of (E) 40×40 μm^2; (F) 20×20 μm^2; (G) 10×10 μm^2; (H) line profile for G.

5.3.3 Surface Changes with Addition of Hexametaphosphate at pH 6.5 and 9

When hexametaphosphate was added in the water solutions, at a lower alkalinity level of 10 mg/L DIC, considerably different morphologies were observed for the copper surfaces. Figure 5.4 displays images of the surface changes for a copper surface immersed in water sample 3 (pH 9, 6 mg/L hexametaphosphate, 10 mg/L DIC). The top row (Figures 5.4A-B) shows a sample that was immersed in water sample 3 for 6 h, and the bottom row of images (Figures 5.4D-E) shows views of a sample immersed for 24 h. After 6 h of sample immersion, round plateau-like features become apparent in Figure 5.4A, however these structures appear to be protrusions that are integrated within the surface and are derived from the copper landscape. The dimensions of the round plateaus range to as large as 0.72 to 1.25 µm in size. The protrusion

nanostructures do not appear to be attached to the surface, rather, a predominant high surface coverage of pits and valleys have become evident in the zoom-in views of Figure 5.4B. The pits seen in this image have depths of 18 to 50 nm. The surface morphologies reveal the onset of changes attributable to corrosion. The RMS roughness for the topograph of Figure 5.4B measures 11 nm.

After 24 h immersion in water sample 3, the pitting became more predominant and

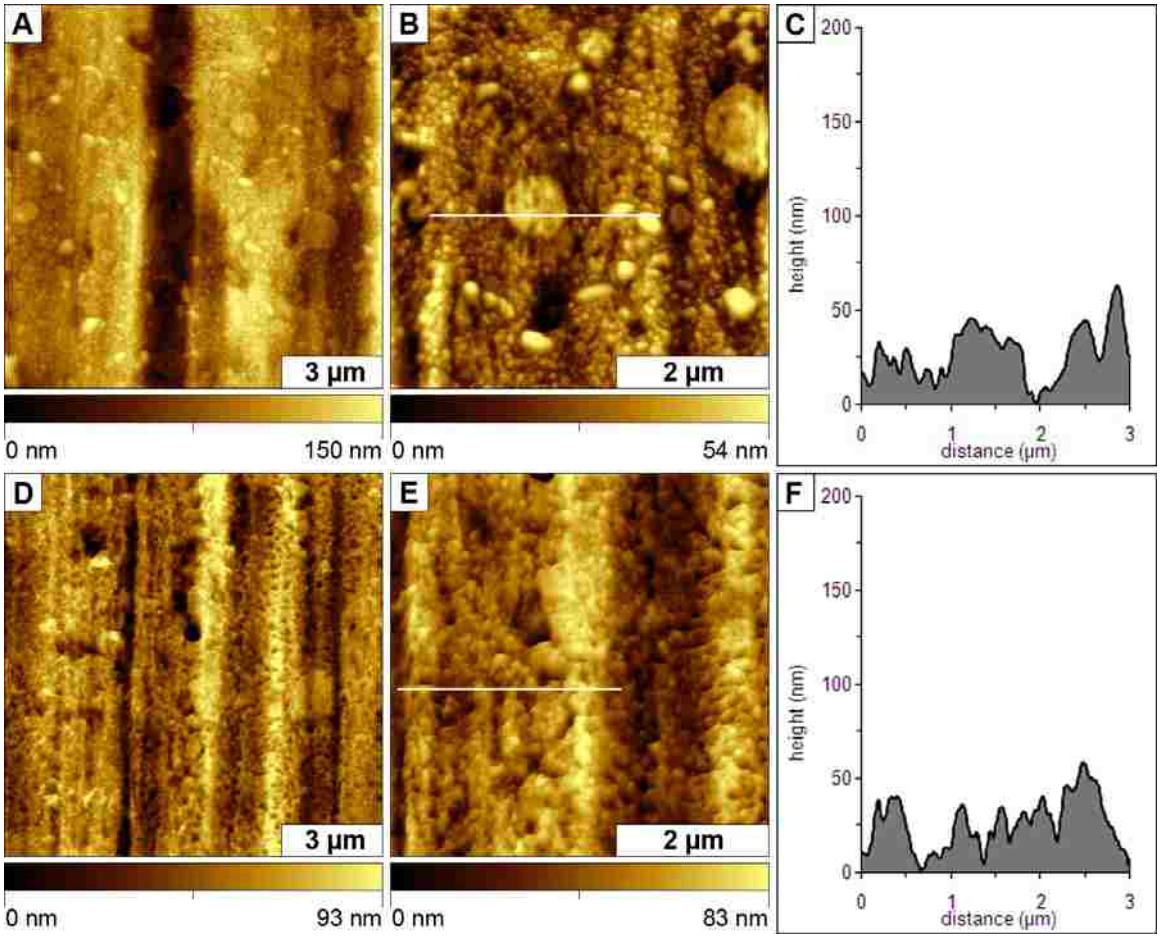

Figure 5.4. Changes due to corrosion for a copper surface after immersion in water sample 3 at pH 9 with 6 mg/L polyphosphate and 10 mg/L DIC. Surface views after 6 h for areas of (A) 11.4×11.4 μm^2; (B) 5×5 μm^2; (C) line profile for B. After 24 h of immersion: (D) 11.4×11.4 μm^2; (E) 5×5 μm^2; (F) line profile for E.

clearly apparent throughout areas of the surface. Instead of the relatively smooth, continuously flat surface of Figure 5.1 (RMS roughness measured 2.4 nm), the surface areas show a high density of multiple pits and valleys have formed. There is no evidence of loosely attached adsorbates or deposits formed for these water conditions, rather the surface shows new shapes of valleys and protrusions throughout the sample areas. The evidence of pitting is especially visible in Figure 5.4D when put side-by-side with to a comparable area of the control sample of Figure 5.1B. The line profile of Figure 5.4F indicates the surface corrugation ranges from 15 to 60 nm. The roughness after 24 h increased to 15 nm for the surface immersed in water sample 3.

The effects of hexametaphosphate for treating a copper surface at pH 6.5 (6 mg/L hexametaphosphate, 10 mg/L DIC) are shown in the AFM images of Figure 5.5. The upper images (Figures 5.5A and 5.5B) display changes for a sample immersed in water sample 4 for 6 h and the bottom row (Figures 5.5D and 5.5E) presents views for a sample immersed under the same conditions for 24 h. After 6 h immersion, the surface displays both the formation of surface deposits as well as an increase in pitting corrosion. Round adsorbates of various sizes and shapes have formed throughout areas the copper surface. The adsorbates are smooth and round, with a globular shape. Pitting is also evident for the zoom-in view of Figure 5.5B, evidencing a continuous coverage of the surface with small pits that are 20 to 40 nm deep. The globular nanostructures measure 25 to 61 nm in dimension, and the RMS roughness measured 14 nm for the area framed in Figure 5.5B.

A new surface morphology evolved after immersion in water sample 4 for 24 h. The smooth globular shapes have been replaced with compact clusters of aggregated nanoparticles, as well as an increase in depth and density for pinhole pits (Figure 5.5D). The surface changes result from the interplay of corrosive etching and the adsorption of nanoparticle deposits. From

the zoom-in view presented in Figure 5.5E, there are many aggregated clusters of small adsorbates attached at the sites of grooves and crevices on the surface. The clusters of nanoparticles measure from 15 to 71 nm in height, and the RMS roughness increased to 22 nm (Figure 5.5E).

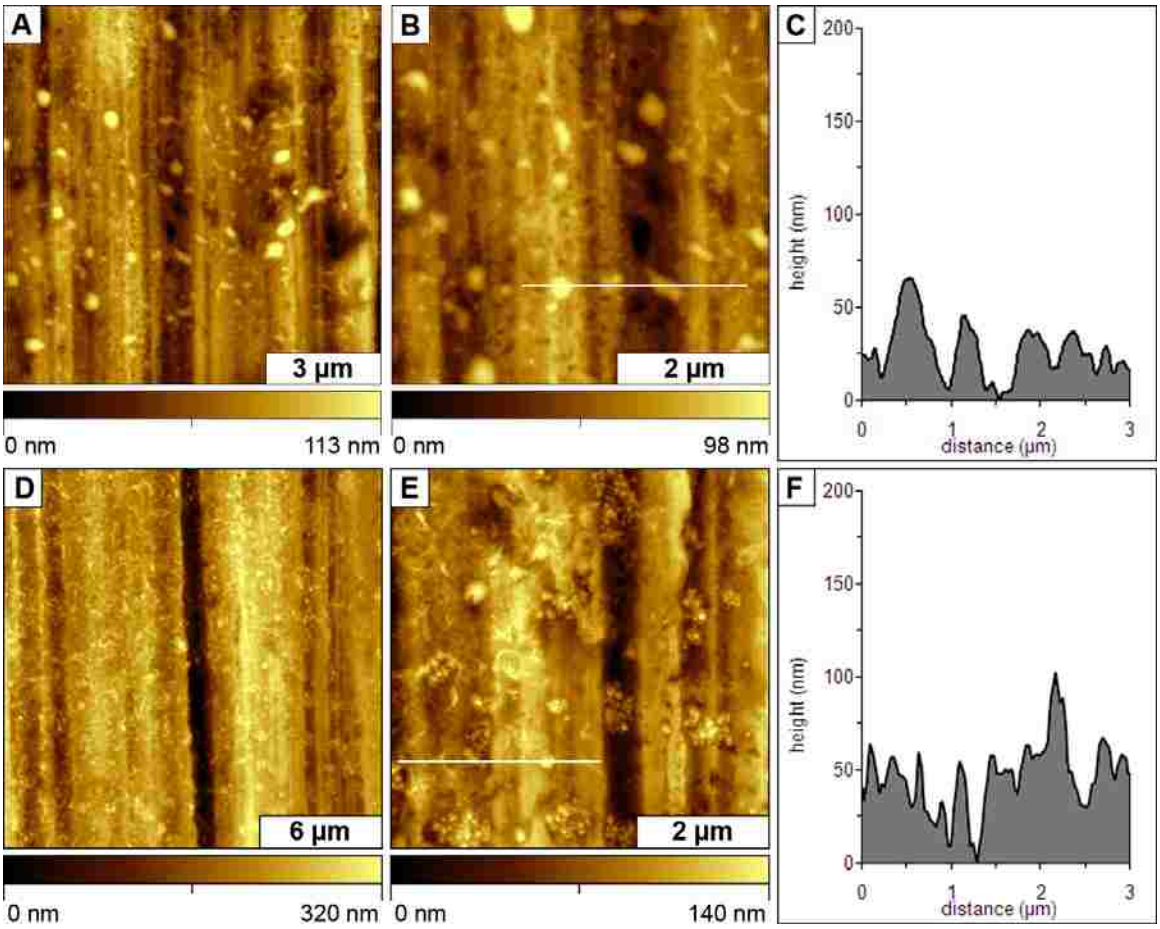

Figure 5.5. Changes for a copper surface after immersion in water sample 4 at pH 6.5 with 6 mg/L polyphosphate and 10 mg/L DIC. Surface changes after 6 h for (A) 10×10 μm^2; (B) 5×5 μm^2; (C) line profile for B. After 24 h of exposure for areas of (D) 18.3×18.3 μm^2; (E) 5.6×5.6 μm^2; (F) line profile for E.

5.4 Discussion

Side-by-side comparisons of the AFM images of various surface treatments at different immersion intervals provide new insight on the role of polyphosphates, DIC and pH in surface

passivation or corrosion. As a frame of reference, the untreated surface of Figure 1 can be compared to each of the sets of AFM images, providing a baseline of the expected surface morphology for untreated copper. Evidence of an increase in pitting was not observed for surfaces treated with water samples 1 (pH 9) and 2 (pH 6.5), with the addition of 100 mg/L DIC, thus increased alkalinity from bicarbonate was demonstrated to inhibit corrosion of copper in agreement with previous reports. The AFM images in Figures 5.2 and 5.3 display the surface deposits of different chemical nature, however there was no clear evidence of an increase in the density of surface pits due to corrosion. The facets and angular morphology of the crystals viewed in Figure 5.3 can be attributed to the precipitation of salt crystals.

Changes due to corrosion were observed for the surfaces of copper which occurred at lower levels of DIC, even with the addition of hexametaphosphate, as disclosed in the AFM images of Figures 5.4 and 5.5. Changes attributable to corrosive pitting were more readily apparent and advanced at pH 9 than was observed for surfaces treated at pH 6.5. An interchange between particulate deposition and corrosive pitting was evident for surfaces treated with water sample 4 at pH 6.5. Understanding the chemical composition of the surface adsorbates through XRD or SIMS characterizations will provide a clearer picture of the nature and mechanism of copper corrosion as well as the routes for producing passivating surface layers of mineral deposits.

5.5 Conclusion

When one considers the complex interactions at the surface-liquid interface of copper for various pH and water treatment conditions, a great deal of research remains to be addressed. Although we have judiciously chosen certain concentrations of DIC and polyphosphates for these initial investigations, rich information about the evolution of surface structures can be

gained by investigations with incremental changes in pH, solution concentration and immersion intervals. This report furnishes a practical framework and starting point for selecting experimental parameters which markedly influence the surface changes that occur during water corrosion. By combining approaches for qualitative and quantitative surface characterizations, a predictive molecular-level model can be developed for understanding the interplay between anions, salts, organic agents, DIC and pH for processes of surface corrosion and passivation.

CHAPTER 6. SYNOPSIS AND FUTURE PROSPECTUS

There is an emerging requirement for robust, inexpensive lithography methods for the high throughput fabrication of nanostructures. In Chapter 3, "two-particle" lithography was demonstrated as a facile route for producing well-ordered arrays of rings of nanoparticles. The new method requires only simple bench chemistry techniques of mixing, centrifuging, evaporation, and rinsing. Two-particle lithography was first demonstrated using cysteine-coated CdS quantum dots to produce regular arrays of ring-shaped nanostructures spanning micron-sized areas. Since this development, the approach for two-particle lithography has been generically applied for preparing nanopatterns of several other systems of nanoparticles. Investigations are in progress which apply the capabilities of two-particle lithography to generate well-defined test platforms of nanomaterials such as metal nanoparticles which were synthesized by templating with plasmid DNA,[221-223] magnetite nanoparticles with various organic shells,[224] cobalt nanoparticles with surface coating terminated with oleic acid and trioctylphosphine oxide,[225] ferritin proteins which have a protein cage encapsulating an iron nanoparticle core[226] as well as nanoparticles derived from ionic liquids.[227] The dimensions of nanostructures produced via two-particle lithography are tunable by selecting different sizes of templating spheres of either latex or silica. The arrays of nanostructures produced by two-particle lithography provide precise, reproducible dimensions for nanoscale investigations of surface properties, furnishing well-defined test platforms that are suitable for successive characterizations with scanning probe microscopy.

Understanding the dependence of magnetic properties and the size scaling effects at the nanoscale is important for both understanding the behavior of existing nanomomaterials as well as for the advancement in the development of new materials. A newly developed atomic force microscopy imaging mode referred to as magnetic sample modulation (MSM) was developed for

mapping and measuring the vibrational response of magnetic nanomaterials on surfaces when the flux of an alternation electromagnetic field is applied to samples. The new atomic force microscopy (AFM) imaging mode was first demonstrated for micropatterned stripes of iron oxide nanoparticles, as described in Chapter 2 in Figure 2.10. An alternating flux of an AC-generated electromagnetic field was used to induce vibration of magnetic nanomaterials on surfaces. The vibration is sensitively detected using channels of a lock-in amplifier. The MSM imaging technique provides practical and innovative strategy for mapping and measuring the magnetic forces of metal nanoparticles, and establishes a new benchmark in resolution and sensitivity for AFM characterizations of magnetic nanomaterials, at the level of detecting the magnetic response of individual nanoparticles. The MSM imaging mode furnishes unparalleled sensitivity and selectivity for distinguishing samples which exhibit a magnetic moment in the presence of an applied alternating current (AC) electromagnetic field. Changes in the phase and amplitude of vibrating nanomaterials are mapped relative to the driving AC signal. Magnetic sample modulation has been applied for characterizing individual ferritin,[226] DNA-templated nanoparticles of nickel and iron,[221, 222] and cobalt nanoparticles as small as 4 nm in diameter.[225]

Nanostructures of ferritin were used as a test platform for investigations with MSM to characterize biomolecules at the nanoscale. The ferritin nanocage is 12 nm in height and contains about 4500 iron atoms. The iron core which is about 6 nm in size is paramagnetic. Ferritin has an iron core which is paramagnetic. Particle lithography was used to define the surface assembly of ferritin to generate well defined rings of protein necklaces. Well organized structures of ferritin on the surface enable accurate and precise characterizations of the magnetic properties of the samples using MSM. The sensitivity and selectivity of MSM enabled mapping and selective detection of the iron atoms present within the encapsulating protein cage. The

combination of nanoscale lithography with new measurement approaches with AFM was brought about by protocols described and developed for this dissertation. Combining lithography and AFM characterizations is a practical strategy for analysis of surface properties at the nanoscale.

Magnetic samples need to be carefully arranged on surfaces to enable vibration. Designed test structures with nanoscale dimensions were prepared using practical, inexpensive strategies based on the chemical approaches of self-assembly by two-particle lithography. Magnetic nanoparticles of cobalt and nickel were fabricated using plasmid DNA as a structural template, in a collaborative project with A. Varotto and C. M. Drain at City University of New York. The method of magnetic sample modulation (Chapter 2) is a hybrid mode of AFM imaging. For MSM-AFM, a modulated AC electromagnetic field selectively induces vibration of magnetic nanomaterials on surfaces. A *non-magnetic* AFM tip is brought into contact with the sample surface using constant force feedback. The mechanical vibration of the magnetic nanomaterials on the surface is sensed by the AFM tip when it touches the vibrating domains. Only the magnetic domains vibrate, providing selective contrast when energy is transferred from the sample to the AFM probe. A lock-in amplifier is used to acquire the amplitude and phase components of the AC signal which provides exquisite sensitivity for small changes in AFM tip movement driven by the oscillation of magnetic samples. Essentially, MSM is a hybrid of contact mode AFM and selective "force modulation" of magnetic domains. Both the amplitude and phase signal are acquired simultaneously with topographic images to map the location of magnetic nanoparticles. Our results indicate that the best images for magnetic mapping are acquired with standard soft commercial probes using sample resonance frequencies which are different than the natural resonances of the AFM cantilevers.

Atomic force microscopy provides a tool for developing new approaches to view the changes of surface during the early stages of corrosion. The effects which ions have on the resulting copper surface after immersion in a particular water chemistry, as well as the effects of known corrosion inhibitors such as phosphates, has been performed. The size, shape and surface coverage of corrosion products can be directly visualized with AFM for side-by-side comparisons of surface treatments. Combining AFM with other analytical techniques such as x-ray diffraction (XRD) and secondary ion mass spectrometry (SIMS) gives new insight into the mechanisms for surface passivation and/or corrosion processes. New collaborative projects are in progress by S. L. Daniels of LSU, for investigating the role of water chemistry parameters for changes in surface chemistry at even earlier stages of corrosion, using in situ protocols with AFM. The United States Environmental Protection Agency (USEPA) will continue to sponsor research internships for students with AFM training in this on-going collaborative effort. As evidence of the priority for such investigations in research with the USEPA, a new research building is nearly constructed for targeting surface chemistry and developing new characterization tools for surface analysis.

REFERENCES

1. Butt, H. J.; Cappella, B.; Kappl, M., Force measurements with the atomic force microscope: Technique, interpretation and applications. *Surf. Sci. Rep.* **2005,** *59* (1-6), 1-152.

2. Hugel, T.; Seitz, M., The study of molecular interactions by AFM force spectroscopy. *Macromol. Rapid Commun.* **2001,** *22* (13), 989-1016.

3. Gimzewski, J. K.; Joachim, C., Nanoscale science of single molecules using local probes. *Science* **1999,** *283* (5408), 1683-1688.

4. Santos, N. C.; Castanho, M. A. R. B., An overview of the biophysical applications of atomic force microscopy. *Biophys. Chem.* **2004,** *107* (2), 133-149.

5. Muller, D. J.; Janovjak, H.; Lehto, T.; Kuerschner, L.; Anderson, K., Observing structure, function and assembly of single proteins by AFM. *Prog. Biophys. Mol. Biol.* **2002,** *79* (1-3), 1-43.

6. De Feyter, S.; De Schryver, F. C., Two-dimensional supramolecular self-assembly probed by scanning tunneling microscopy. *Chem. Soc. Rev.* **2003,** *32* (3), 139-150.

7. Gaboriaud, F.; Dufrene, Y. F., Atomic force microscopy of microbial cells: Application to nanomechanical properties, surface forces and molecular recognition forces. *Colloids Surf., B* **2007,** *54* (1), 10-19.

8. Palermo, V.; Liscio, A.; Palma, M.; Surin, M.; Lazzaroni, R.; Samori, P., Exploring nanoscale electrical and electronic properties of organic and polymeric functional materials by atomic force microscopy based approaches. *Chem. Commum.* **2007,** (32), 3326-3337.

9. Kramer, S.; Fuierer, R. R.; Gorman, C. B., Scanning probe lithography using self-assembled monolayers. *Chem. Rev.* **2003,** *103* (11), 4367-4418.

10. Wouters, D.; Schubert, U. S., Nanolithography and nanochemistry: Probe-related patterning techniques and chemical modification for nanometer-sized devices. *Angew. Chem. Int. Ed.* **2004,** *43* (19), 2480-2495.

11. Liu, M.; Amro, N. A.; Liu, G. Y., Nanografting for surface physical chemistry. *Annu. Rev. Phys. Chem.* **2008,** *59*, 367-386.

12. McCreery, R. L., Molecular electronic junctions. *Chem. Mater.* **2004,** *16* (23), 4477-4496.

13. Davis, J. J.; Morgan, D. A.; Wrathmell, C. L.; Axford, D. N.; Zhao, J.; Wang, N., Molecular bioelectronics. *J. Mater. Chem.* **2005,** *15* (22), 2160-2174.

14. Zotti, G.; Vercelli, B.; Berlin, A., Monolayers and multilayers of conjugated polymers as nanosized electronic components. *Acc. Chem. Res.* **2008,** *41* (9), 1098-1109.

15. Li, D.; Bonnell, D. A., Controlled patterning of ferroelectric domains: Fundamental concepts and applications. *Annu. Rev. Mater. Res.* **2008,** *38*, 351-368.

16. Xie, X. N.; Chung, H. J.; Sow, C. H.; Wee, A. T. S., Nanoscale materials patterning and engineering by atomic force microscopy nanolithography. *Mater. Sci. Eng., R* **2006,** *54* (1-2), 1-48.

17. Archakov, A. I.; Ivanov, Y. D., Analytical nanobiotechnology for medicine diagnostics. *Mol. Biosyst.* **2007,** *3* (5), 336-342.

18. Muller, D. J.; Dufrene, Y. F., Atomic force microscopy as a multifunctional molecular toolbox in nanobiotechnology. *Nat. Nanotechnol.* **2008,** *3* (5), 261-269.

19. Edwardson, J. M.; Henderson, R. M., Atomic force microscopy and drug discovery. *Drug Discovery Today* **2004,** *9* (2), 64-71.

20. Lewandowski, B. R.; Kelley, A. T.; Singleton, R.; Li, J.-R.; Lowry, M.; Warner, I. M.; Garno, J. C., Nanostructures of cysteine-coated CdS nanoparticles produced with "two-particle" lithography. *J. Phys. Chem. C* **2009,** *in press*.

21. Lewandowski, B. R.; Lytle, D. A.; Garno, J. C., Surface Changes During the Initial Stages of Water Corrosion of Copper Investigate by Atomic Force Microscopy: Role of pH and Phosphate. *Environ. Sci. Technol.* **2009,** *submitted*.

22. Lewandowski, B. R.; Lytle, D. A.; Garno, J. C., Impact of pH, Dissolved Inorganic Carbon, and Polyphosphate During the Initial Stages of Water Corrosion of Copper Surfaces Investigated by AFM. *Corros. Sci.* **2009,** *in preparation*.

23. Li, J.-R.; Lewandowski, B. R.; Xu, S.; Garno, J. C., Development of a new hybrid AFM imaging mode for selective mapping of magnetic nanomaterials. *Anal. Chem.* **2009,** *in submission*.

24. Daniels, S. L.; Ngunjiri, J. N.; Garno, J. C., Investigation of the magnetic properties of ferritin by combining AFM imaging with electromagnetic sample modulation. *Anal. Bioanal. Chem.* **2009,** *in press*.

25. Hulteen, J. C.; Treichel, D. A.; Smith, M. T.; Duval, M. L.; Jensen, T. R.; Van Duyne, R. P., Nanosphere lithography: Size-tunable silver nanoparticle and surface cluster arrays. *J. Phys. Chem. B* **1999,** *103* (19), 3854-3863.

26. Haynes, C. L.; Van Duyne, R. P., Nanosphere lithography: A versatile nanofabrication tool for studies of size-dependent nanoparticle optics. *J. Phys. Chem. B* **2001,** *105* (24), 5599-5611.

27. Yang, S.-M.; Jang, S. G.; Choi, D.-G.; Kim, S.; Yu, H. K., Nanomachining by colloidal lithography. *Small* **2006,** *2* (4), 458-475.

28. Wang, D.; Salgueirino-Maceira, V.; Liz-Marzan, L. M.; Caruso, F., Gold-silica inverse opals by colloidal crystal templating. *Adv. Mater.* **2002,** *14* (12), 908-912.

29. Meng, Q.-B.; Fu, C.-H.; Einaga, Y.; Gu, Z.-Z.; Fujishima, A.; Sato, O., Assembly of highly ordered three-dimensional porous structure with nanocrystalline TiO2 semiconductors. *Chem. Mater.* **2002,** *14* (1), 83-88.

30. Wang, D.; Caruso, F., Lithium niobate inverse opals prepared by templating colloidal crystals of polyelectrolyte-coated spheres. *Adv. Mater.* **2003,** *15* (3), 205-210.

31. Wang, D.; Caruso, F., Fabrication of polyaniline inverse opals via templating ordered colloidal assemblies. *Adv. Mater.* **2001,** *13* (5), 350-353.

32. Jiang, P.; Bertone, J. F.; Colvin, V. L., A lost-wax approach to monodisperse colloids and their crystals. *Science* **2001,** *291* (5503), 453-457.

33. Wang, X. D.; Graugnard, E.; King, J. S.; Wang, Z. L.; Summers, C. J., Large-scale fabrication of ordered nanobowl arrays. *Nano Lett.* **2004,** *4* (11), 2223-2226.

34. Chen, J.; Liao, W.-S.; Chen, X.; Yang, T.; Wark, S. E.; Son, D. H.; Batteas, J. D.; Cremer, P. S., Evaporation-induced assembly of quantum dots into nanorings. *ACS Nano* **2009,** *3* (1), 173-180.

35. Garno, J. C.; Amro, N. A.; Wadu-Mesthrige, K.; Liu, G.-Y., Production of periodic arrays of protein nanostructures using particle lithography. *Langmuir* **2002,** *18* (21), 8186-8192.

36. Li, J.-R.; Henry, G. C.; Garno, J. C., Fabrication of nanopatterned films of bovine serum albumin and staphylococcal protein A using latex particle lithography. *Analyst* **2006,** *131* (2), 244-250.

37. Ngunjiri, J. N.; Daniels, S. L.; Li, J.-R.; Serem, W. K.; Garno, J. C., Controlling the surface coverage and arrangement of proteins using particle lithography. *Nanomedicine* **2008,** *3* (4), 529-541.

38. Frey, W.; Woods, C. K.; Chilkoti, A., Ultraflat nanosphere lithography: A new method to fabricate flat nanostructures. *Adv. Mater.* **2000,** *12* (20), 1515-1519.

39. Xia, Y.; Gates, B.; Yin, Y.; Lu, Y., Monodispersed colloidal spheres: Old materials with new applications. *Adv. Mater.* **2000,** *12* (10), 693-713.

40. Jiang, P.; Hwang, K. S.; Mittleman, D. M.; Bertone, J. F.; Colvin, V. L., Template-directed preparation of macroporous polymers with oriented and crystalline arrays of voids. *J. Am. Chem. Soc.* **1999,** *121* (50), 11630-11637.

41. Denis, F. A.; Hanarp, P.; Sutherland, D. S.; Dufrene, Y. F., Nanoscale chemical patterns fabricated by using colloidal lithography and self-assembled monolayers. *Langmuir* **2004,** *20* (21), 9335-9339.

42. Michel, R.; Reviakine, I.; Sutherland, D.; Fokas, C.; Csucs, G.; Danuser, G.; Spencer, N. D.; Textor, M., A novel approach to produce biologically relevant chemical patterns at the nanometer scale: Selective molecular assembly patterning combined with colloidal lithography. *Langmuir* **2002,** *18* (22), 8580-8586.

43. Serem, W. K.; Varotto, A.; Castro, G.; Drain, C. M.; Garno, J. C., Investigation of the vibrational response of individual nanoparticles using AFM with magnetic sample modulation. *NOBCChE Proceedings* **2008**.

44. Li, J.-R.; Verberne-Sutton, S.; Lin, X.-M.; Garno, J. C., Controlling the arrangement of cobalt nanoparticles with mesoparticle templates. **2009,** *in preparation*.

45. McLellan, J. M.; Geissler, M.; Xia, Y., Edge spreading lithography and its application to the fabrication of mesoscopic gold and silver rings. *J. Am. Chem. Soc.* **2004,** *126* (35), 10830-10831.

46. Bae, C.; Moon, J.; Shin, H.; Kim, J.; Sung, M. M., Fabrication of monodisperse asymmetric colloidal clusters by using contact area lithography (CAL). *J. Am. Chem. Soc.* **2007,** *129* (46), 14232-14239.

47. Li, J.-R.; Garno, J. C., Elucidating the role of surface hydrolysis in preparing organosilane nanostructures via particle lithography. *Nano Lett.* **2008,** *8* (7), 1916-1922.

48. USEPA Lead and copper rule: A quick reference guide http://www.epa.gov/ogwdw/lcrmr/pdfs/qrg_lcmr_2004.pdf. (accessed February 2, 2009).

49. Binnig, G.; Rohrer, H.; Gerber, C.; Weibel, E., Tunneling through a controllable vacuum gap. *Appl. Phys. Lett.* **1982,** *40* (2), 178-180.

50. Binnig, G.; Quate, C. F.; Gerber, C., Atomic force microscope. *Phys. Rev. Lett.* **1986,** *56* (9), 930-933.

51. Wiesendanger, R., *Scanning Probe Microscopy and Specroscopy*. Cambridge University Press: Cambridge, United Kingdom, 1994.

52. Radmacher, M.; Tillmann, R. W.; Fritz, M.; Gaub, H. E., From molecules to cells - imaging soft samples with the atomic force microscope. *Science* **1992,** *257* (5078), 1900-1905.

53. Drake, B.; Prater, C. B.; Weisenhorn, A. L.; Gould, S. A. C.; Albrecht, T. R.; Quate, C. F.; Cannell, D. S.; Hansma, H. G.; Hansma, P. K., Imaging crystals, polymers, and processes in water with the atomic force microscope. *Science* **1989,** *243* (4898), 1586-1589.

54. Zhong, Q.; Inniss, D.; Kjoller, K.; Elings, V. B., Fractured polymer silica fiber surface studied by tapping mode atomic-force microscopy. *Surf. Sci.* **1993,** *290* (1-2), L688-L692.

55. Putman, C. A. J.; Van der Werf, K. O.; De Grooth, B. G.; Van Hulst, N. F.; Greve, J., Tapping mode atomic-force microscopy in liquid. *Appl. Phys. Lett.* **1994,** *64* (18), 2454-2456.

56. Hansma, P. K.; Cleveland, J. P.; Radmacher, M.; Walters, D. A.; Hillner, P. E.; Bezanilla, M.; Fritz, M.; Vie, D.; Hansma, H. G.; Prater, C. B.; Massie, J.; Fukunaga, L.; Gurley, J.; Elings, V., Tapping mode atomic-force microscopy in liquids. *Appl. Phys. Lett.* **1994,** *64* (13), 1738-1740.

57. Tamayo, J.; Garcia, R., Deformation, contact time, and phase contrast in tapping mode scanning force microscopy. *Langmuir* **1996,** *12* (18), 4430-4435.

58. Moller, C.; Allen, M.; Elings, V.; Engel, A.; Muller, D. J., Tapping-mode atomic force microscopy produces faithful high-resolution images of protein surfaces. *Biophys. J.* **1999,** *77* (2), 1150-1158.

59. Thomson, N. H.; Fritz, M.; Radmacher, M.; Cleveland, J. P.; Schmidt, C. F.; Hansma, P. K., Protein tracking and detection of protein motion using atomic force microscopy. *Biophys. J.* **1996,** *70* (5), 2421-2431.

60. Kasas, S.; Thomson, N. H.; Smith, B. L.; Hansma, H. G.; Zhu, X.; Guthold, M.; Bustamante, C.; Kool, E. T.; Kashlev, M.; Hansma, P. K., Escherichia coli RNA polymerase activity observed using atomic force microscopy. *Biochemistry* **1997,** *36* (3), 461-468.

61. Gosal, W. S.; Myers, S. L.; Radford, S. E.; Thomson, N. H., Amyloid under the atomic force microscope. *Protein Pept. Lett.* **2006,** *13* (3), 261-270.

62. Kelley, T. W.; Granstrom, E. L.; Frisbie, C. D., Conducting probe atomic force microscopy: A characterization tool for molecular electronics. *Adv. Mater.* **1999,** *11* (3), 261-264.

63. Gomez-Navarro, C.; Moreno-Herrero, F.; de Pablo, P. J.; Colchero, J.; Gomez-Herrero, J.; Baro, A. M., Contactless experiments on individual DNA molecules show no evidence for molecular wire behavior. *Proc. Nat. Acad. Sci. U.S.A.* **2002,** *99* (13), 8484-8487.

64. Cui, X. D.; Primak, A.; Zarate, X.; Tomfohr, J.; Sankey, O. F.; Moore, A. L.; Moore, T. A.; Gust, D.; Harris, G.; Lindsay, S. M., Reproducible measurement of single-molecule conductivity. *Science* **2001,** *294* (5542), 571-574.

65. Seferos, D. S.; Blum, A. S.; Kushmerick, J. G.; Bazan, G. C., Single-molecule charge-transport measurements that reveal technique-dependent perturbations. *J. Am. Chem. Soc.* **2006,** *128* (34), 11260-11267.

66. Wold, D. J.; Frisbie, C. D., Fabrication and characterization of metal-molecule-metal junctions by conducting probe atomic force microscopy. *J. Am. Chem. Soc.* **2001,** *123* (23), 5549-5556.

67. Tivanski, A. V.; Walker, G. C., Ferrocenylundecanethiol self-assembled monolayer charging correlates with negative differential resistance measured by conducting probe atomic force microscopy. *J. Am. Chem. Soc.* **2005,** *127* (20), 7647-7653.

68. Rawlett, A. M.; Hopson, T. J.; Nagahara, L. A.; Tsui, R. K.; Ramachandran, G. K.; Lindsay, S. M., Electrical measurements of a dithiolated electronic molecule via conducting atomic force microscopy. *Appl. Phys. Lett.* **2002,** *81* (16), 3043-3045.

69. Overney, R. M.; Meyer, E.; Frommer, J.; Guntherodt, H. J.; Fujihira, M.; Takano, H.; Gotoh, Y., Force microscopy study of friction and elastic compliance of phase-separated organic thin-films. *Langmuir* **1994,** *10* (4), 1281-1286.

70. Bar, G.; Rubin, S.; Parikh, A. N.; Swanson, B. I.; Zawodzinski, T. A.; Whangbo, M. H., Scanning force microscopy study of patterned monolayers of alkanethiols on gold. Importance of tip-sample contact area in interpreting force modulation and friction force microscopy images. *Langmuir* **1997,** *13* (3), 373-377.

71. Price, W. J.; Leigh, S. A.; Hsu, S. M.; Patten, T. E.; Liu, G. Y., Measuring the size dependence of Young's modulus using force modulation atomic force microscopy. *J. Phys. Chem. A* **2006,** *110* (4), 1382-1388.

72. Kiridena, W.; Jain, V.; Kuo, P. K.; Liu, G.-Y., Nanometer-scale elasticity measurements on organic monolayers using scanning force microscopy. *Surf. Interface Anal.* **1997,** *25* (6), 383-389.

73. Martin, Y.; Wickramasinghe, H. K., Magnetic imaging by force microscopy with 1000-A resolution. *Appl. Phys. Lett.* **1987,** *50* (20), 1455-1457.

74. Saenz, J. J.; Garcia, N.; Grutter, P.; Meyer, E.; Heinzelmann, H.; Wiesendanger, R.; Rosenthaler, L.; Hidber, H. R.; Guntherodt, H. J., Observation of magnetic forces by the atomic force microscope. *J. Appl. Phys.* **1987,** *62* (10), 4293-4295.

75. Bhushan, B., *Tribology of magnetic storage systems*. John Wiley & Sons: 1998.

76. Rugar, D.; Mamin, H. J.; Guethner, P.; Lambert, S. E.; Stern, J. E.; McFadyen, I.; Yogi, T., Magnetic Force Microscopy - General-principles and application to longitudinal recording media. *J. Appl. Phys.* **1990,** *68* (3), 1169-1183.

77. Hansma, P. K.; Elings, V. B.; Marti, O.; Bracker, C. E., Scanning tunneling microscopy and atomic force microscopy - application to biology and technology. *Science* **1988,** *242* (4876), 209-216.

78. Schitter, G.; Menold, P.; Knapp, H. F.; Allgower, F.; Stemmer, A., High performance feedback for fast scanning atomic force microscopes. *Rev. Sci. Instrum.* **2001,** *72* (8), 3320-3327.

79. Ando, T.; Kodera, N.; Takai, E.; Maruyama, D.; Saito, K.; Toda, A., A high-speed atomic force microscope for studying biological macromolecules. *Proc. Nat. Acad. Sci. U.S.A.* **2001,** *98* (22), 12468-12472.

80. Schitter, G.; Allgower, F.; Stemmer, A., A new control strategy for high-speed atomic force miciroscopy. *Nanotechnology* **2004,** *15* (1), 108-114.

81. Schitter, G.; Stark, R. W.; Stemmer, A., Fast contact-mode atomic force microscopy on biological specimen by model-based control. *Ultramicroscopy* **2004,** *100* (3-4), 253-257.

82. DeVecchio, D.; Bhushan, B., Localized surface elasticity measurements using an atomic force microscope. *Rev. Sci. Instrum.* **1997,** *68* (12), 4498-4505.

83. Jourdan, J. S.; Cruchon-Dupeyrat, S. J.; Huan, Y.; Kuo, P. K.; Liu, G. Y., Imaging nanoscopic elasticity of thin film materials by atomic force microscopy: Effects of force modulation frequency and amplitude. *Langmuir* **1999,** *15* (19), 6495-6504.

84. Price, W. J.; Kuo, P. K.; Lee, T. R.; Colorado, R.; Ying, Z. C.; Liu, G. Y., Probing the local structure and mechanical response of nanostructures using force modulation and nanofabrication. *Langmuir* **2005,** *21* (18), 8422-8428.

85. Stark, M.; Moller, C.; Muller, D. J.; Guckenberger, R., From images to interactions: High-resolution phase imaging in tapping-mode atomic force microscopy. *Biophys. J.* **2001,** *80* (6), 3009-3018.

86. Hierlemann, A.; Campbell, J. K.; Baker, L. A.; Crooks, R. M.; Ricco, A. J., Structural distortion of dendrimers on gold surfaces: A tapping-mode AFM investigation. *J. Am. Chem. Soc.* **1998,** *120* (21), 5323-5324.

87. Raghavan, D.; Gu, X.; Nguyen, T.; Van Landingham, M.; Karim, A., Mapping polymer heterogeneity using atomic force microscopy phase imaging and nanoscale indentation. *Macromolecules* **2000,** *33* (7), 2573-2583.

88. Lindsay, S. M.; Lyubchenko, Y. L.; Tao, N. J.; Li, Y. Q.; Oden, P. I.; Derose, J. A.; Pan, J., Scanning-tunneling-microscopy and atomic-force microscopy studies of biomaterials at a liquid-solid interface. *J. Vac. Sci. Technol., A* **1993,** *11* (4), 808-815.

89. Han, W. H.; Lindsay, S. M.; Jing, T. W., A magnetically driven oscillating probe microscope for operation in liquids. *Appl. Phys. Lett.* **1996,** *69* (26), 4111-4113.

90. Leuba, S. H.; Lindsay, S. M., Magnetically driven oscillating probe ("MAC mode") scanning force microscopy (SFM) of chromatin fibers in aqueous buffer. *Biophys. J.* **1998,** *74* (2), A71.

91. Kienberger, F.; Stroh, C.; Kada, G.; Moser, R.; Baumgartner, W.; Pastushenko, V.; Rankl, C.; Schmidt, U.; Muller, H.; Orlova, E.; LeGrimellec, C.; Drenckhahn, D.; Blaas, D.; Hinterdorfer, P., Dynamic force microscopy imaging of native membranes. *Ultramicroscopy* **2003,** *97* (1-4), 229-237.

92. Ge, G. L.; Han, D.; Lin, D. Y.; Chu, W. G.; Sun, Y. X.; Jiang, L.; Ma, W. Y.; Wang, C., MAC mode atomic force microscopy studies of living samples, ranging from cells to fresh tissue. *Ultramicroscopy* **2007,** *107* (4-5), 299-307.

93. Hehn, M.; Padovani, S.; Ounadjela, K.; Bucher, J. P., Nanoscale magnetic domain structures in epitaxial cobalt films. *Phys. Rev. B: Condens. Matter* **1996,** *54* (5), 3428-3433.

94. Porthun, S.; Abelmann, L.; Lodder, C., Magnetic force microscopy of thin film media for high density magnetic recording. *J. Magn. Magn. Mater.* **1998,** *182* (1-2), 238-273.

95. Belliard, L.; Miltat, J.; Thiaville, A.; Dubois, S.; Duvail, J. L.; Piraux, L., Observing magnetic nanowires by means of magnetic force microscopy. *J. Magn. Magn. Mater.* **1998,** *190* (1-2), 1-16.

96. Qin, D. H.; Lu, M.; Li, H. L., Magnetic force microscopy of magnetic domain structure in highly ordered Co nanowire arrays. *Chem. Phys. Lett.* **2001,** *350* (1-2), 51-56.

97. Puntes, V. F.; Gorostiza, P.; Aruguete, D. M.; Bastus, N. G.; Alivisatos, A. P., Collective behaviour in two-dimensional cobalt nanoparticle assemblies observed by magnetic force microscopy. *Nat. Mater.* **2004,** *3* (4), 263-268.

98. Rugar, D.; Yannoni, C. S.; Sidles, J. A., Mechanical detection of magnetic-resonance. *Nature* **1992,** *360* (6404), 563-566.

99. Sidles, J. A.; Garbini, J. L.; Bruland, K. J.; Rugar, D.; Zuger, O.; Hoen, S.; Yannoni, C. S., Magnetic-resonance force microscopy. *Rev. Mod. Phys.* **1995,** *67* (1), 249-265.

100. Zhang, Z.; Hammel, P. C.; Wigen, P. E., Observation of ferromagnetic resonance in a microscopic sample using magnetic resonance force microscopy. *Appl. Phys. Lett.* **1996,** *68* (14), 2005-2007.

101. Rugar, D.; Budakian, R.; Mamin, H. J.; Chui, B. W., Single spin detection by magnetic resonance force microscopy. *Nature* **2004,** *430* (6997), 329-332.

102. Florin, E. L.; Radmacher, M.; Fleck, B.; Gaub, H. E., Atomic-force microscope with magnetic force modulation. *Rev. Sci. Instrum.* **1994,** *65* (3), 639-643.

103. Yamamoto, S.; Yamada, H., Interpretation of direct and indirect force modulation methods using polymer films. *Langmuir* **1997,** *13* (18), 4861-4864.

104. Schemmel, A.; Gaub, H. E., Single molecule force spectrometer with magnetic force control and inductive detection. *Rev. Sci. Instrum.* **1999,** *70* (2), 1313-1317.

105. Scherer, M. P.; Gummer, A. W., Impedance analysis of the organ of corti with magnetically actuated probes. *Biophys. J.* **2004,** *87* (2), 1378-1391.

106. Stoeva, S. I.; Prasad, B. L. V.; Uma, S.; Stoimenov, P. K.; Zaikovski, V.; Sorensen, C. M.; Klabunde, K. J., Face-centered cubic and hexagonal closed-packed nanocrystal superlattices of gold nanoparticles prepared by different methods. *J. Phys. Chem. B* **2003,** *107* (30), 7441-7448.

107. Kiely, C. J.; Fink, J.; Brust, M.; Bethell, D.; Schiffrin, D. J., Spontaneous ordering of bimodal ensembles of nanoscopic gold clusters. *Nature* **1998,** *396* (6710), 444-446.

108. Pileni, M. P., Nanosized particles made in colloidal assemblies. *Langmuir* **1997,** *13* (13), 3266-3276.

109. Murray, C. B.; Kagan, C. R.; Bawendi, M. G., Synthesis and characterization of monodisperse nanocrystals and close-packed nanocrystal assemblies. *Ann. Rev. Mater. Sci.* **2000,** *30*, 545-610.

110. Shevchenko, E. V.; Ringler, M.; Schwemer, A.; Talapin, D. V.; Klar, T. A.; Rogach, A. L.; Feldmann, J.; Alivisatos, A. P., Self-assembled binary superlattices of CdSe and Au nanocrystals and their fluorescence properties. *J. Am. Chem. Soc.* **2008,** *130* (11), 3274-+.

111. Nordlander, P.; Oubre, C.; Prodan, E.; Li, K.; Stockman, M. I., Plasmon hybridizaton in nanoparticle dimers. *Nano Lett.* **2004,** *4* (5), 899-903.

112. Bouhelier, A.; Bachelot, R.; Im, J. S.; Wiederrecht, G. P.; Lerondel, G.; Kostcheev, S.; Royer, P., Electromagnetic interactions in plasmonic nanoparticle arrays. *J. Phys. Chem. B* **2005,** *109* (8), 3195-3198.

113. Kang, Y. J.; Erickson, K. J.; Taton, T. A., Plasmonic nanoparticle chains via a morphological, sphere-to-string transition. *J. Am. Chem. Soc.* **2005,** *127* (40), 13800-13801.

114. Huang, W. Y.; Qian, W.; Jain, P. K.; El-Sayed, M. A., The effect of plasmon field on the coherent lattice phonon oscillation in electron-beam fabricated gold nanoparticle pairs. *Nano Lett.* **2007,** *7* (10), 3227-3234.

115. Koenderink, A. F.; Hernandez, J. V.; Robicheaux, F.; Noordam, L. D.; Polman, A., Programmable nanolithography with plasmon nanoparticle arrays. *Nano Lett.* **2007,** *7* (3), 745-749.

116. El-Kouedi, M.; Foss, C. A., Optical properties of gold-silver iodide nanoparticle pair structures. *J. Phys. Chem. B* **2000,** *104* (17), 4031-4037.

117. Henzie, J.; Shuford, K. L.; Kwak, E. S.; Schatz, G. C.; Odom, T. W., Manipulating the optical properties of pyramidal nanoparticle arrays. *J. Phys. Chem. B* **2006,** *110* (29), 14028-14031.

118. He, S. T.; Yao, J. N.; Jiang, P.; Shi, D. X.; Zhang, H. X.; Xie, S. S.; Pang, S. J.; Gao, H. J., Formation of silver nanoparticles and self-assembled two-dimensional ordered superlattice. *Langmuir* **2001,** *17* (5), 1571-1575.

119. Choi, D. G.; Jang, S. G.; Yu, H. K.; Yang, S. M., Two-dimensional polymer nanopattern by using particle-assisted soft lithography. *Chem. Mater.* **2004,** *16* (18), 3410-3413.

120. Han, S. B.; Briseno, A. L.; Shi, X. Y.; Mah, D. A.; Zhou, F. M., Polyelectrolyte-coated nanosphere lithographic patterning of surfaces: Fabrication and characterization of electropolymerized thin polyaniline honeycomb films. *J. Phys. Chem. B* **2002,** *106* (25), 6465-6472.

121. Yi, D. K.; Kim, D. Y., Polymer nanosphere lithography: fabrication of an ordered trigonal polymeric nanostructure. *Chem. Comm.* **2003,** (8), 982-983.

122. Sun, Z. Q.; Li, Y. F.; Wang, Y. F.; Chen, X.; Zhang, J. H.; Zhang, K.; Wang, Z. F.; Bao, C. X.; Zeng, H.; Zhao, B.; Yang, B., Three-dimensional colloidal crystal-assisted lithography for two-dimensional patterned arrays. *Langmuir* **2007,** *23* (21), 10725-10731.

123. Cai, Y. G.; Ocko, B. M., Large-scale fabrication of protein nanoarrays based on nanosphere lithography. *Langmuir* **2005,** *21* (20), 9274-9279.

124. Valsesia, A.; Meziani, T.; Bretagnol, F.; Colpo, P.; Ceccone, G.; Rossi, F., Plasma assisted production of chemical nano-patterns by nano-sphere lithography: application to bio-interfaces. *J. Phys. D: Appl. Phys.* **2007,** *40* (8), 2341-2347.

125. Zin, M. T.; Leong, K.; Wong, N.-Y.; Ma, H.; Jen, A. K.-Y., Plasmon resonant structures with unique topographic characteristics and tunable optical properties for surface-enhanced Raman scattering. *Nanotechnology* **2007,** *18* (45), 1-6.

126. Winzer, M.; Kleiber, M.; Dix, N.; Wiesendanger, R., Fabrication of nano-dot- and nano-ring-arrays by nanosphere lithography. *Appl. Phys. A* **1996,** *63* (6), 617-619.

127. Sun, F.; Cai, W.; Li, Y.; Duan, G.; Nichols, W. T.; Liang, C.; Koshizaki, N.; Fang, Q.; Boyd, I. W., Laser morphological manipulation of gold nanoparticles periodically arranged on solid supports. *Appl. Phys. B* **2005,** *81* (6), 765-768.

128. Tan, B. J. Y.; Sow, C. H.; Koh, T. S.; Chin, K. C.; Wee, A. T. S.; Ong, C. K., Fabrication of size-tunable gold nanoparticles array with nanosphere lithography, reactive ion etching, and thermal annealing. *J. Phys. Chem. B* **2005,** *109* (22), 11100-11109.

129. Rossi, R. C.; Tan, M. X.; Lewis, N. S., Size-dependent electrical behavior of spatially inhomogeneous barrier height regions on silicon. *Appl. Phys. Lett.* **2000,** *77* (17), 2698-2700.

130. Bullen, H. A.; Garrett, S. J., TiO_2 nanoparticle arrays prepared using a nanosphere lithography technique. *Nano Lett.* **2002,** *2* (7), 739-745.

131. Cheng, S. L.; Lu, S. W.; Wong, S. L.; Chang, C. C.; Chen, H., Fabrication of 2D ordered arrays of cobalt silicide nanodots on (001)Si substrates. *J. Crystal Growth* **2007,** *300* (2), 473-477.

132. Zhang, K.; Chang, H. Y.; Fu, A. H.; Alivisatos, A. P.; Yang, H., Continuous distribution of emission states from single CdSe/ZnS quantum dots. *Nano Lett.* **2006,** *6* (4), 843-847.

133. Liu, D. F.; Xiang, Y. J.; Liao, Q.; Zhang, J. P.; Wu, X. C.; Zhang, Z. X.; Liu, L. F.; Ma, W. J.; Shen, J.; Zhou, W. Y.; Xie, S. S., A simple route to scalable fabrication of perfectly ordered ZnO nanorod arrays. *Nanotechnology* **2007,** *18* (40), 1-5.

134. Li, Y.; Li, C. C.; Cho, S. O.; Duan, G. T.; Cai, W. P., Silver hierarchical bowl-like array: synthesis, superhydrophobicity, and optical properties. *Langmuir* **2007,** *23* (19), 9802-9807.

135. Weekes, S. M.; Ogrin, F. Y.; Murray, W. A.; Keatley, P. S., Macroscopic arrays of magnetic nanostructures from self-assembled nanosphere templates. *Langmuir* **2007,** *23* (3), 1057-1060.

136. Ctistis, G.; Patoka, P.; Wang, X.; Kempa, K.; Giersig, M., Optical transmission through hexagonal arrays of subwavelength holes in thin metal films. *Nano Lett.* **2007,** *7* (9), 2926-2930.

137. Ryu, K. S.; Wang, X.; Shaikh, K.; Bullen, D.; Goluch, E.; Zou, J.; Liu, C., Integrated microfluidic linking chip for scanning probe nanolithography. *Appl. Phys. Letts.* **2004,** *85* (1), 136-138.

138. McLellan, J. M.; Geissler, M.; Xia, Y. N., Edge spreading lithography and its application to the fabrication of mesoscopic gold and silver rings. *J. Am. Chem. Soc.* **2004,** *126* (35), 10830-10831.

139. Geissler, M.; McLellan, J. M.; Chen, J. Y.; Xia, Y. N., Side-by-side patterning of multiple alkanethiolate monolayers on gold by edge-spreading lithography. *Angew. Chem. Int. Ed.* **2005,** *44* (23), 3596-3600.

140. Wang, X. D.; Summers, C. J.; Wang, Z. L., Large-scale hexagonal-patterned growth of aligned ZnO nanorods for nano-optoelectronics and nanosensor arrays. *Nano Lett.* **2004,** *4* (3), 423-426.

141. Wu, W.; Katsnelson, A.; Memis, O. G.; Mohseni, H., A deep sub-wavelength process for the formation of highly uniform arrays of nanoholes and nanopillars. *Nanotechnology* **2007,** *18* (48), 1-4.

142. Pacifico, J.; Gomez, D.; Mulvaney, P., A simple route to tunable two-dimensional arrays of quantum dots. *Adv. Mater.* **2005,** *17* (4), 415-+.

143. Tessier, P. M.; Velev, O. D.; Kalambur, A. T.; Lenhoff, A. M.; Rabolt, J. F.; Kaler, E. W., Stuctured metallic films for optical and spectroscopic applications via colloidal crystal templating. *Adv. Mater.* **2001,** *13* (6), 396-400.

144. Choi, D. G.; Yu, H. K.; Jang, S. G.; Yang, S. M., Colloidal lithographic nanopatterning via reactive ion etching. *J. Am. Chem. Soc.* **2004,** *126* (22), 7019-7025.

145. Zhang, G.; Wang, D. Y.; Mohwald, H., Decoration of microspheres with gold nanodots-giving colloidal spheres valences. *Angew. Chem. Int. Ed.* **2005,** *44* (47), 7767-7770.

146. Holland, B. T.; Blanford, C. F.; Do, T.; Stein, A., Synthesis of highly ordered, three-dimensional, macroporous structures of amorphous or crystalline inorganic oxides, phosphates, and hybrid composites. *Chem. Mater.* **1999,** *11* (3), 795-805.

147. Cao, B. Q.; Cai, W. P.; Sun, F. Q.; Li, Y.; Lei, Y.; Zhang, L. D., Fabrication of large-scale zinc oxide ordered pore arrays with controllable morphology. *Chem. Comm.* **2004,** (14), 1604-1605.

148. Velev, O. D.; Jede, T. A.; Lobo, R. F.; Lenhoff, A. M., Microstructured porous silica obtained via colloidal crystal templates. *Chem. Mater.* **1998,** *10* (11), 3597-3602.

149. Gates, B.; Yin, Y.; Xia, Y., Fabrication and characterization of porous membranes with highly ordered three-dimensional periodic structures. *Chem. Mater.* **1999,** *11* (10), 2827-2836.

150. Subramania, G.; Constant, K.; Biswas, R.; Sigalas, M. M.; Ho, K.-M., Inverse face-centered cubic thin film photonic crystals. *Adv. Mater.* **2001,** *13* (6), 443-446.

151. Ozin, G. A.; Yang, S. M., The race for the photonic chip: Colloidal crystal assembly in silicon wafers. *Adv. Funct. Mater.* **2001,** *11* (2), 95-104.

152. Haes, A. J.; Hall, W. P.; Chang, L.; Klein, W. L.; Van Duyne, R. P., A localized surface plasmon resonance biosensor: First steps toward an assay for Alzheimer's disease. *Nano Lett.* **2004,** *4* (6), 1029-1034.

153. Riboh, J. C.; Haes, A. J.; McFarland, A. D.; Yonzon, C. R.; Van Duyne, R. P., A nanoscale optical biosensor: Real-time immunoassay in physiological buffer enabled by improved nanoparticle adhesion. *J. Phys. Chem. B* **2003,** *107* (8), 1772-1780.

154. Baumberg, J. J.; Kelf, T. A.; Sugawara, Y.; Cintra, S.; Abdelsalam, M. E.; Bartlett, P. N.; Russell, A. E., Angle-resolved surface-enhanced Raman scattering on metallic nanostructured plasmonic crystals. *Nano Lett.* **2005,** *5* (11), 2262-2267.

155. Schmidt, J. P.; Cross, S. E.; Buratto, S. K., Surface-enhanced Raman scattering from ordered Ag nanocluster arrays. *J. Chem. Phys.* **2004,** *121* (21), 10657-10659.

156. Haynes, C. L.; Van Duyne, R. P., Plasmon-sampled surface-enhanced Raman excitation spectroscopy. *J. Phys. Chem. B* **2003,** *107* (30), 7426-7433.

157. Mahajan, S.; Abdelsalam, M.; Suguwara, Y.; Cintra, S.; Russell, A.; Baumberg, J.; Bartlett, P., Tuning plasmons on nano-structured substrates for NIR-SERS. *Phys. Chem. Chem. Phys.* **2007,** *9* (1), 104-109.

158. Cintra, S.; Abdelsalam, M. E.; Bartlett, P. N.; Baumberg, J. J.; Kelf, T. A.; Sugawara, Y.; Russell, A. E., Sculpted substrates for SERS. *Faraday Discuss.* **2006,** *132*, 191-199.

159. Prevo, B. G.; Velev, O. D., Controlled, rapid deposition of structured coatings from micro- and nanoparticle suspensions. *Langmuir* **2004,** *20* (6), 2099-2107.

160. Park, S. H.; Qin, D.; Xia, Y., Crystallization of mesoscale particles over large areas. *Adv. Mater.* **1998,** *10* (13), 1028-1032.

161. Wang, D. Y.; Mohwald, H., Rapid fabrication of binary colloidal crystals by stepwise spin-coating. *Adv. Mater.* **2004,** *16* (3), 244-247.

162. Amos, R. M.; Rarity, J. G.; Tapster, P. R.; Shepherd, T. J., Fabrication of large-area face-centered-cubic hard-sphere colloidal crystals by shear alignment. *Phys. Rev. E* **2000,** *61* (3), 2929-2935.

163. Marquez, M.; Grady, B. P., The use of surface tension to predict the formation of 2D arrays of latex spheres formed via the Langmuir-Blodgett-like technique. *Langmuir* **2004,** *20* (25), 10998-11004.

164. Hoogenboom, J. P.; Retif, C.; de Bres, E.; van de Boer, M.; van Langen-Suurling, A. K.; Romijn, J.; van Blaaderen, A., Template-induced growth of close-packed and non-close-packed colloidal crystals during solvent evaporation. *Nano Lett.* **2004,** *4* (2), 205-208.

165. Michalet, X.; Pinaud, F.; Lacoste, T. D.; Dahan, M.; Bruchez, M. P.; Alivisatos, A. P.; Weiss, S., Properties of fluorescent semiconductor nanocrystals and their application to biological labeling. *Single Mol.* **2001,** *2* (4), 261-276.

166. Chan, W. C. W.; Nie, S., Quantum dot bioconjugates for ultrasensitive nonisotopic detection. *Science* **1998,** *281* (5385), 2016-2018.

167. Bruchez, M.; Moronne, M.; Gin, P.; Weiss, S.; Alivisatos, A. P., Semiconductor nanocrystals as fluorescent biological labels. *Science* **1998,** *281* (5385), 2013-2016.

168. Hoshino, A.; Fujioka, K.; Oku, T.; Suga, M.; Sasaki, Y. F.; Ohta, T.; Yasuhara, M.; Suzuki, K.; Yamamoto, K., Physicochemical properties and cellular toxicity of nanocrystal quantum dots depend on their surface modification. *Nano Lett.* **2004,** *4* (11), 2163-2169.

169. Derfus, A. M.; Chan, W. C. W.; Bhatia, S. N., Probing the cytotoxicity of semiconductor quantum dots. *Nano Lett.* **2004,** *4* (1), 11-18.

170. Løver, T.; Henderson, W.; Bowmaker, G. A.; Seakins, J. M.; Cooney, R. P., Functionalization and capping of a CdS nanocluster: A study of ligand exchange by electrospray mass spectrometry. *Chem. Mater.* **1997,** *9* (8), 1878-1886.

171. Sachleben, J. R.; Colvin, V.; Emsley, L.; Wooten, E. W.; Alivisatos, A. P., Solution-state NMR studies of the surface structure and dynamics of semiconductor nanocrystals. *J. Phys. Chem. B* **1998,** *102* (50), 10117-10128.

172. Li, H.; Shih, W. Y.; Shih, W. H., Synthesis and characterization of aqueous carboxyl-capped CdS quantum dots for bioapplications. *Ind. Eng. Chem. Res.* **2007,** *46* (7), 2013-2019.

173. Elliott, S. D.; Moloney, M. P.; Gun'ko, Y. K., Chiral shells and achiral cores in CdS quantum dots. *Nano Lett.* **2008,** *8* (8), 2452-2457.

174. Young, A. G.; Al-Salim, N.; Green, D. P.; McQuillan, A. J., Attenuated total reflection infrared studies of oleate and trioctylphosphine oxide ligand adsorption and exchange reactions on CdS quantum dot films. *Langmuir* **2008,** *24* (8), 3841-3849.

175. Miyake, M.; Matsumoto, H.; Nishizawa, M.; Sakata, T.; Mori, H.; Kuwabata, S.; Yoneyama, H., Characterization of covalently immobilized Q-CdS particles on Au(111) by scanning tunneling microscopy and tunneling spectroscopy with high reproducibility. *Langmuir* **1997,** *13* (4), 742-746.

176. Bae, W.; Mehra, R. K., Properties of glutathione- and phytochelatin-capped CdS bionanocrystallites. *J. Inorg. Biochem.* **1998,** *69* (1-2), 33-43.

177. Tsay, J. M.; Trzoss, M.; Shi, L.; Kong, X.; Selke, M.; Jung, M. E.; Weiss, S., Singlet oxygen production by peptide-coated quantum dot-photosensitizer conjugates. *J. Am. Chem. Soc.* **2007,** *129* (21), 6865-6871.

178. Bigham, S. R.; Coffer, J. L., The influence of adenine content on the properties of Q-CdS clusters stabilized by polynucleotides. *Colloids Surf., A* **1995,** *95* (2-3), 211-219.

179. Ma, N.; Yang, J.; Stewart, K. M.; Kelley, S. O., DNA-passivated CdS nanocrystals: Luminescence, bioimaging, and toxicity profiles. *Langmuir* **2007,** *23* (26), 12783-12787.

180. Liang, J.-g.; Ai, X.-p.; He, Z.-k.; Xie, H.-y.; Pang, D.-w., Synthesis and characterization of CdS/BSA nanocomposites. *Mater. Lett.* **2005,** *59* (22), 2778-2781.

181. Xiong, S.; Xi, B.; Wang, C.; Zou, G.; Fei, L.; Wang, W.; Qian, Y., Shape-controlled synthesis of 3D and 1D structures of CdS in a binary solution with L-cysteine's assistance. *Chem. Eur. J.* **2007,** *13* (11), 3076-3081.

182. Cai, Z.-X.; Yang, H.; Zhang, Y.; Yan, X.-P., Preparation, characterization and evaluation of water-soluble L-cysteine-capped-CdS nanoparticles as fluorescence probe for detection of Hg(II) in aqueous solution. *Analyt. Chim. Acta* **2006,** *559* (2), 234-239.

183. Bae, W.; Abdullah, R.; Mehra, R. K., Cysteine-mediated synthesis of CdS bionanocrystallites. *Chemosphere* **1998,** *37* (2), 363-385.

184. Steigerwald, M. L.; Brus, L. E., Semiconductor crystallites: A class of large molecules. *Acc. Chem. Res.* **1990,** *23* (6), 183-188.

185. Brus, L. E., Electron-electron and electron-hole interactions in small semiconductor crystallites: The size dependence of the lowest excited electronic states. *J. Chem. Phys.* **1984,** *80* (9), 4403-4409.

186. Yu, W. W.; Qu, L. H.; Guo, W. Z.; Peng, X. G., Experimental determination of the extinction coefficient of CdTe, CdSe, and CdS nanocrystals. *Chem. Mater.* **2003,** *15* (14), 2854-2860.

187. Klapetek, P.; Necas, D. *Gwyddion* 2.9; Czech Metrology Institute: Czech Republic, 2007.

188. Nazmutdinov, R. R.; Zhang, J. D.; Zinkicheva, T. T.; Manyurov, I. R.; Ulstrup, J., Adsorption and in situ scanning tunneling microscopy of cysteine on Au(111): Structure, energy, and tunneling contrasts. *Langmuir* **2006,** *22* (18), 7556-7567.

189. Wilcox, D.; Dove, B.; McDavid, D.; Greer, D. *UTHSCA Image Tool v. 3.00*, The University of Texas Health Science Center in San Antonio: San Antonio, TX, 1995-2002.

190. Kim, A. J.; Manoharan, V. N.; Crocker, J. C., Swelling-based method for preparing stable, functionalized polymer colloids. *J. Am. Chem. Soc.* **2005,** *127* (6), 1592-1593.

191. Chen, Y. Y.; Ford, W. T.; Materer, N. F.; Teeters, D., Conversion of colloidal crystals to polymer nets: Turning latex particles inside out. *Chem. Mater.* **2001,** *13* (8), 2697-2704.

192. Verberne-Sutton, S.; Li, J.-R.; Lin, X.-M.; Garno, J. C., *Abstracts, 60th Southeast Regional Meeting of the American Chemical Society* **2008**, Nashville, TN.

193. Lebrini, M.; Bentiss, F.; Chihib, N. E.; Jama, C.; Hornez, J. P.; Lagrenee, M., Polyphosphate derivatives of guanidine and urea copolymer: Inhibiting corrosion effect of armco iron in acid solution and antibacterial activity. *Corros. Sci.* **2008,** *50* (10), 2914-2918.

194. Ramesh, S.; Rajeswari, S.; Maruthamuthu, S., Corrosion inhibition of copper by new triazole phosphonate derivatives. *Appl. Surf. Sci.* **2004,** *229* (1-4), 214-225.

195. Laamari, M. R.; Derja, A.; Benzakour, J.; Berraho, M., Calcium monofluorophosphate: a new class of corrosion inhibitors in NaCl medium. *J. Electroanal. Chem.* **2004,** *569* (1), 1-6.

196. Amar, H.; Benzakour, J.; Derja, A.; Villemin, D.; Moreau, B., A corrosion inhibition study of iron by phosphonic acids in sodium chloride solution. *J. Electroanal. Chem.* **2003,** *558*, 131-139.

197. Truc, T. A.; Pebere, N.; Hang, T. T. X.; Hervaud, Y.; Boutevin, B., Study of the synergistic effect observed for the corrosion protection of a carbon steel by an association of phosphates. *Corros. Sci.* **2002,** *44* (9), 2055-2071.

198. Edwards, M.; Hidmi, L.; Gladwell, D., Phosphate inhibition of soluble copper corrosion by-product release. *Corros. Sci.* **2002,** *44* (5), 1057-1071.

199. Telegdi, J.; Shaglouf, M. M.; Shaban, A.; Karman, F. H.; Betroti, I.; Mohai, M.; Kalman, E., Influence of cations on the corrosion inhibition efficiency of aminophosphonic acid. *Electrochim. Acta* **2001,** *46*.

200. Sanchez, J.; Fullea, J.; Andrade, C.; Gaitero, J. J.; Porro, A., AFM study of the early corrosion of a high strength steel in a diluted sodium chloride solution. *Corros. Sci.* **2008,** *50* (7), 1820-1824.

201. Martin, F. A.; Bataillon, C.; Cousty, J., In situ AFM detection of pit onset location on a 304L stainless steel. *Corros. Sci.* **2008,** *50* (1), 84-92.

202. Wang, R., An AFM and XPS study of corrosion caused by micro-liquid of dilute sulfuric acid on stainless steel. *Appl. Surf. Sci.* **2004,** *227* (1-4), 399-409.

203. Kleber, C.; Wiesinger, R.; Schnoller, J.; Hilfrich, U.; Hutter, H.; Schreiner, M., Initial oxidation of silver surfaces by S2- and S4+ species. *Corros. Sci.* **2008,** *50* (4), 1112-1121.

204. Schmitz, I.; Schreiner, M.; Friedbacher, G.; Grasserbauer, M., Tapping-mode AFM in comparison to contact-mode AFM as a tool for in situ investigations of surface reactions with reference to glass corrosion. *Anal. Chem.* **1997,** *69* (6), 1012-1018.

205. Kleber, C.; Hilfrich, U.; Schreiner, M., In situ QCM and TM-AFM investigations of the early stages of degradation of silver and copper surfaces. *Appl. Surf. Sci.* **2007,** *253* (7), 3712-3721.

206. Aastrup, T.; Wadsak, M.; Schreiner, M.; Leygraf, C., Experimental in situ studies of copper exposed to humidified air. *Corros. Sci.* **2000,** *42* (6), 957-967.

207. Li, J.; Lampner, D., In-situ AFM study of pitting corrosion of Cu thin films. *Colloids Surf., A* **1999,** *154* (1-2), 227-237.

208. Wadsak, M.; Schreiner, M.; Aastrup, T.; Leygraf, C., A comparison of preparation methods of copper surfaces for in situ scanning force microscopy investigations. *Appl. Surf. Sci.* **2000,** *157* (1-2), 39-46.

209. Otmacic, H.; Telegdi, J.; Papp, K.; Stupnisek-Lisac, E., Protective properties of an inhibitor layer formed on copper in neutral chloride solution. *J. Appl. Electrochem.* **2004,** *34* (5), 545-550.

210. Li, X. H.; Mu, G. N., Tween-40 as corrosion inhibitor for cold rolled steel in sulphuric acid: Weight loss study, electrochemical characterization, and AFM. *Appl. Surf. Sci.* **2005,** *252* (5), 1254-1265.

211. Zhang, D. Q.; An, Z. X.; Pan, Q. Y.; Gao, L. X.; Zhou, G. D., Volatile corrosion inhibitor film formation on carbon steel surface and its inhibition effect on the atmospheric corrosion of carbon steel. *Appl. Surf. Sci.* **2006,** *253* (3), 1343-1348.

212. Klapetek, P.; Necas, D. *Gwyddion, http://gwyddion.net/*, Czech Metrology Institute: Czech Republic, 2007.

213. Wilcox, D.; Dove, B.; McDavid, D.; Greer, D. *UTHSCSA Image Tool for Windows version 3.00*, The University of Texas Health Science Center San Antonio, TX, 1995-2002.

214. Telegdi, J.; Shaglouf, M. M.; Shaban, A.; Karma´n, F. H.; Betroti, I.; Mohai, M.; Kalman, E., Influence of cations on the corrosion inhibition efficiency of aminophosphonic acid. *Electrochimica Acta* **2001,** *46*, 3791-3799.

215. Vastag, G.; E. Szöcs; Shaban, A.; Kálmán, E., New inhibitors for copper corrosion. *Pure Appl. Chem.* **2001,** *73* (12), 1861-1869.

216. Xu, L.; Chan, K.; Fang, H. H. P., Application of atomic force microscopy in the study of microbiologically influenced corrosion. *Materials Characterization* **2002,** *48* (2-3), 195-203.

217. Mu, G.; Li, X., Inhibition of cold rolled steel corrosion by tween-20 in sulfuric acid: weight loss, electrochemical and AFM approaches. *Journal of Colloid and Interface Science* **2005,** *289* (1), 184-192.

218. Olivares-Xometl, O.; Likhanova, N. V.; Dominguez-Aguilar, M. A.; Hallen, J. M.; Zamudio, L. S.; Arce, E., Surface analysis of inhibitor films formed by imidazolines and amides on mild steel in an acidic environment. *Appl. Surf. Sci.* **2006,** *252* (6), 2139-2152.

219. Skolnik, A. M.; Hughes, W. C.; Augustine, B. H., A Metallic Surface Corrosion Study in Aqueous NaCl Solutions Using Atomic Force Microscopy (AFM). *Chemical Educator* **2000,** *5*, 8-13.

220. Borch, T.; Camper, A. K.; Biederman, J. A.; Butterfield, P. W.; Gerlach, R.; Amonette, J. E., Evaluation of Characterization Techniques for Iron Pipe Corrosion Products and Iron Oxide Thin Films. *Journal of Environmental Engineering* **2008,** *10*, 835-844.

221. Serem, W. K.; Castro, G.; Varotta, A.; Drain, C. M.; Garno, J. C., High throughput patterning of plasmid DNA-templated nanoparticles using two particle lithography. *Materials Chemistry* **2009**, in preparation.

222. Serem, W. K.; Varotto, A.; Castro, G.; Drain, C. M.; Garno, J. C. In *Investigation of the vibrational response of individual nanoparticles using AFM with magnetic sample modulation*, National Organization for the Professional Advancement of Black Chemists and Chemical Engineers (NOBCChE), Philadelphia, PA, Royster, T., Ed. Philadelphia, PA, 2008.

223. Samson, J.; Varotto, A.; Nahirney, P. C.; Toschi, A.; Piscopo, I.; Drain, C. M., Fabrication of Metal Nanoparticles Using Toroidal Plasmid DNA as a Sacrificial Mold. *ACS Nano* **2009,** *3* (2), 339-344.

224. Caruntu, D.; Caruntu, G.; Y., C.; O'Connor, C. J.; Goloverda, G.; Kolesnichenko, V. L., Synthesis of variable-sized nanocrystals of Fe3O4 with high surface reactivity *Chemistry of Materials* **2004,** *16* (25), 5527-5534.

225. Li, J.-R.; Verberne-Sutton, S.; Lin, X.-M.; Garno, J. C., Nanostructures of Cobalt Nanoparticles Produced with “Two-Particle” Lithography. *in preparation* **2009**.

226. Daniels, S. L.; Ngunjiri, J. N.; Garno, J. C., Investigation of the magnetic properties of ferritin by combining AFM imaging with electromagnetic sample modulation (invited). *Analytical and Bioanalytical Chemistry* **2009,** *May* (in press).

227. Tesfai, A.; El-Zahab, B.; Bwambok, D. K.; Baker, G. A.; Fakayode, S. O.; Lowry, M.; Warner, I. M., Controllable formation of ionic liquid micro- and nanoparticles via a melt-emulsion-quench approach. *Nano Letters* **2008,** *8* (3), 897-901.

APPENDIX A: LETTER OF PERMISSION

American Chemical Society's Policy on Theses and Dissertations

If your university requires a signed copy of this letter see contact information below.

Thank you for your request for permission to include **your** paper(s) or portions of text from **your** paper(s) in your thesis. Permission is now automatically granted; please pay special attention to the implications paragraph below. The Copyright Subcommittee of the Joint Board/Council Committees on Publications approved the following:

> Copyright permission for published and submitted material from theses and dissertations
> ACS extends blanket permission to students to include in their theses and dissertations their own articles, or portions thereof, that have been published in ACS journals or submitted to ACS journals for publication, provided that the ACS copyright credit line is noted on the appropriate page(s).
>
> Publishing implications of electronic publication of theses and dissertation material
> Students and their mentors should be aware that posting of theses and dissertation material on the Web prior to submission of material from that thesis or dissertation to an ACS journal may affect publication in that journal. Whether Web posting is considered prior publication may be evaluated on a case-by-case basis by the journal's editor. If an ACS journal editor considers Web posting to be "prior publication", the paper will not be accepted for publication in that journal. If you intend to submit your unpublished paper to ACS for publication, check with the appropriate editor prior to posting your manuscript electronically.

If your paper has **not** yet been published by ACS, we have no objection to your including the text or portions of the text in your thesis/dissertation in **print and microfilm formats**; please note, however, that electronic distribution or Web posting of the unpublished paper as part of your thesis in electronic formats might jeopardize publication of your paper by ACS. Please print the following credit line on the first page of your article: "Reproduced (or 'Reproduced in part') with permission from [JOURNAL NAME], in press (or 'submitted for publication'). Unpublished work copyright [CURRENT YEAR] American Chemical Society." Include appropriate information.

If your paper has already been published by ACS and you want to include the text or portions of the text in your thesis/dissertation in **print or microfilm formats**, please print the ACS copyright credit line on the first page of your article: "Reproduced (or 'Reproduced in part') with permission from [FULL REFERENCE CITATION.] Copyright [YEAR] American Chemical Society." Include appropriate information.

Submission to a Dissertation Distributor: If you plan to submit your thesis to UMI or to another dissertation distributor, you should not include the unpublished ACS paper in your thesis if the thesis will be disseminated electronically, until ACS has published your paper. After publication of the paper by ACS, you may release the entire thesis (**not the individual ACS article by itself**) for electronic dissemination through the distributor; ACS's copyright credit line should be printed on the first page of the ACS paper.

Use on an Intranet: The inclusion of your ACS unpublished or published manuscript is permitted in your thesis in print and microfilm formats. If ACS has published your paper you may include the manuscript in your thesis on an intranet that is not publicly available. Your ACS article cannot be posted electronically on a publicly available medium (i.e. one that is not password protected), such as but not limited to, electronic archives, Internet, library server, etc. The only material from your paper that can be posted on a public electronic medium is the article abstract, figures, and tables, and you may link to the article's DOI or post the article's author-directed URL link provided by ACS. This paragraph does not pertain to the dissertation distributor paragraph above.

Questions? Call +1 202/872-4368/4367. Send e-mail to copyright@acs.org or fax to +1 202-776-8112. 10/10/03, 01/15/04, 06/07/06

APPENDIX B: PROCEDURE FOR CLEANING COPPER SURFACES

To prepare the copper substrates for the immersion experiments, the following protocol was followed to clean the surfaces of the copper:

1. Sonicate the copper sample in 0.5% Triton X-100 surfactant for 5 minutes.

2. Rinse the sample with Milli-Q water.

3. Sonicate the sample in Milli-Q water for 5 minutes.

4. Rinse the sample with acetone.

5. Dry the sample in air.

6. Store the sample in a dessicator until use.

APPENDIX C: TOF-SIMS SPECTRA OF COPPER SURFACES IMMERSED IN WATERS OF VARYING CHEMISTRIES

Time-of-flight secondary ion mass spectrometry (ToF-SIMS) is capable of shallow sputter depth profiling. An ion (Ar^+) gun is operated in the DC mode during the sputtering phase in order to remove material, and the primary ion gun is operated in the pulsed mode for the ion acquisition. Depth profiling by ToF-SIMS allows monitoring of all species of interest simultaneously, and with high mass resolution. For the depth profiles, an Ar gun of 3 keV was used for the sputtering of sample surface and the sputter area was 300 × 300 μm^2. The sputtered surface was analyzed by the Ga^+ gun with 25 keV having 1.85 to 1.95 pA current and the analyzed area was 100 × 100 μm^2.

A CAMECA ION-TOF model IV instrument equipped with a 25 kV liquid metal (^{69}Ga) ion gun was used for ToF-SIMS analysis. A flood gun was used for charge neutralization. Corroded copper coupon samples were cut as small as 1 × 1 cm^2, then analyzed for the chemical composition on surface and depth profiling from the top down. The mass spectra generated are used to determine the composition of sample surface constituents.

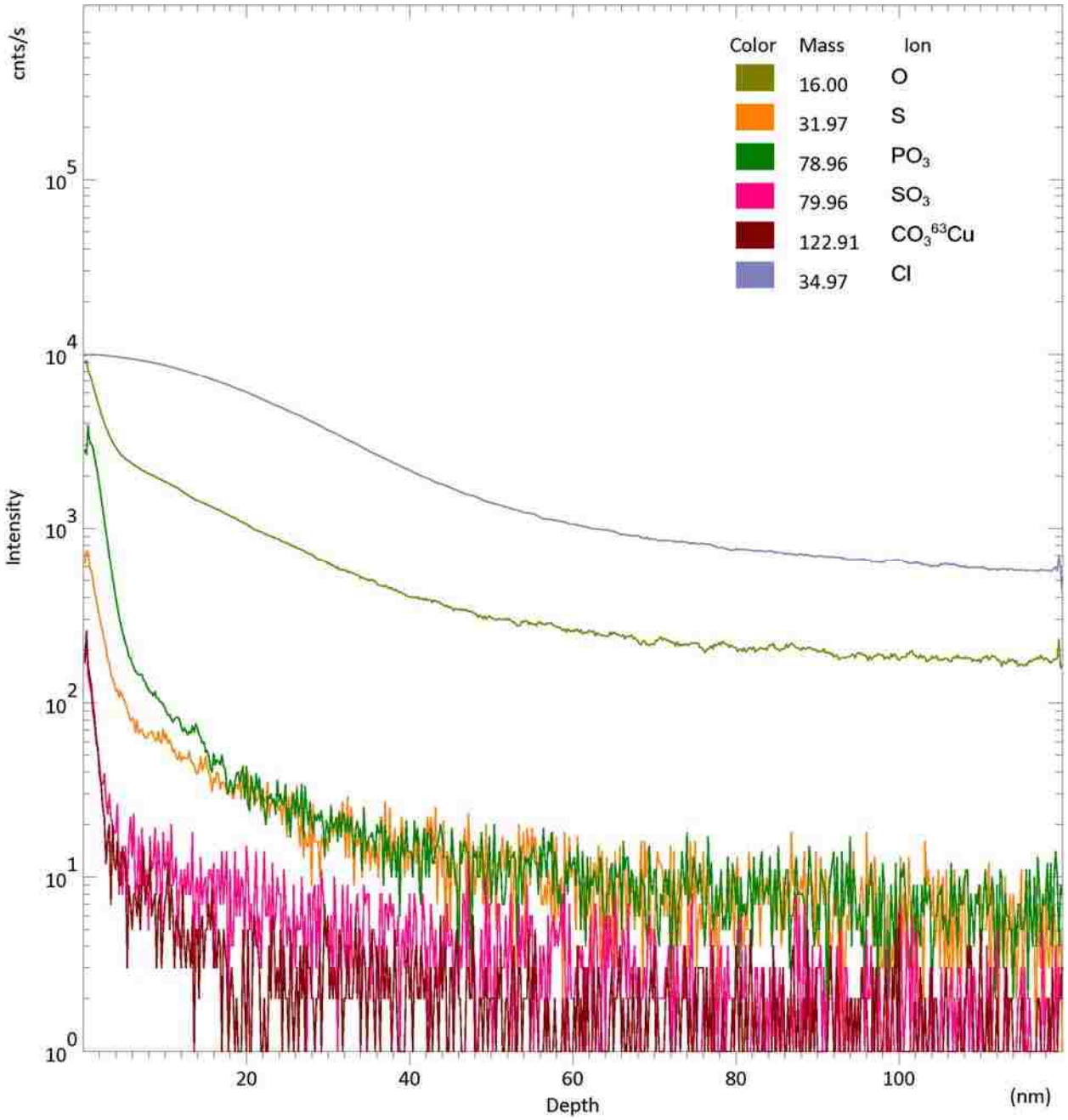

Figure C.1. Negative ion ToF-SIMS spectrum of a copper surface immersed in water sample 1 from table 4.1 for 6 h.

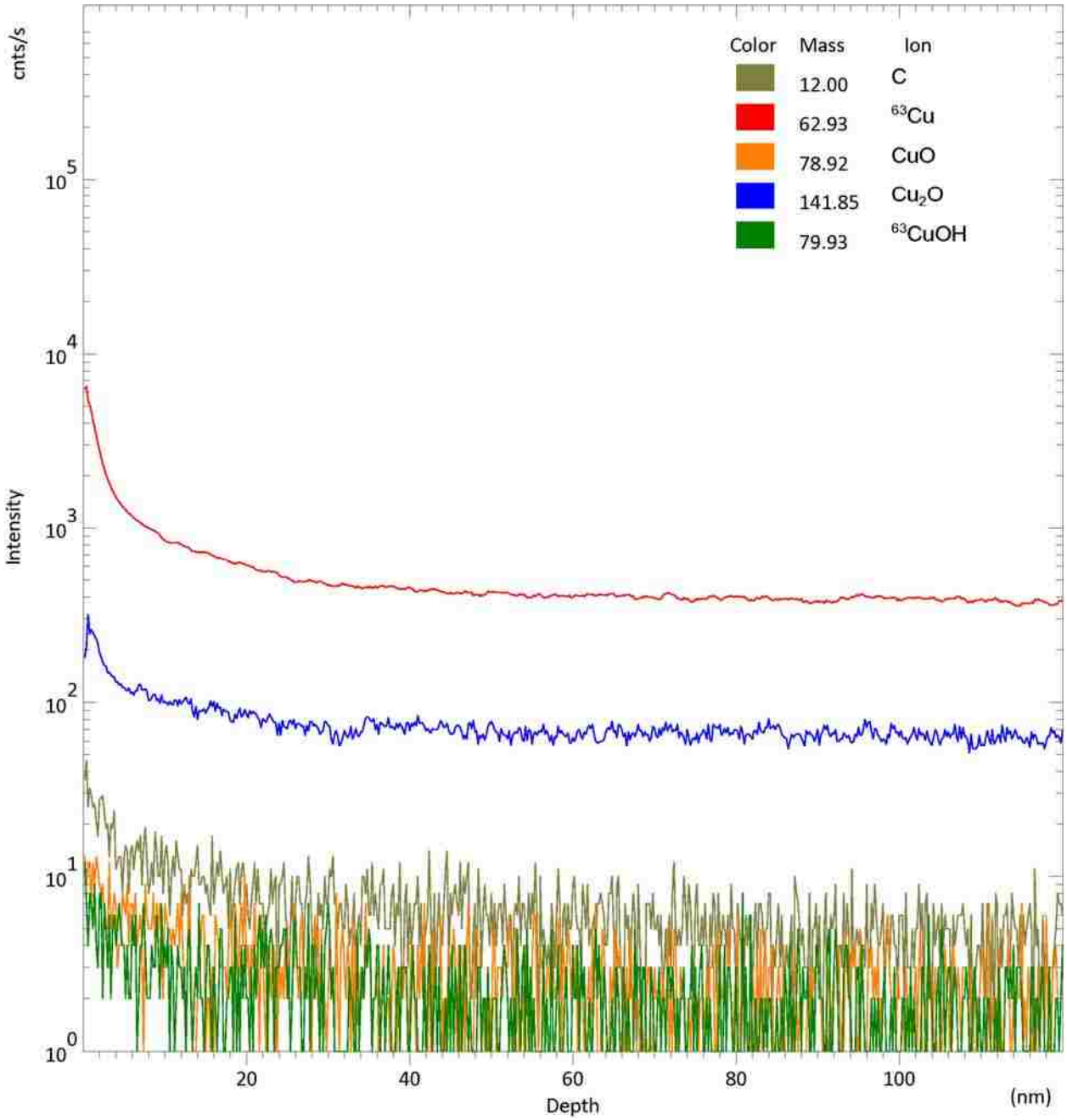

Figure C.2. Positive ion ToF-SIMS spectrum of a copper surface immersed in water sample 1 from table 4.1 for 6 h.

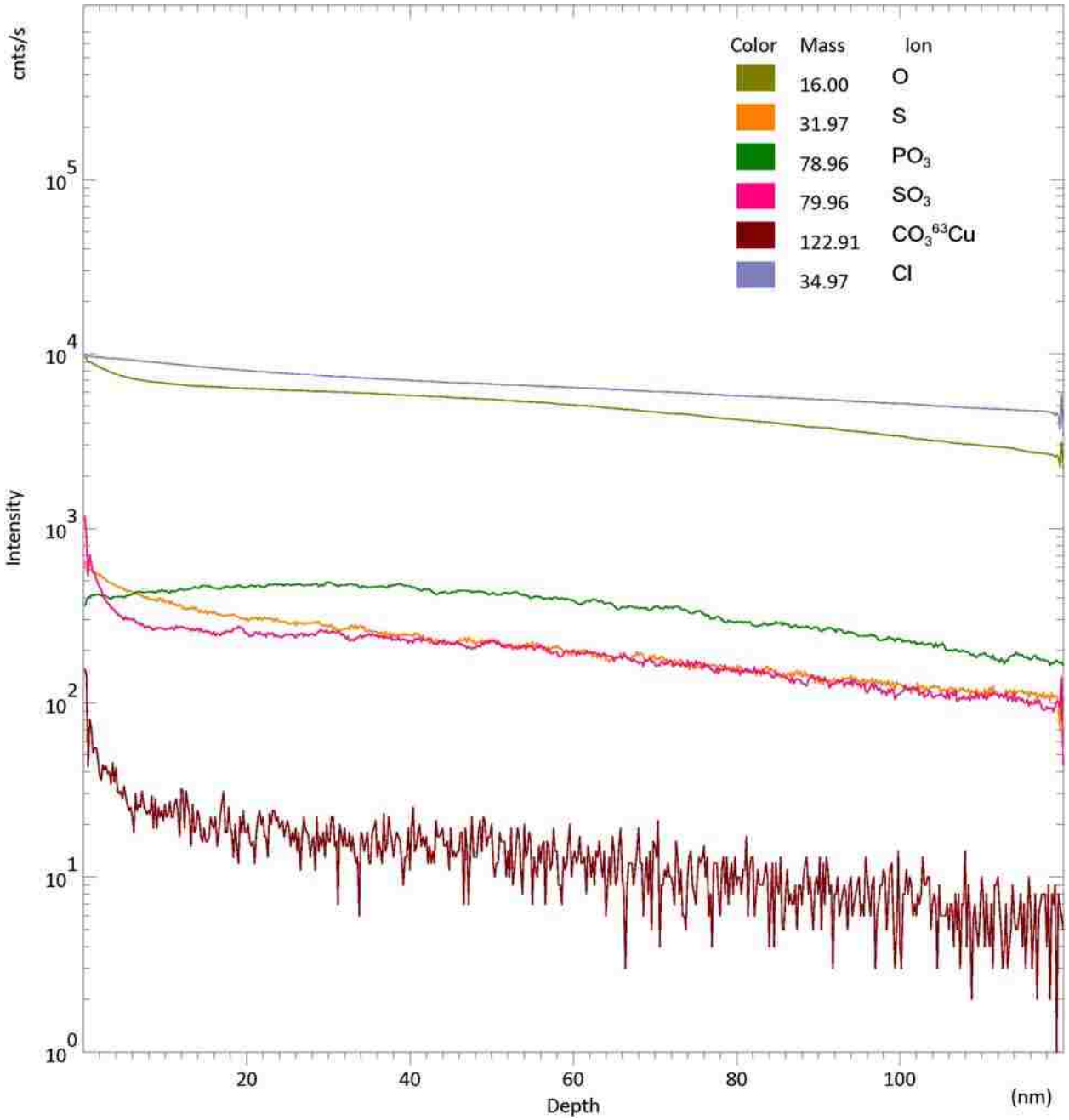

Figure C.3. Negative ion ToF-SIMS spectrum of a copper surface immersed in water sample 1 from table 4.1 for 24 h.

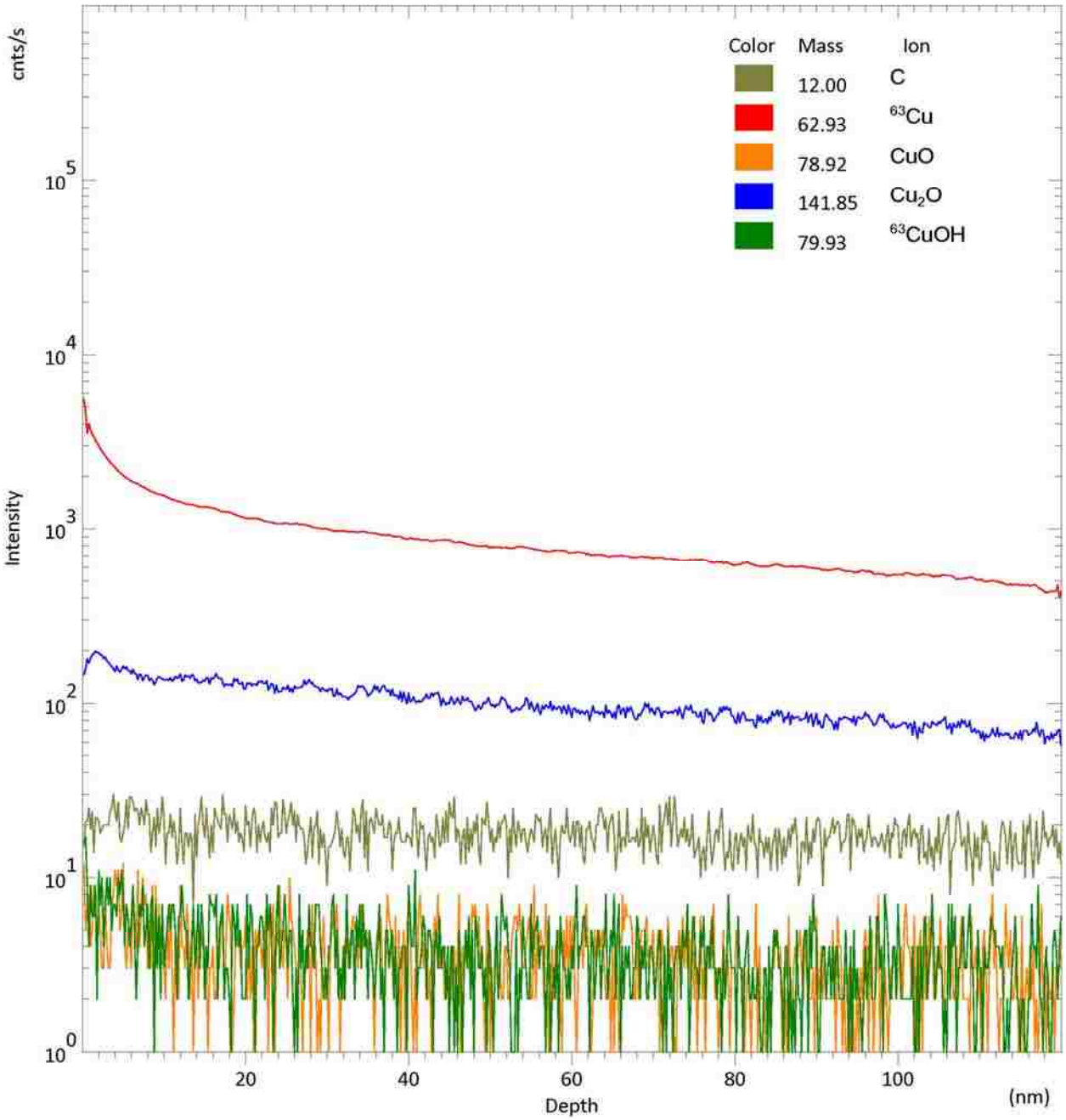

Figure C.4. Positive ion ToF-SIMS spectrum of a copper surface immersed in water sample 1 from table 4.1 for 24 h.

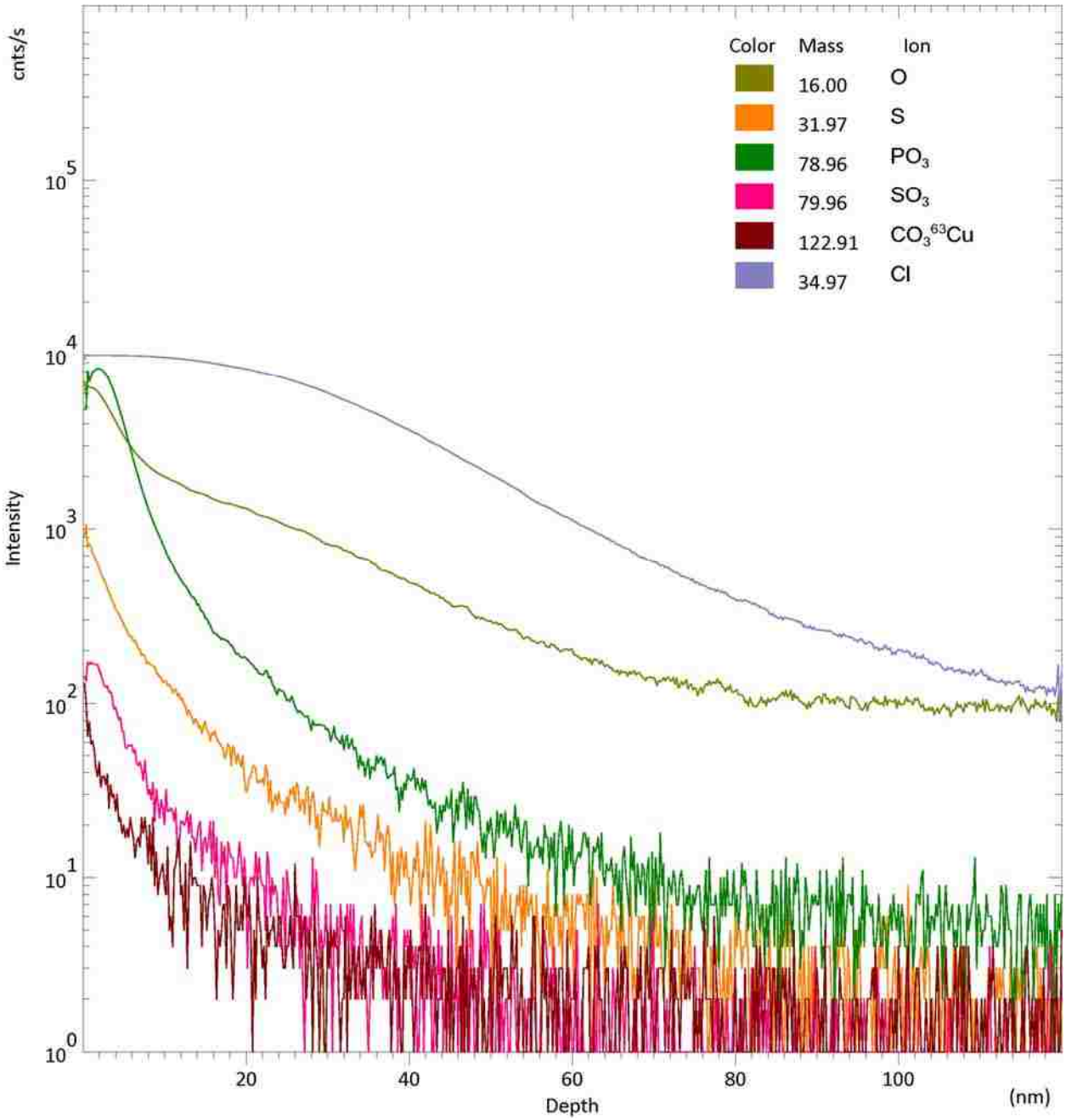

Figure C.5. Negative ion ToF-SIMS spectrum of a copper surface immersed in water sample 2 from table 4.1 for 6 h.

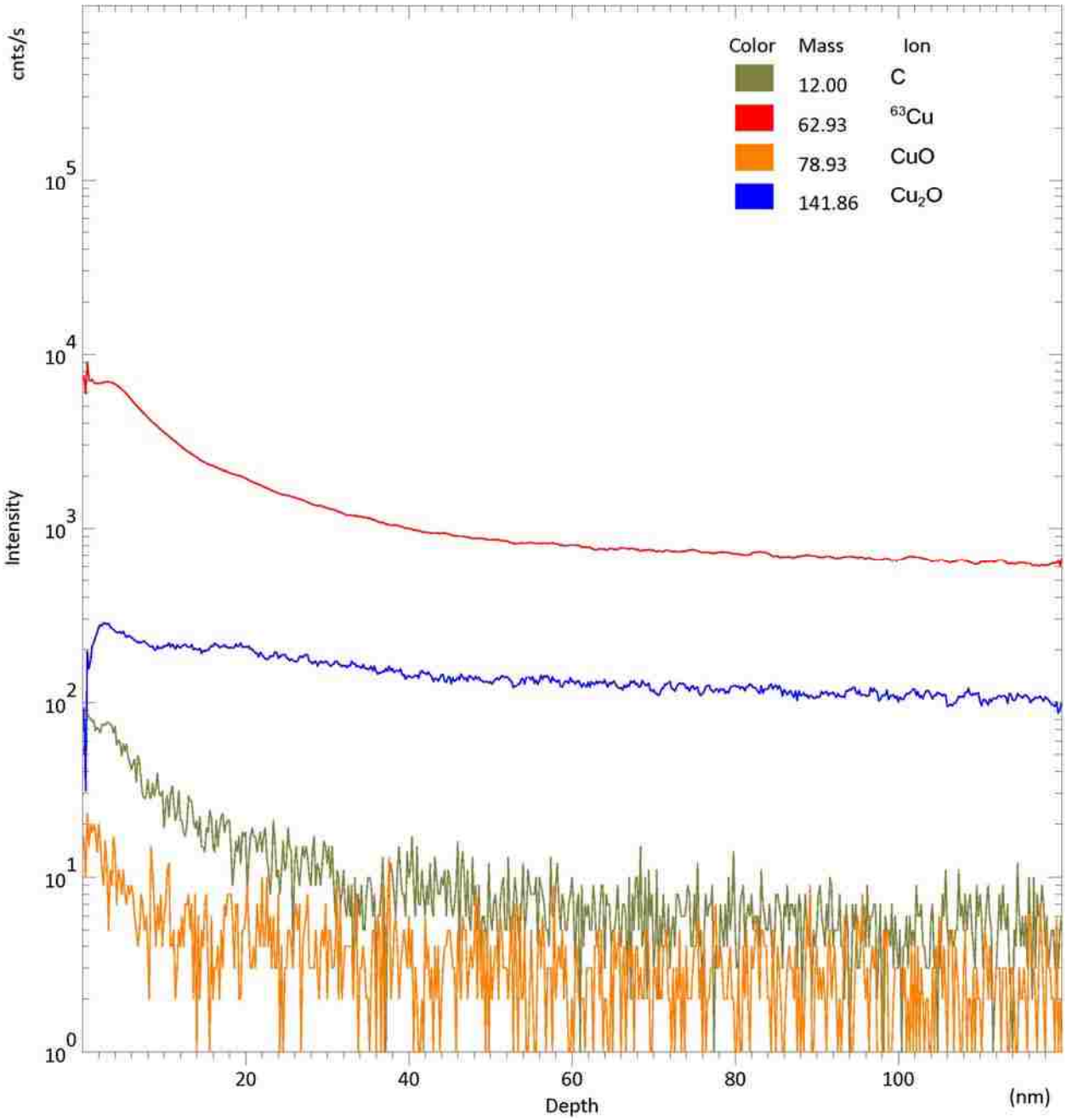

Figure C.6. Positive ion ToF-SIMS spectrum of a copper surface immersed in water sample 2 from table 4.1 for 6 h.

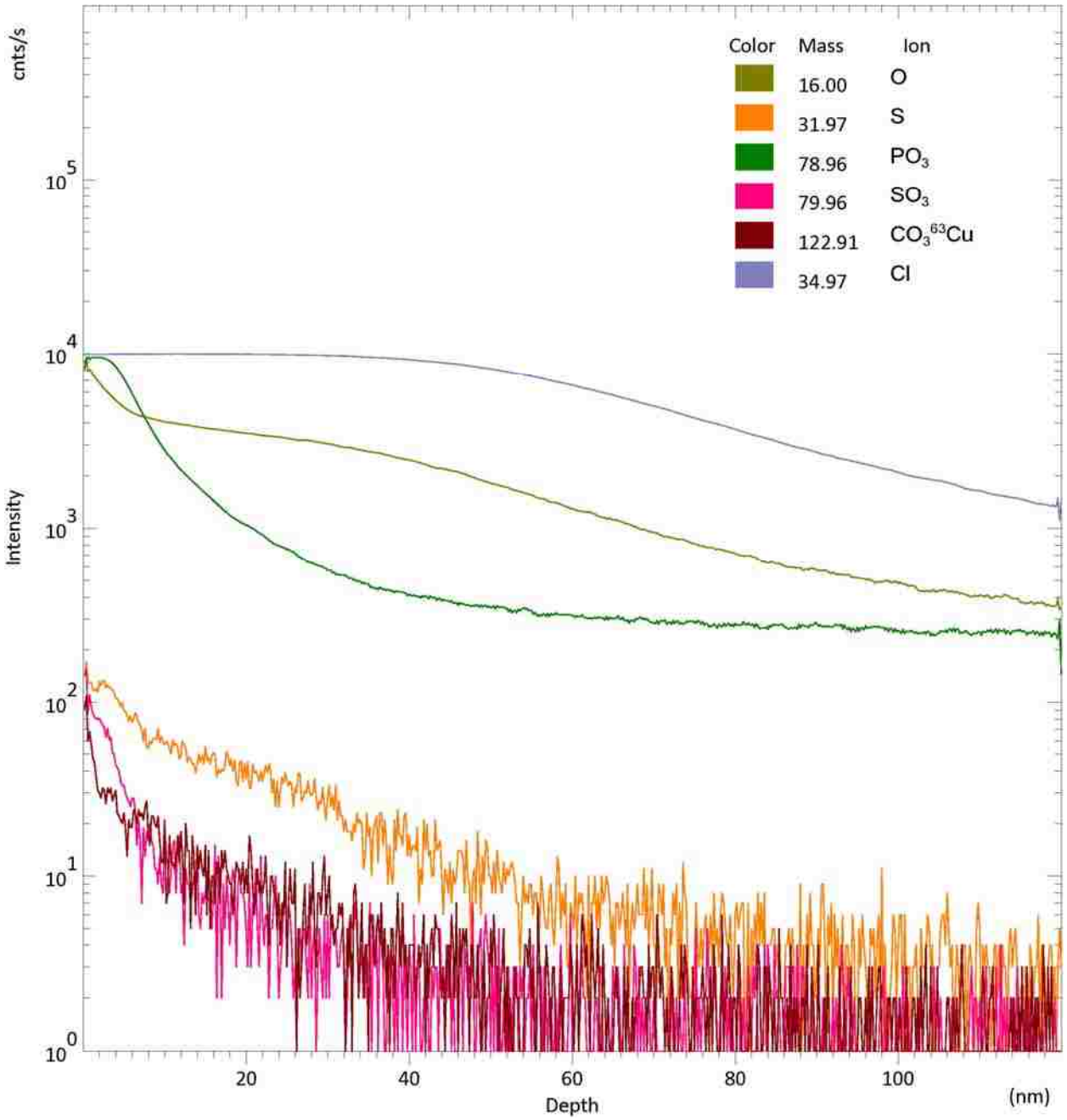

Figure C.7. Negative ion ToF-SIMS spectrum of a copper surface immersed in water sample 2 from table 4.1 for 24 h.

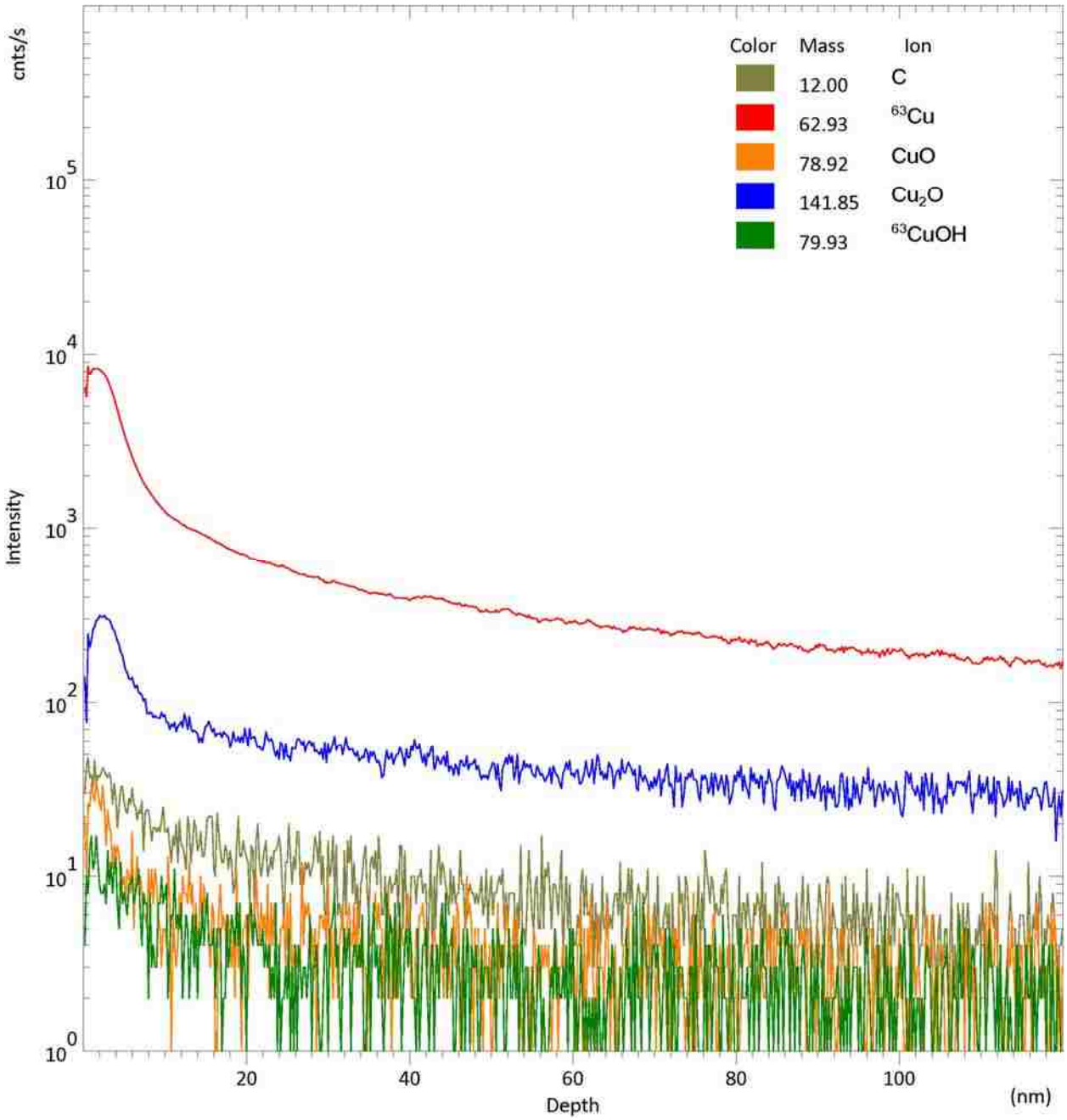

Figure C.8. Positive ion ToF-SIMS spectrum of a copper surface immersed in water sample 2 from table 4.1 for 24 h.

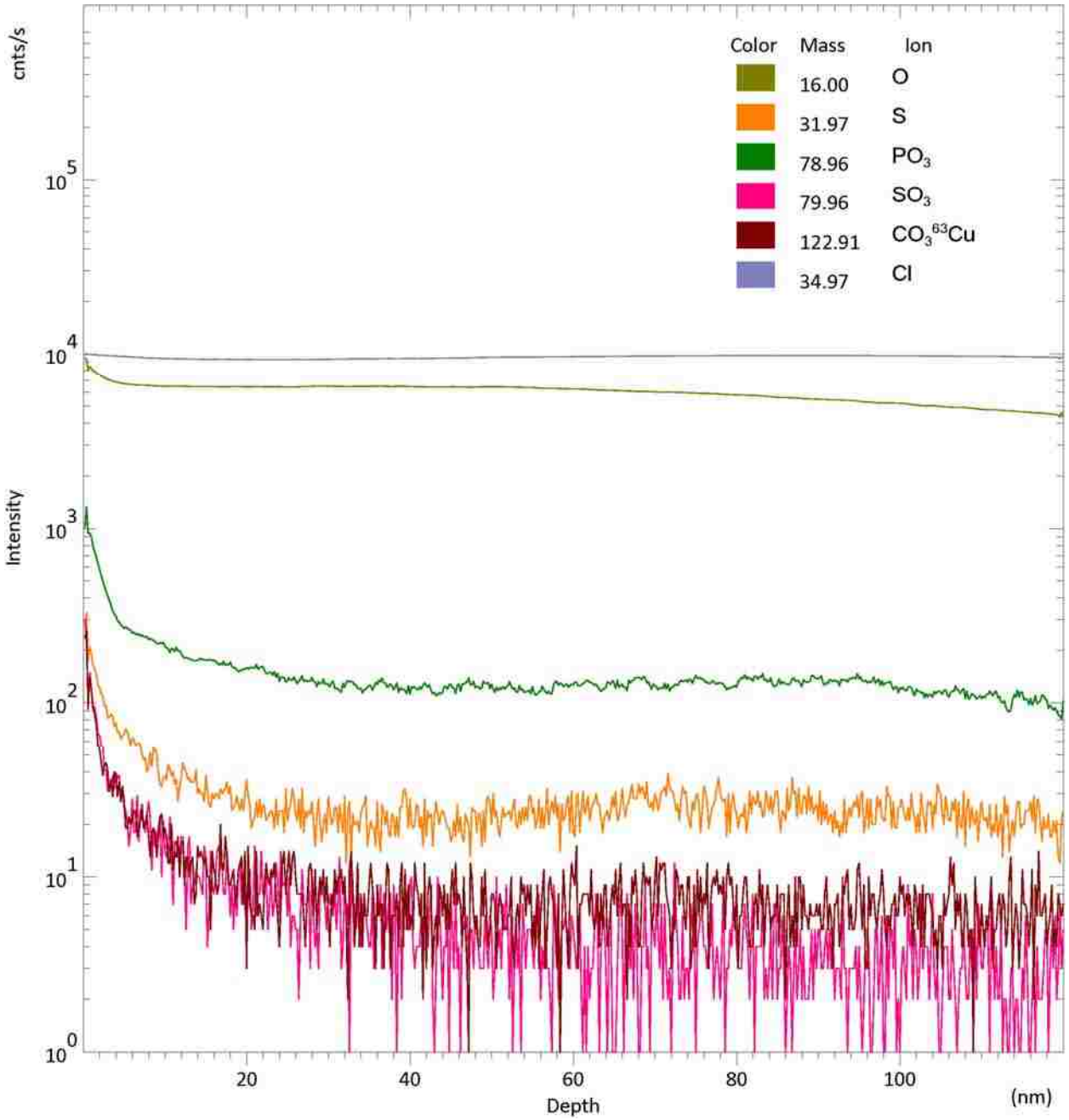

Figure C.9. Negative ion ToF-SIMS spectrum of a copper surface immersed in water sample 3 from table 4.1 for 6 h.

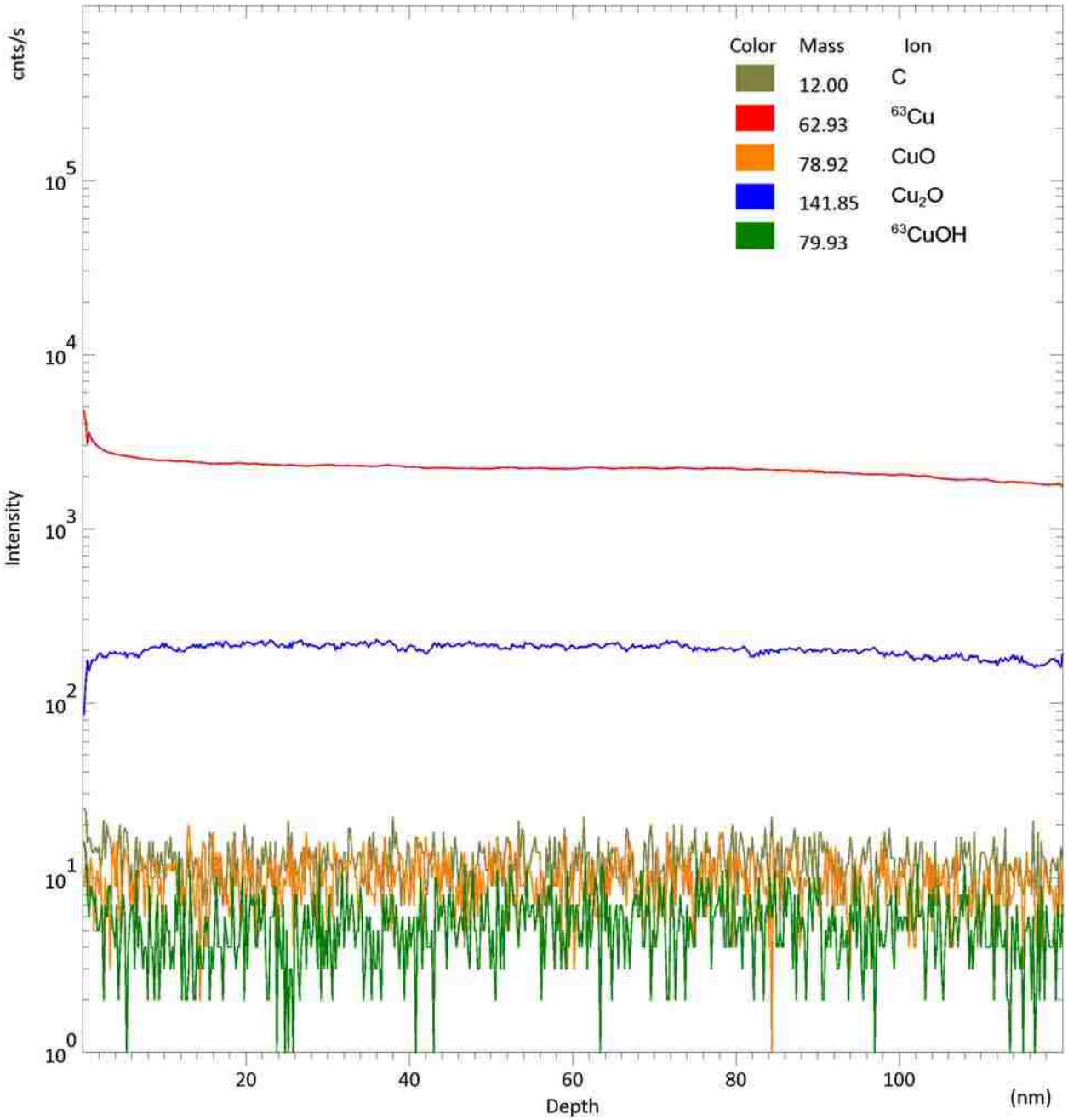

Figure C.10. Positive ion ToF-SIMS spectrum of a copper surface immersed in water sample 3 from table 4.1 for 6 h.

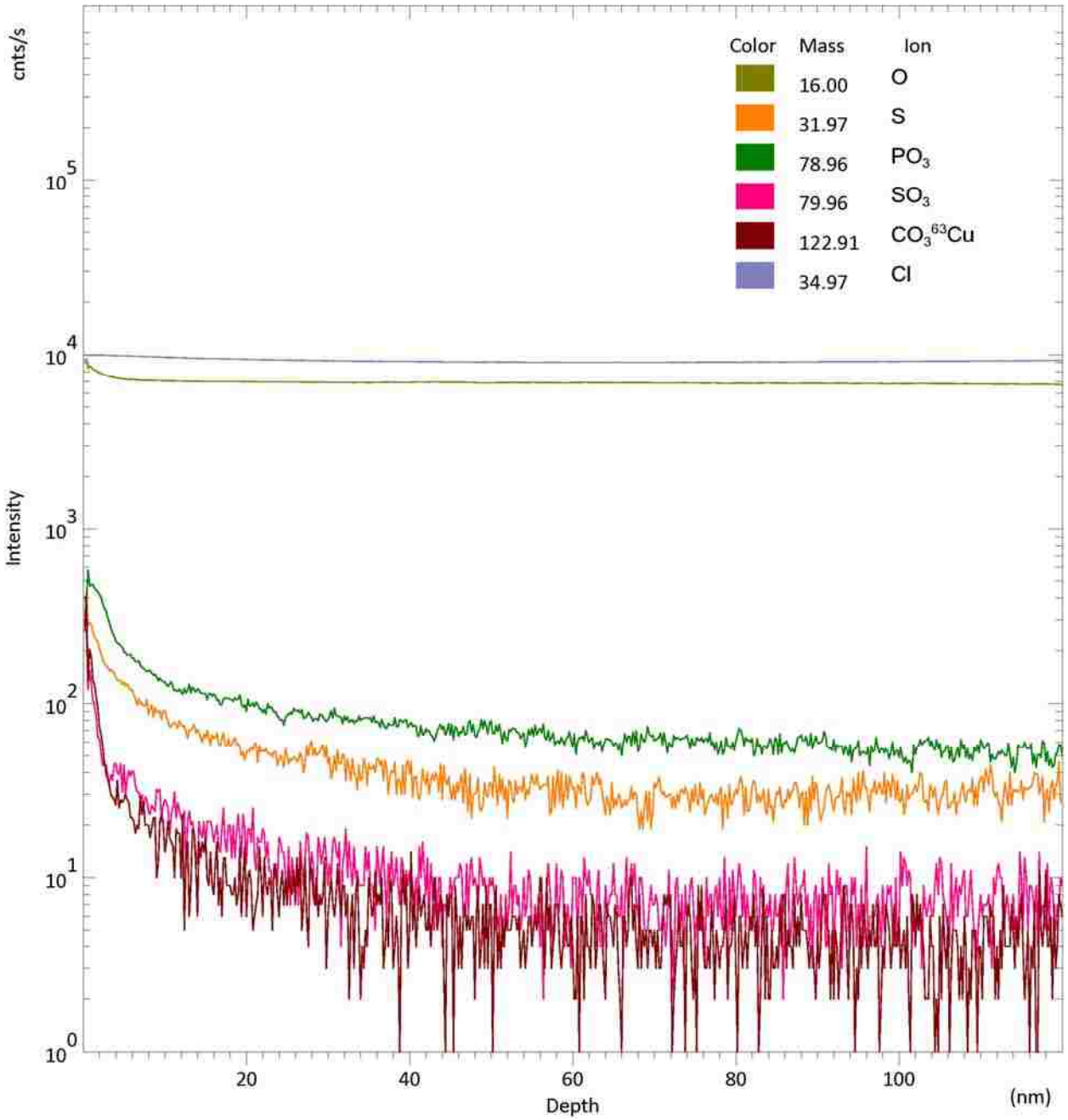

Figure C.11. Negative ion ToF-SIMS spectrum of a copper surface immersed in water sample 3 from table 4.1 for 24 h.

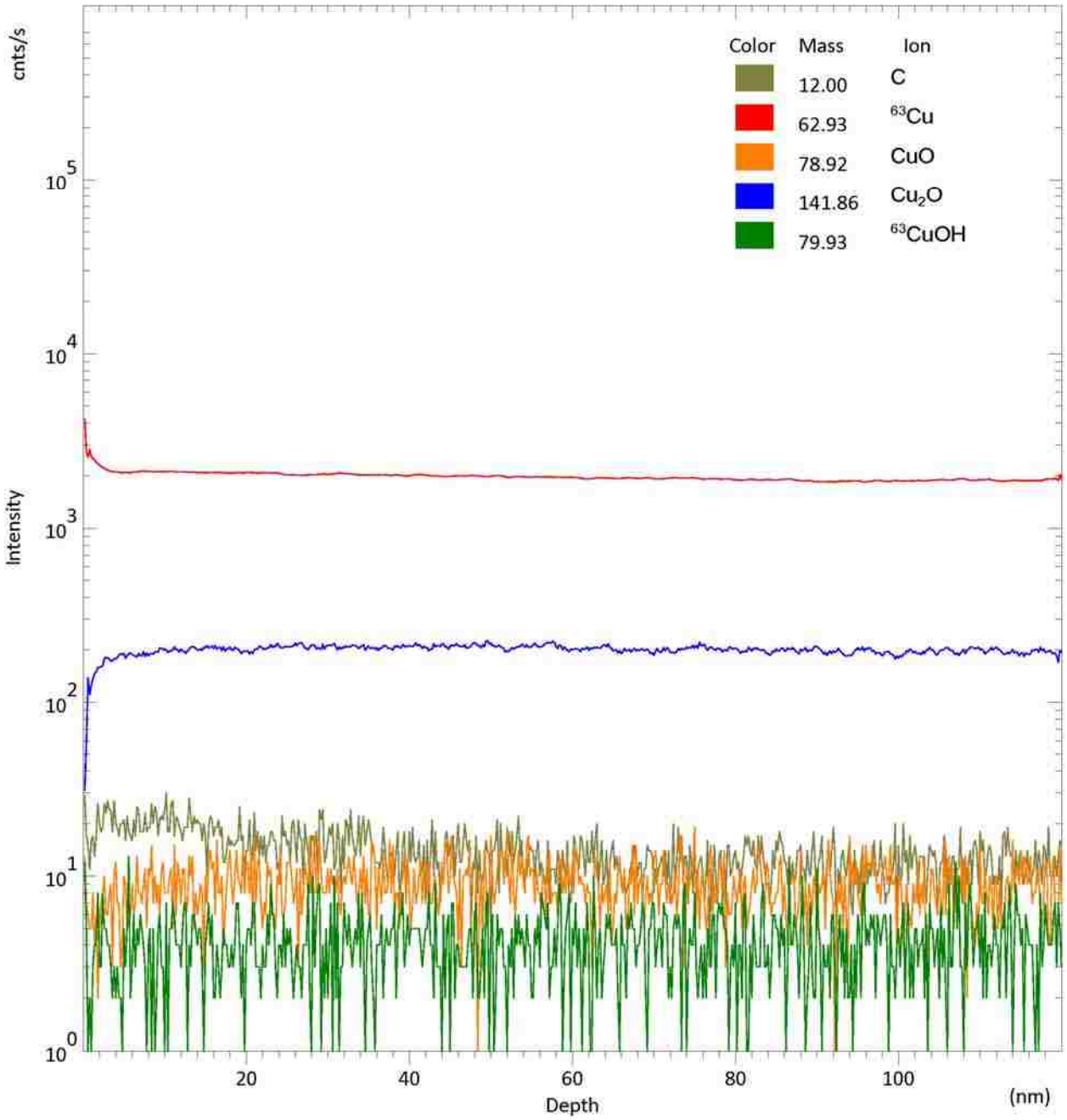

Figure C.12. Positive ion ToF-SIMS spectrum of a copper surface immersed in water sample 3 from table 4.1 for 24 h.

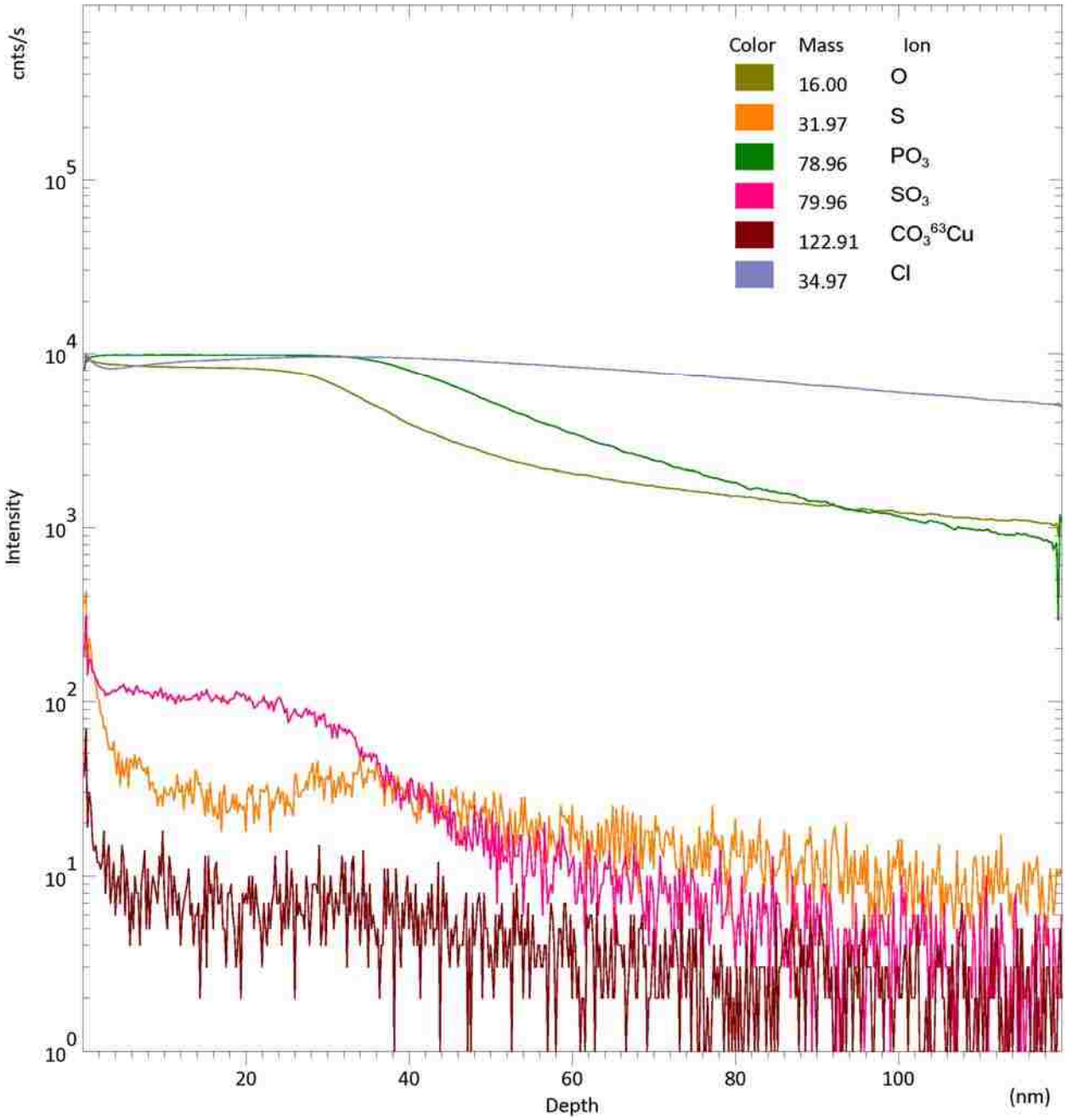

Figure C.13. Negative ion ToF-SIMS spectrum of a copper surface immersed in water sample 4 from table 4.1 for 6 h.

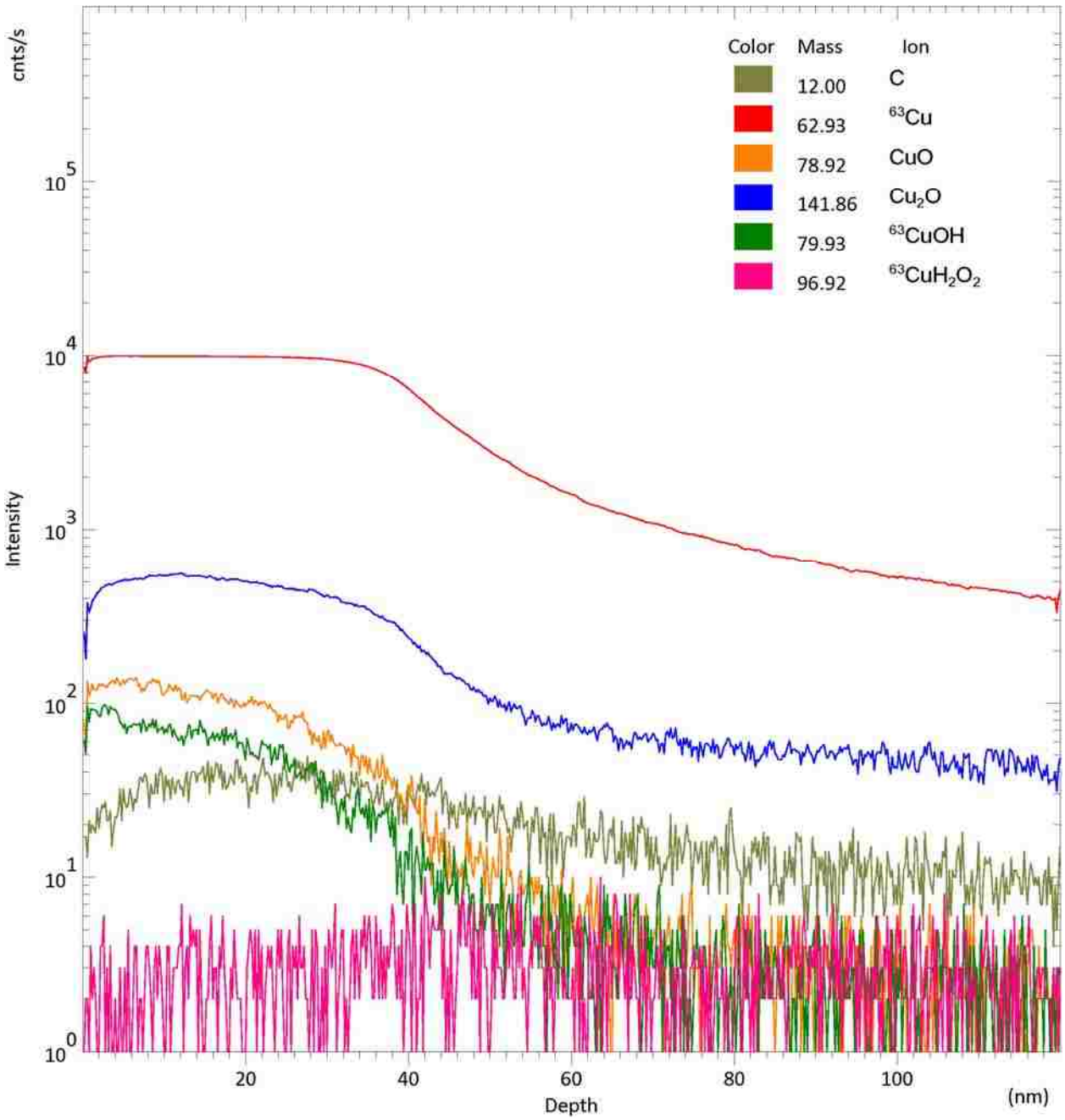

Figure C.14. Positive ion ToF-SIMS spectrum of a copper surface immersed in water sample 4 from table 4.1 for 6 h.

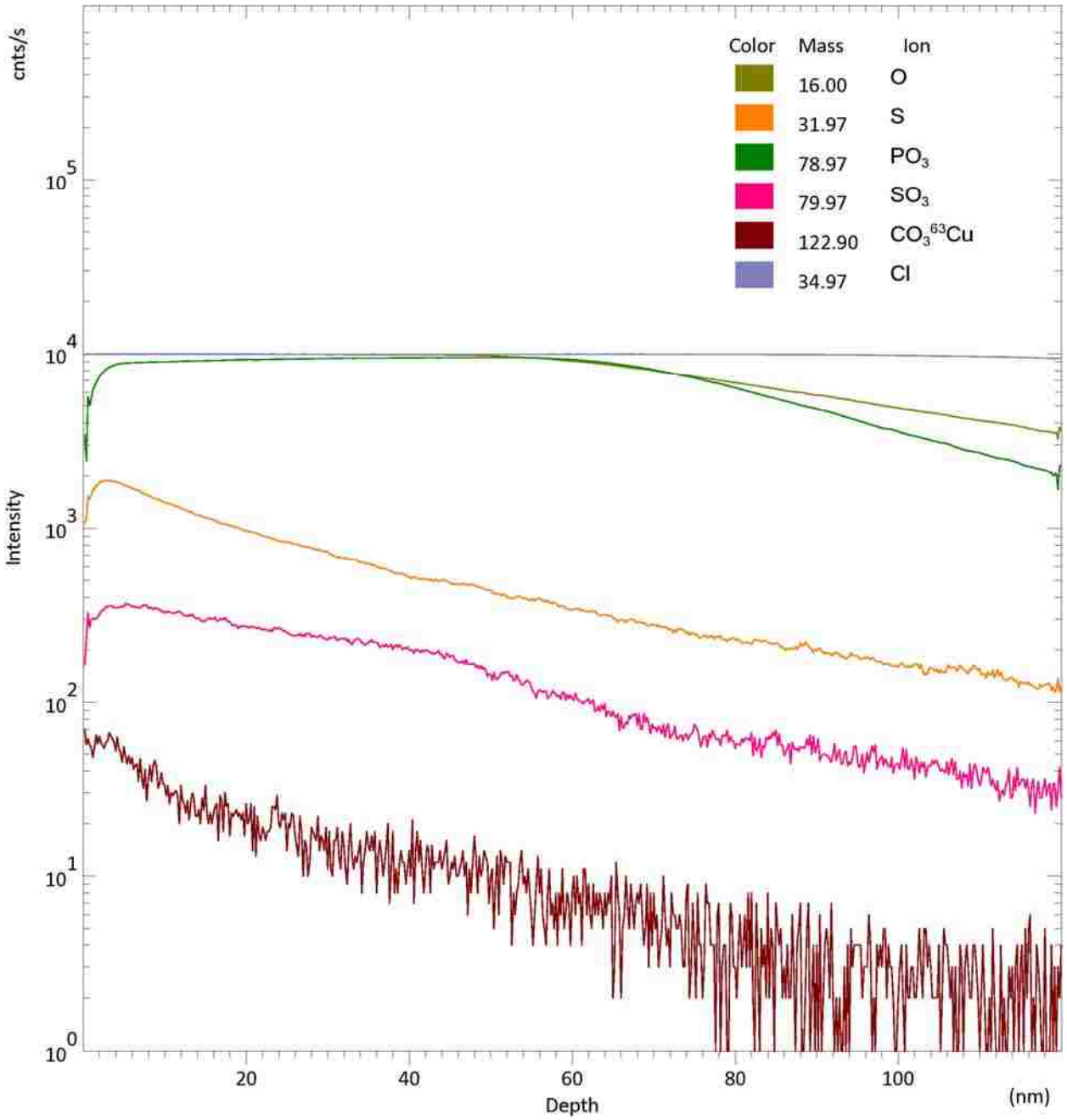

Figure C.15 . Negative ion ToF-SIMS spectrum of a copper surface immersed in water sample 4 from table 4.1 for 24 h.

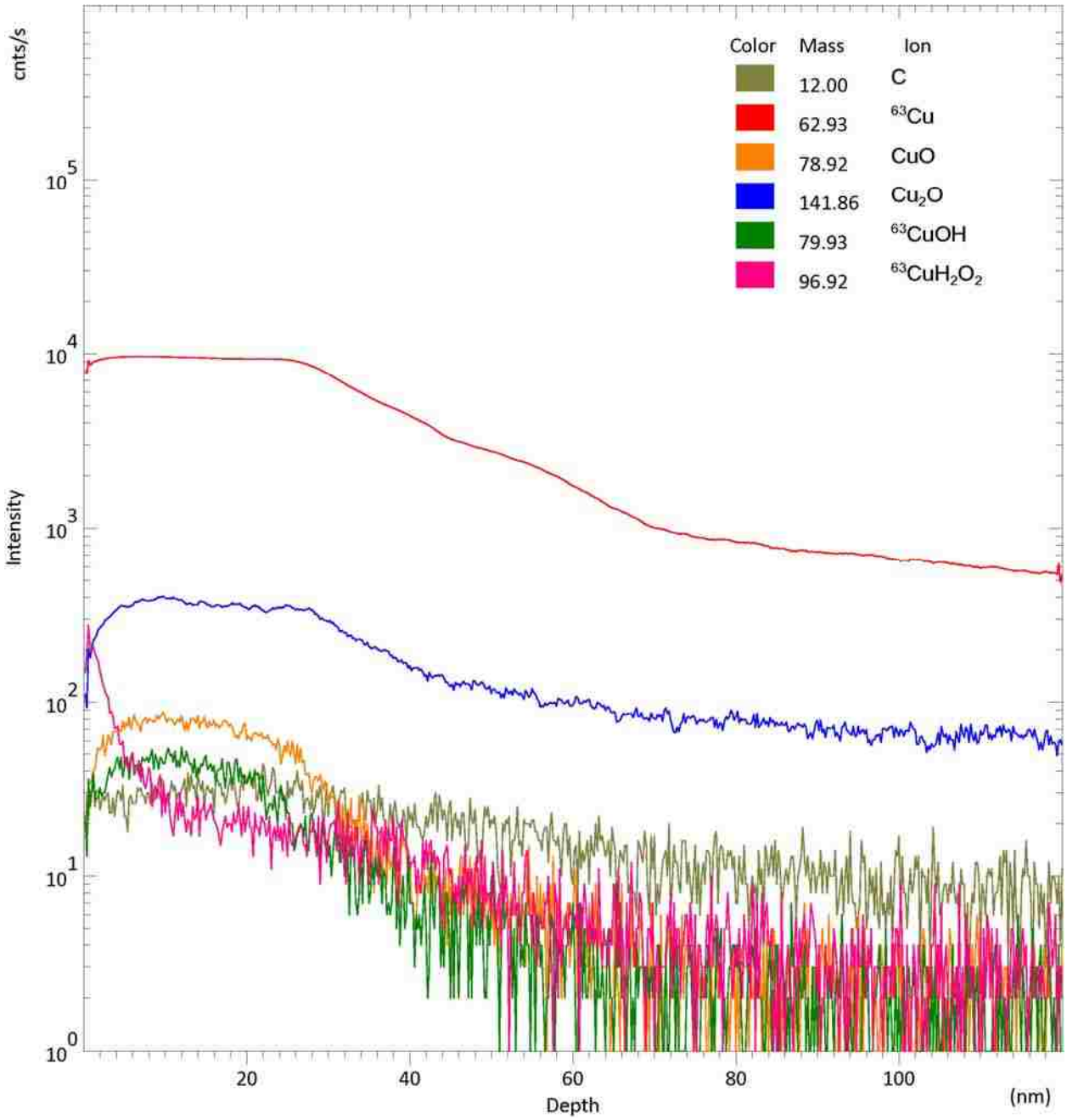

Figure C.16. Positive ion ToF-SIMS spectrum of a copper surface immersed in water sample 4 from table 4.1 for 24 h.

VITA

Brian Lewandowski was born in Baton Rouge, Louisiana in 1982 to Richard and Barbara Lewandowski. He attended Central High School where he gained an interest in the subject of chemistry. He received his Bachelor of Science degree in chemistry from Loyola University New Orleans in May 2004. In the fall of 2004, he enrolled in the doctoral program in the Department of Chemistry at Louisiana State University where he joined the research group of Dr. Jayne C. Garno. During 2007, Brian Lewandowski performed an internship with the Environmental Protection Agency in Cincinnati, Ohio under the guidance of Dr. Darren A. Lytle. The degree of Doctor of Philosophy will be conferred at the Spring 2009 Commencement.